

FINITE ELEMENT MODELLING OF A COMPOSITE
WIND TURBINE BLADE WITH FULLY-BONDED AND
PARTICALLY UNBONDED TRAILING EDGE

A THESIS SUBMITTED TO
THE GRADUATE SCHOOL OF NATURAL AND APPLIED SCIENCES
OF
MIDDLE EAST TECHNICAL UNIVERSITY

BY
MELTEM OZYILDIZ

IN PARTIAL FULFILLMENT OF THE REQUIREMENTS
FOR
THE DEGREE OF MASTER OF SCIENCE
IN
AEROSPACE ENGINEERING

JUNE 2018

Approval of the thesis:

**FINITE ELEMENT MODELLING OF A COMPOSITE WIND TURBINE
BLADE WITH FULLY-BONDED AND PARTIALLY UNBONDED
TRAILING EDGE**

submitted by **MELTEM ÖZYILDIZ** in partial fulfillment of the requirements for the degree of **Master of Science in Aerospace Engineering Department, Middle East Technical University** by,

Prof. Dr. Halil Kalıpçılar
Dean, Graduate School of **Natural and Applied Sciences** _____

Prof. Dr. Ozan Tekinalp
Head of Department, **Aerospace Engineering** _____

Assoc. Prof. Dr. Demirkan Çöker
Supervisor, **Aerospace Engineering Dept., METU** _____

Examining Committee Members:

Prof. Dr. Altan Kayran
Aerospace Engineering Dept., METU _____

Assoc. Prof. Dr. Demirkan ÇÖKER
Aerospace Engineering Dept., METU _____

Prof. Dr. Kemal Levend Parnas
Mechanical Engineering Dept., TED University _____

Assoc. Prof. Dr. Mehmet Ali Güler
Mechanical Engineering Dept., TOBB _____

Assoc. Prof. Dr. Ercan GÜRSES
Aerospace Engineering Dept., METU _____

Date: 08.06.2018

I hereby declare that all information in this document has been obtained and presented in accordance with academic rules and ethical conduct. I also declare that, as required by these rules and conduct, I have fully cited and referenced all material and results that are not original to this work.

Name, Last name: Meltem ÖZYILDIZ

Signature:

ABSTRACT

FINITE ELEMENT MODELLING OF A COMPOSITE WIND TURBINE BLADE WITH FULLY-BONDED AND PARTIALLY UNBONDED TRAILING EDGE

Özyıldız, Meltem

M.S., Department of Aerospace Engineering

Supervisor: Assoc. Prof. Demirkan Çöker.

June 2018, 101 pages

In this thesis, strength analysis of an existing 5-meter glass-fiber epoxy composite wind turbine blade subjected to monotonic loading condition is presented. Finite element analysis is employed to simulate the virtual testing of the blade and understand the failure modes/mechanisms which may lead to the ultimate failure of the blade. CAD Model of the blade is prepared using NX 10.0 and ANSYS ACP/Pre module is utilized for building the material model of the blade. The evaluation of the stresses is carried out with two different approaches: linear elastic analysis using Tsai-Wu criteria and linear elastic analysis using Puck criteria. Linear analysis is carried out with ANSYS ACP/Post module. Analysis of the blade is also performed with the blade that has debonding in the trailing edge between the suction and pressure sides because the most critical damage occurs as debonding between suction and pressure sides of the blade. After the analysis of the blade, ANSYS ACP/Post module is used for the visualization of the results. Critical components and regions with the highest risk of failure are identified and the effect of debond region is assessed. The simulation results will be utilized to calibrate a 5-m blade test set-up and predict and compare with failure modes from blade testing.

KEYWORDS: Composite wind turbine blades, debonding, finite element analysis, progressive failure analysis, Puck failure criteria, Tsai-Wu failure criterion.

ÖZ

TAMAMEN YAPIŞIK VE KISMEN YAPIŞIK OLMAYAN KENARLI BİR KOMPOZİT RÜZGAR TÜRBİN KANADININ SONLU ELEMANLAR MODELLEMESİ

Özyıldız, Meltem

Yüksek Lisans, Havacılık ve Uzay Mühendisliği

Tez Yöneticisi: Doç. Dr. Demirkan Çöker

Haziran 2018, 101 sayfa

Bu tez kapsamında, RÜZGEM için üretilen 5 metre uzunluğundaki bir cam elyaf polimer kompozit rüzgâr türbin kanadının statik yük altında dayanımı incelenmiştir. Kompozit rüzgâr türbin kanadını simüle etmek ve dayanıksızlığa yol açabilecek hata modlarını/mekanizmalarını anlamak için sonlu elemanlar analizi kullanılmıştır. Kanat NX 10.0 kullanılarak üç boyutlu olarak modellenmiş ve ANSYS ACP / Pre modülü kullanılarak da kanadın malzeme modeli oluşturulmuştur. Hata modlarını /mekanizmalarını anlamak için iki farklı yaklaşım kullanılmıştır: Tsai-Wu kriteri kullanılarak lineer analiz ve Puck kriteri kullanılarak lineer analiz. Lineer analizler için ANSYS ACP / Post modülü kullanılmıştır. Ayrıca, yapılan literatür araştırmasına göre, rüzgâr türbin kanatlarında en fazla hata, emme ve basma kısımlarının birleşim yerinde kullanılan yapıştırıcıdan kaynaklı olduğu görülmüştür. Buna göre, yapılan analizler mevcut kanadın emme ve basma kısımlarının birleşim yerinde bir ayrılma yaratılarak tekrarlanmıştır. Analizlerin tamamlanmasının ardından sonuçlar karşılaştırılmıştır. Buna göre, kritik bileşenler ve en yüksek hata riskine sahip bölgeler belirlenmiştir. Yapıştırıcının sağlam olduğu ve olmadığı analiz sonuçları karşılaştırılarak, yapıştırıcının önemi görülmüştür. Ek olarak, farklı yaklaşım sonuçlarına göre en optimum kompozit rüzgâr türbin kanadı dayanım analiz metoduna karar verilmiştir.

Bu tezden elden edilen veriler, mevcut kanadın statik test sonuçlarına katkı sağlayacaktır.

ANAHTAR KELİMELER: Aşamalı hata analizi, kompozit rüzgâr türbin kanadı, Puck hata kriter, Tsai-Wu hata kriteri, sonlu elemanlar analizi.

To my family...

ACKNOWLEDGEMENTS

First and foremost, I would like to thank my thesis advisor Assoc. Prof. Demirkan Çöker. His office door was always open whenever I ran into a trouble or had a question about my study. He consistently allowed this study to be my own work but steered me in the right the direction whenever he thought I needed it.

Besides my advisor, I would like to thank the rest of my thesis committee, Prof. Dr. Levend Parnas, Prof. Dr. Altan Kayran, Prof. Dr. Mehmet Ali Güler and Assoc. Prof. Dr. Ercan Gürses for valuable comments on this thesis.

I am thankful to my company ASELSAN Inc. for letting and supporting of my thesis. Also, the cooperation and friendly support of my colleagues in ASELSAN during my thesis study also deserves to be acknowledged.

I really appreciate the support of my friends, who always support me. I managed to overcome the difficulties in the process with their love and understanding.

Last but not the least, I must express my very profound gratitude to my parents, Takip Özyıldız and Şermin Özyıldız and to my brother, Ethem Özyıldız for providing me with support and continuous encouragement throughout my years of study and through the process of researching and writing this thesis. This accomplishment would not have been possible without them. Thank you.

TABLE OF CONTENTS

ABSTRACT	3
ÖZ	5
ACKNOWLEDGEMENTS	8
TABLE OF CONTENTS	9
LIST OF TABLES	12
LIST OF FIGURES	13
LIST OF SYMBOLS	21
ABBREVIATIONS	22
1. INTRODUCTION	1
1.1. Wind Turbine Blades.....	1
1.1.1. Wind Turbine Blade Construction.....	1
1.1.2. Loads on Wind Turbine Blade.....	3
1.1.3. Materials Used in Wind Turbine Blades.....	4
1.2. Wind Turbine Blade in METU RUZGEM.....	5
1.3. Problem Definition in Wind Turbine Blades	6
1.4. Scope of The Study	7
2. LITERATURE SURVEY	9

2.1. Damage on Wind Turbine Blades	9
3. FINITE ELEMENT MODEL OF WIND TURBINE BLADE.....	15
3.1. Geometric Modeling of The Blade	15
3.2. Contact Definitions.....	18
3.3. Mesh Convergence	19
3.4. Material Layout of The Blade	21
3.4. Loading Conditions	26
4. STATIC AND FAILURE ANALYSIS OF THE FULLY-BONDED BLADE .	29
4.4. Modal Analysis.....	29
4.5. Static Analysis	31
4.5.1. Flapwise Analysis	31
4.5.2. Flapwise and Edgewise Analysis.....	32
4.6. Failure Analysis.....	34
4.6.1. Methodology	34
4.6.2. Failure Analysis Under Flapwise Loading	36
4.6.3. Failure Analysis Under Flapwise And Edgewise Loading	45
5. STATIC AND FAILURE ANALYSIS OF THE UNBONDED BLADE.....	55
5.1. Unbonded Blade Model.....	55

5.2. Modal Analysis.....	57
5.3. Static Analysis.....	59
5.3.1. Flapwise Analysis.....	59
5.3.2. Flapwise and Edgewise Analysis.....	60
5.4. Failure Analysis.....	61
5.4.1. Failure Analysis Under Flapwise Loading.....	62
5.4.2. Failure Analysis Under Flapwise And Edgewise Loading.....	70
6. DISCUSSION.....	79
6.1. Comparison of Stress Under Different Loading Conditions.....	79
6.2. Comparison of Tsai-Wu and Puck Failure Criteria.....	83
6.3. Comparison of Fully-bonded and Unbonded Blade Model.....	88
7. SUMMARY AND CONCLUSIONS.....	99
7.1. Summary.....	99
7.2. Conclusions.....	100
7.3. Future Works.....	101
REFERENCES.....	103

LIST OF TABLES

Table 1. Material properties.	21
Table 2. Flapwise and edgewise loads over blade radial position.	26
Table 3. Results of modal analysis.	30
Table 4. Results of modal analysis of the unbonded blade.	57

LIST OF FIGURES

Figure 1.1. Blade coordinate system [1].	3
Figure 1.2. Loading directions acting on the blade [2].	3
Figure 1.3. Forces and moments acting over a wind turbine blade [4].	4
Figure 1.4. Wind Turbine Blade in METU RUZGEM	6
Figure 3.1. Blade assembly.	15
Figure 3.2. The blade cross-section at 0.5-meter [16].	16
Figure 3.3. The detailed cross-section at 0.7-meter.	17
Figure 3.4. The detailed cross-section at 1.4-meter.	17
Figure 3.5. Geometric modeling of the blade.	17
Figure 3.6. Three-dimensional model of the blade.	18
Figure 3.7. Bonded regions between (a) Pressure side and suction side (b) Spar and suction side.	19
Figure 3.8. Results of the mesh study in the blade model.	20
Figure 3.9. Meshed model of the blade.	20
Figure 3.10. Lamination plan of the pressure and suction sides of blade.	22
Figure 3.11. Lamination plan of chassis.	23
Figure 3.12. Material lay-up in the cross-section of the blade.	24

Figure 3.13. Contour plot of layer thickness along (a) the blade skin (b) chasis.....	24
Figure 3.14. Layer thickness of the blade skin.....	25
Figure 3.15. Layer thickness for the aeroshell of the blade.	25
Figure 3.16. Load distribution over blade radial position.	27
Figure 3.17. Location of forces in the finite element model.	27
Figure 3.18. Bending moment distribution along blade.	28
Figure 4.1. Mode shapes of the existing blade.	30
Figure 4.2. Total deformation under loading in flapwise direction.	31
Figure 4.3. Stress distribution at the suction side of the blade (a) fiber directions (b) transverse fiber directions (c) shear stresses under flapwise loading.....	32
Figure 4.4. Total deformation under loading in flapwise and edgewise direction.....	33
Figure 4.5. Stress distribution at the suction side of the blade (a) fiber directions (b) transverse fiber directions (c) shear stresses under flapwise and edgewise loading..	33
Figure 4.6. Puck fracture curve [20].	36
Figure 4.7. Contour plots of Tsai-Wu failure reserve factors under flapwise loads from 20% to 100% of the extreme flapwise loading.	37
Figure 4.8. Contour plots of IFF (A) mode for the suction side of the blade under flapwise loads from 20% to 100% of the extreme flapwise loading.....	38
Figure 4.9. Contour plots of IFF (B) mode for the suction side of the blade under flapwise loads from 20% to 100% of the extreme flapwise loading.....	39

Figure 4.10. Contour plots of IFF (C) mode for the suction side of the blade under flapwise loads from 20% to 100% of the extreme flapwise loading.....	40
Figure 4.11. Contour plots of FF mode for the suction side of the blade under flapwise loads from 20% to 100% of the extreme flapwise loading.	40
Figure 4.12. Contour plots of failure exposes of (a) IFF(A) (b) IFF(B) (c) IFF(C) (d) FF for the pressure side of the blade under flapwise loading.	41
Figure 4.13. Contour plots of Tsai-Wu failure reserve factors in the pressure side at flapwise loading.	42
Figure 4.14. Contour plots of failure exposes of (a) IFF(A) (b) IFF(B) (c) IFF(C) (d) FF for the chassis of the blade under flapwise loading.....	43
Figure 4.15. Contour plots of Tsai-Wu failure reserve factors in the chassis at flapwise loading.....	44
Figure 4.16. Contour plots of failure exposes of (a) IFF(A) (b) IFF(B) (c) IFF(C) (d) FF for the internal flange of the blade under flapwise loading.....	44
Figure 4.17. Contour plots of Tsai-Wu failure reserve factors in the internal flange at flapwise loading.	45
Figure 4.18. Contour plots of Tsai-Wu failure reserve factors of the blade under flapwise and edgewise loads from 20% to 100% of the extreme loading.	46
Figure 4.19. Contour plots of IFF (A) mode for the suction side of the blade under flapwise and edgewise loads from 10% to 100% of the extreme loading.	47
Figure 4.20. Contour plots of IFF (B) mode for the suction side of the blade under flapwise and edgewise loads from 20% to 100% of the extreme loading.	48

Figure 4.21. Contour plots of IFF (C) mode for the suction side of the blade under flapwise and edgewise loads from 20% to 100% of the extreme loading.....	49
Figure 4.22. Contour plots of FF mode for the suction side of the blade under flapwise and edgewise loads from 20% to 100% of the extreme loading.	49
Figure 4.23. Contour plots of failure exposes of (a) IFF(A) (b) IFF(B) (c) IFF(C) (d) FF for the pressure side of the blade under flapwise and edgewise loading.	50
Figure 4.24. Contour plots of Tsai-Wu failure reserve factors in the pressure side at flapwise and edgewise loading.....	51
Figure 4.25. Contour plots of failure exposes of (a) IFF(A) (b) IFF(B) (c) IFF(C) (d) FF for the chassis of the blade under flapwise and edgewise loading.	51
Figure 4.26. Contour plots of Tsai-Wu failure reserve factors in the chassis at flapwise and edgewise loading.	52
Figure 4.27. Contour plots of failure exposes of (a) IFF(A) (b) IFF(B) (c) IFF(C) (d) FF for the internal flange of the blade under flapwise and edgewise loading.	52
Figure 4.28. Contour plots of Tsai-Wu failure reserve factors in the internal flange at flapwise and edgewise loading.....	53
Figure 5.1. Failure modes occurred in (a) skin of the blade (b) spar of the blade [7].	56
Figure 5.2. Unbonded blade model.	56
Figure 5.3. Mode shapes of the unbonded blade.....	58
Figure 5.4. Total deformation of unbonded blade under loading in flapwise direction.	59

Figure 5.5. Deformation of the unbonded region of the blade.....	59
Figure 5.6. Stress distribution at the suction side of the blade (a) fiber directions (b) transverse fiber directions (c) shear stresses under flapwise loading.	60
Figure 5.7. Total deformation of unbonded blade under loading in flapwise and edgewise direction.....	61
Figure 5.8. Stress distribution at the suction side of the blade (a) fiber directions (b) transverse fiber directions (c) shear stresses under flapwise and edgewise loading..	61
Figure 5.9. Contour plots of Tsai-Wu failure reserve factors under flapwise loads from 10% to 100% of the extreme loading.....	62
Figure 5.10. Contour plots of IFF (A) mode for the suction side of the blade under flapwise loads from 10% to 100% of the extreme loading.....	63
Figure 5.11. Contour plots of IFF (B) mode for the suction side of the blade under flapwise loads from 20% to 100% of the extreme loading.....	64
Figure 5.12. Contour plots of IFF (C) mode for the suction side of the blade under flapwise loads from 10% to 100% of the extreme loading.....	65
Figure 5.13. Contour plots of FF mode for the suction side of the blade under flapwise loads from 10% to 100% of the extreme loading.....	65
Figure 5.14. Contour plots of failure exposes of (a) IFF(A) (b) IFF(B) (c) IFF(C) (d) FF for the pressure side of the unbonded blade under flapwise loads.	66
Figure 5.15. Contour plots of Tsai-Wu failure reserve factors in the pressure side at flapwise loading.....	67

Figure 5.16. Contour plots of failure exposes of (a) IFF(A) (b) IFF(B) (c) IFF(C) (d) FF for the chassis of the unbonded blade under flapwise loads. 68

Figure 5.17. Contour plots of Tsai-Wu failure reserve factors in the pressure side at flapwise loading. 68

Figure 5.18. Contour plots of failure exposes of (a) IFF(A) (b) IFF(B) (c) IFF(C) (d) FF for the internal flange of the unbonded blade under flapwise loads. 69

Figure 5.19. Contour plots of Tsai-Wu failure reserve factors in the internal flange at flapwise loading. 70

Figure 5.20. Contour plots of Tsai-Wu failure reserve factors under flapwise and edgewise loads from 20% to 100% of the extreme loading. 71

Figure 5.21. Contour plots of IFF (A) mode for the suction side of the blade under flapwise loads from 20% to 100% of the extreme flapwise and edgewise loading. .. 72

Figure 5.22. Contour plots of IFF (B) mode for the suction side of the blade under flapwise loads from 10% to 100% of the extreme flapwise and edgewise loading. .. 73

Figure 5.23. Contour plots of IFF (C) mode for the suction side of the blade under flapwise loads from 20% to 100% of the extreme flapwise and edgewise loading. .. 74

Figure 5.24. Contour plots of FF mode for the suction side of the blade under flapwise loads from 10% to 100% of the extreme flapwise and edgewise loading..... 74

Figure 5.25. Contour plots of failure exposes of (a) Tsai-Wu (b) IFF(A) (c) IFF(B) (d) IFF(C) (e) FF for the pressure side of the unbonded blade under flapwise and edgewise loads. 75

Figure 5.26. Contour plots of failure exposes of (a) Tsai-Wu (b) IFF(A) (c) IFF(B) (d) IFF(C) (e) FF for the chassis of the unbonded blade under flapwise and edgewise loads.	76
Figure 5.27. Contour plots of failure exposes of (a) Tsai-Wu (b) IFF(A) (c) IFF(B) (d) IFF(C) (e) FF for the internal flange of the unbonded blade under flapwise and edgewise loads.	77
Figure 6.1. Stress distribution at the section of 0.7-metre from the root at the skin..	80
Figure 6.2. Stress distribution at the section of 0.7-metre from the root at the spar..	81
Figure 6.3. Stress distribution at the section of 0.7-metre from the root at the internal flange.....	82
Figure 6.4. Contour plots of inverse reserve factors of (a) IFF(A) (b) IFF(B) (c) IFF(C) (d) FF (e) Tsai-Wu for the suction side of the fully-bonded blade under %40 of extreme flapwise and edgewise loading.....	84
Figure 6.5. Comparison of Stress and Inverse Reserve Factor of Puck and Tsai-Wu Failure Criteria at the 0.8-metre of the fully-bonded blade under %40 of extreme flapwise and edgewise loading.....	85
Figure 6.6. Inverse reserve factors of (a) IFF(A) (b) IFF(B) (c) IFF(C) (d) FF (e) Tsai-Wu at the 0.8-metre of the fully-bonded blade under %40 of extreme flapwise and edgewise loading.....	86
Figure 6.7. Inverse Reserve Factors of (a) Puck (b) Tsai-Wu at the 1-metre of the fully-bonded blade under %40 of extreme flapwise and edgewise loading.	87
Figure 6.8. Inverse Reserve Factors of (a) Puck (b) Tsai-Wu at the 2.5-metre of the fully-bonded blade under %40 of extreme flapwise and edgewise loading.....	88

Figure 6.9. Mode shapes of unbonded and fully bonded blade models.	89
Figure 6.10. Total deformation of (a) fully-bonded (b) unbonded blade model under flapwise and edgewise loadings.	89
Figure 6.11. Load displacement curve of the blade corresponding to the fully-bonded and unbonded blade analysis.	90
Figure 6.12. Contour plots of inverse reserve factors between 0.7-1.25 meters at the suction side of the fully-bonded blade for (a) IFF(A) (b) IFF(B) (c) IFF(C) (d)FF ..	91
Figure 6.13. Contour plots of inverse reserve factors between 0.7-1.25 meters at the suction side of the unbonded blade for (a) IFF(A) (b) IFF(B) (c) IFF(C) (d)FF ..	92
Figure 6.14. Inverse reserve factors ply-by-ply at the sample element of the fully-bonded blade for (a) IFF(A) (b) IFF(B) (c) IFF(C) (d)FF ..	93
Figure 6.15. Inverse reserve factors ply-by-ply at the sample element of the unbonded blade for (a) IFF(A) (b) IFF(B) (c) IFF(C) (d)FF ..	94
Figure 6.16. Stress distributions along suction side of the fully-bonded blade model between 0.7 and 1.25-metre (a) in fiber direction (b) in the transverse fiber direction (c) shear stress.	95
Figure 6.17. Stress distributions along suction side of the unbonded blade model between 0.7 and 1.25-metre (a) in fiber direction (b) transverse fiber direction (c) shear stress.	95
Figure 6.18. Stress distributions along trailing edge (a) in fiber direction (b) transverse fiber direction (c) shear stress.	96
Figure 6.19. Stress distributions along trailing edge between 0.7 and 1.25-metre (a) in fiber direction (b) transverse fiber direction (c) shear stress.	97

LIST OF SYMBOLS

B	The number of blades in the rotor
$c(r)$	The airfoil chord distribution
c_L	The lift coefficient
c_D	The drag coefficient
Q	Torque
r	Blade radius

ABBREVIATIONS

FF Fiber failure

IFF(A) Inter fiber failure for Mode A

IFF(B) Inter fiber failure for Mode B

IFF(C) Inter fiber failure for Mode C

CHAPTER 1

INTRODUCTION

In this chapter, composite wind turbine blades are discussed in detail. In Section 1.1, construction and materials of wind turbine blades are defined and examples are given. In Section 1.2, the damage problem in the wind turbine blades is defined. In Section 1.3, the scope of this thesis is presented.

1.1. Wind Turbine Blades

Composite rotor blade is the one of the significant parts in wind turbine structure. Structural design of the blade is important for reliability and safety of the wind turbine. The strength of the blade depends on material and construction of the blade [1]. The detailed information about wind turbine construction, materials and loads is given in the following sections.

1.1.1. Wind Turbine Blade Construction

In the wind turbine blades, there is more lifting force at the tip of the blade than the root region. The lifting force inclines to bend the blade, so these forces cause bending moment along blade. The maximum bending moment occurs at the root of the blade while it is equal to zero at the tip of the blade, causing the blade to have the maximum strength at the root region and the thickness of the blade to decrease towards the tip. Therefore, the blade has a thinner section at tip where the drag force is crucial. As it happens, the thickness of the blade should be selected to make the blade stiff and strong enough to maximize lifetime. So, the chassis which has a box shape in general is used

in the inside of the blade to minimize the weight of the blade and the loss in aerodynamic efficiency. The blade with a chassis has a three-cell section with two shear webs.

In general, the aeroshell of the blade is composed of three different layers as a gel-coat layer, a foam layer and a double-bias-material composite laminate. Smooth surface conditions are provided by the gel coat layer which is not a structural material. Foam layer is a protective shield for double-bias laminate. The core-material laminate increases strength against the buckling at the trailing section of the blade.

The thickness values of the unidirectional laminate, double-bias laminate, and core material are critical for designing a wind turbine blade. The blade has to be as light as possible and reliable under extreme load distribution. The weight of the blade is directly proportional to the cubic of the blade length. The most suitable construction method should be selected for the optimum weight-length ratio [2].

All forces and moments must be defined clearly for the validation and the design of the blade. The directions of all forces and moments at the blade are shown in Figure 1.1 [1]. The origin of the blade coordinate system is the intersection of the blade root and pitch axis of the blade. YB is in the direction of the trailing edge of the blade and parallel with the chord line of the blade. ZB points forward from the origin to the pitch axis through the tip of blade. XB is perpendicular to YB and ZB axes. FXB, FYB and FZB are flapwise force, edgewise force and force along the blade, respectively.

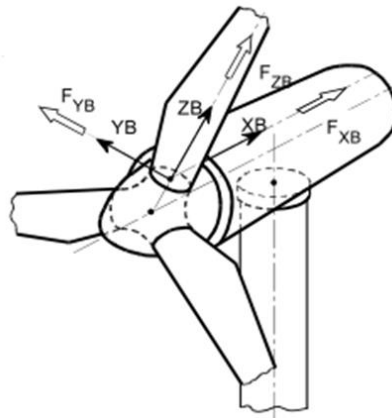


Figure 1.1. Blade coordinate system [1].

1.1.2. Loads on Wind Turbine Blade

There are two types of loads which have effect on the wind turbine blades. These are aerodynamic loads (drag, shear, lift, etc.) and internal loads (gravity, blade dynamic, etc.). These forces occur in flapwise and edgewise direction as shown in Figure 1.2.

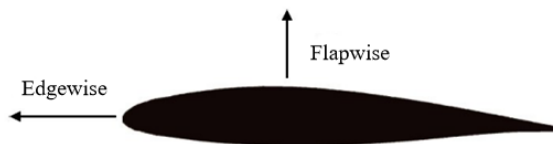


Figure 1.2. Loading directions acting on the blade [2].

Wind loads induce significant bending moments at the blade. Bending moments occur in the flap direction. All forces and moments which are exerted on the blade are shown in Figure 1.3. F_T is the thrust force related to the wind speed V_{ref} . F_g represents the gravity force. F_c is the centrifugal force which depends on the rotational speed. The total bending moment due to thrust in the flapping direction and the bending moment due to thrust in the edgewise direction are represented as $B_{M,T}$ and $B_{M,Q}$ respectively [3].

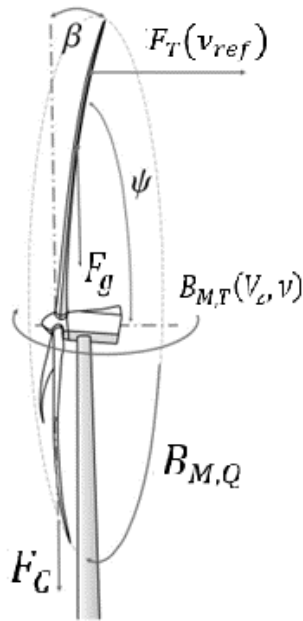


Figure 1.3. Forces and moments acting over a wind turbine blade [4].

1.1.3. Materials Used in Wind Turbine Blades

Composites are frequently used often for designing wind turbine blade. A composite material consists of two or more materials combined to obtain properties different from those of the individual materials. In general, fiber and matrix structures are used in a composite lay-up of the wind turbine blade. Fiber and matrix properties are important and discussed in the following section [5].

Fibers

Fibers are preferred for strengthening the wind turbine blade structure and enhancing the rigidity. The most common fiber type is glass fiber. Popularity of the fibers is increasing, because fibers are getting cheaper and getting easier to produce. Fibers are also lighter than other materials. They have hollow structure with very low density.

Matrix Materials

The main goal of using matrix materials is holding and protecting fiber layers. Usually, some types of matrix materials like thermosets (i.e. epoxies, polyesters) or thermoplastics are used with a matrix form in the wind turbine blade composite structure.

1.2. Wind Turbine Blade in METU RUZGEM

The existing blade was designed as part of a project co-executed by RUZGEM – METU Center for Wind Energy and Core Team of the University of PATRAS according to IEC 61400-2 [6]. The blade was designed for a wind turbine having 30 kW nominal power capacity at 10 m/s wind speed. According to the wind turbine characteristics, the blade optimized aerodynamic and geometric design were finalized by the blade manufacturer. The existing blade is depicted in Figure 1.4.

The main objective of the METUWIND project is to design and manufacture an aerodynamically optimized rotor blade, which is light, reliable and suitable for working under strong wind conditions. The blade design process is initiated by the aeroelastic design load calculations. The optimized aerodynamic design was completed by Smartblade GmbH; they have provided detailed geometry and aeroelastic sectional stress resultant distributions for several extreme IEC loading cases. After calculating the loads, 4 campaigns of static tests were performed to characterize in-plane mechanical properties of GFRP composites, which is used in the design and manufacturing of wind turbine rotor blades. Materials which are used in blade are selected. Finally, the structural design of the blade under extreme loads and life prediction calculations for a typical 20-minute load time series were performed by the CORE team of the University of Patras. Design of the blade includes the internal “hat shaped” FRP spar beam structure, the joint design at the hub as well as the composite shells. Structural analysis of the blade was performed using ANSYS

FE commercial code and proprietary software of the CORE team for static and fatigue analysis of rotor blades. The connection of the blade to the metallic hub is realized through 12 M16x1.5 bolts of class 8.8.



Figure 1.4. Wind Turbine Blade in METU RUZGEM

1.3. Problem Definition in Wind Turbine Blades

The most significant parts of a wind turbine are the blades. Blades must withstand excessive loading conditions and material fatigue along the expected operational life. When a damage occurs in the blade, extra repair time is required causing extra time loss and increasing cost. Thus, blade damage is the most critical problem for a wind turbine. The composite wind turbine blades should be designed against damages due to extreme loading conditions.

Full-scale tests of the blade should be done to ensure the blade strength. In literature, there are a lot of examples of full-scale testing of the composite wind turbine blade. These examples show some major damages on blade such as skin/adhesive delamination, adhesive joint failure of leading or trailing edges, sandwich face/core delamination, delamination of laminates, failure in individual laminas, skin layer/adhesive delamination, gelcoat damage etc. [7].

This study presents two objectives to obtain strength behavior of an existing 5-meter composite wind turbine blade:

1. To develop a finite element model of an existing 5-meter wind turbine blade to investigate the structural integrity of the blade under flapwise and edgewise design loading conditions.
2. To compare the structural behavior of the existing wind turbine blade with a defect by introducing an unbonded region of the trailing edge.

1.4. Scope of The Study

The organization of this thesis can be given as follows:

- In Chapter 2, a brief literature survey about wind turbines blades is presented. The focus is given to the damage investigation of the wind turbine blades.
- In Chapter 3, the existing blade and loading conditions are given. Also, finite element analysis of the blade is presented in detail.
- In Chapter 4, modal, static and failure analyses subjected to the existing blade model are presented.
- In Chapter 5, modal, static and failure analyses subjected to the unbounded blade model are presented are presented.
- In Chapter 6, the results related to different cases are discussed.
- In Chapter 7, the conclusions from this study are discussed. Also, possible future works are proposed.

CHAPTER 2

LITERATURE SURVEY

In this chapter, studies in literature for “damage on wind turbine blades” are investigated in detail.

2.1. Damage on Wind Turbine Blades

A good investigation of composite structure, materials and adhesives in the blade helps to the prediction of wind turbine reliability. Thus, there is a lot of studies about wind turbine damage in literature. Studies are discussed in chronological order.

In [8] Leeuwen et. Al., a 37-meter composite wind turbine blade and coupons of identical materials of that blade are tested under static flapwise loading and fatigue loads to understand of the blade fatigue strength and obtain S-N Curve of the blade materials. After tests are completed, large deformation and crack development are shown on the skin of the blade. The results of testing of the blade and coupons of the materials are compared. The study shows that the fatigue behavior of the blade can be predicted by coupon tests.

In [9] Jensen et. al, full-scale test of a 34-metre composite wind turbine blade is performed under only flapwise loading. Ovalization of the spar caps of the blade is measured during the test and the test simulated with non-linear finite element analysis. The ovalization of the spar caps because of a crushing pressure is called as The Brazier effect. This effect is captured in full-scale testing measurements and finite element analysis, also. Results of tests and analysis shows that the initial failure is the debonding of the outer skin of the blade. And, failure continues with the delamination

in the blade skin. After debonding and delamination, the final collapse occurs in the spar caps of the blade.

In [7] Sørensen et al. focused on damage which is occurred in adhesive joint in the composite wind turbine blade. The durability of the adhesive joints in the blade are important for predicting the damage. Study demonstrates the methodology for understanding the characteristic of the adhesive joints in the blade. Additionally, the laboratory data usage in that methods are investigated. Data obtained from tests is used to predict the crack growth resistance.

In [10] Philippidis et. al, in order to predict behavior of a wind turbine blade under static loading, three main methods are considered: approaches for the determination of material properties, approaches for lifetime, residual strength and failure of the blade, analysis of the effect of fiber and matrix of composite lay-up of the blade. In this study, composite coupons are tested under different loading, temperature, frequency and orientation conditions for the determination of material properties. Additional to these composite coupons tests, a numbers of experiment approaches are investigated to determine of the shear strength of adhesive. For instance, V-notched rail shear and strap method for adhesive joint is examined and the highest shear strength is obtained by this method. Also, some concepts are inspected for life prediction, residual strength and stiffness of the blade. In this study, an isotropic non-linear constitutive model implementing progressive damage concept is expressed. This concept is performed to simulate fatigue damage process in a composite laminate. Furthermore, the effects of fibers and matrix of blade materials on their strength and damage resistance are investigated. It is concluded that a weak fiber-matrix interface causes the development crack development in the composite laminates. Overall, the study shows that the microscale analysis and fiber-matrix optimization play an important for the optimization of materials used in the blade.

In [11] Zhou et al., a 40-meter composite wind turbine blade is analyzed by using finite element method. The analyzed are performed under static loading conditions. The results of analysis show that the stresses occur in the spar caps and the root of the blade is higher than stresses in shear webs and skin of the blade. The study demonstrates that spar caps and the root are the main load-carrying components of the blade.

In [12] Jin et al, a 2 MW composite wind turbine blade is designed by using finite element modelling. A new approach that is called as one-way fluid-structure interaction method is presented based on modified Blade Element Momentum theory. This approach is a combination of finite element analysis and particle swarm algorithm to optimize a composite wind turbine blade. The proposed method allows the thickness and spar cap location variation along the blade. The study shows that the mass is decreased in optimized blade design.

In [13] GUTU Marin et al, a final design of a blade for 10 kW wind turbine is presented by finite element analysis. This final design is reached over an iterative analysis process by a previous design. The objective of this paper is that the structural strength of the blade is increased by the mass and cost of the blade is decreased. The final design is checked by finite element analysis subjected to static and dynamic behavior of the blade. In the study, design variables are fiber directions, lay-up directions, and thickness of the blade. The constrains of the study are deformations on the tip, stresses and resonant vibration of the blade. Due to results of finite element analysis, the finalized design of the blade is stiff enough to harsh weather conditions i.e. storms, and the blade operates out of dangerous resonance frequencies. Also, the optimized blade is approximatively 20% lighter.

In [14] Lee et al., a 48.3-meter composite wind turbine blade is tested under static and fatigue loading conditions in accordance with IEC TS 61400-23 standard. The static tests have four loading conditions: positive flapwise directions, negative flapwise directions, positive edgewise directions, negative edgewise directions. After static

tests, a fatigue test of a full-scale test is performed. For the fatigue test, the number of test cycles is one million for the flapwise loading and two million for the edgewise loading. After the static and fatigue tests, the third test is performed to collapse the blade and the blade collapsed under 70% of the maximum negative flapwise loading. After the collapse test, spar cap in the pressure side of the blade is broken, and two shear webs are cracked obliquely and longitudinally. Likewise, there is a debonding in the trailing edge of the blade. The study states that the main reason of failure in shear webs is compressive buckling. The longitudinal cracks in the shear webs is caused by transverse forces, and the oblique cracks in the shear webs is caused by shear forces. The Brazier effect which means ovalization of the cross-section of the blade causes transverse forces, however it is not a root cause because blade cross-section experienced larger loads during in positive flapwise loading test. Bending and torsion occur shear stresses in the shear webs. If bending is the root cause, the oblique cracks in the two shear webs should be parallel, however the cracks are not parallel in the shear webs, they are transversal. Only torsion can create the observed oblique cracks. However, if debonding occurs in the trailing edge of the blade, the shear stresses cannot flow along the blade skin and they flow between the trailing edge and the second shear web. This process creates torsion in shear webs. Consequently, the study demonstrates that main failure mechanism is debonding of the trailing edge of the blade cross-section.

In [15] Chen et. al, a 52.3-metre composite wind turbine blade is tested under static flapwise and edgewise loading conditions. These loadings are determined according to IEC 64100-23 standard. When loading reaches almost 90% of the extreme loading, the blade collapsed in root transition and near-tip region around the loading clamp. The test was recorded by video camera. Thus, the process of collapse could be examined particularly. First of all, during test the crack sound occurred and blade started to vibrate. And then, failure in the root region of suction side was occurred. Secondly, the root region deforms upwards. In the meantime, the failure of trailing

edge and aft panels in the root transition region was observed. Then, global deformation progressed to the sections between the last loading clamps. It is observed that a deformation occurs in the middle span of the blade, which is caused by the failure of the RT region. Finally, trailing edge failure is observed in the middle span of the blade and in the region near the last loading clamp. Meanwhile, the blade tip starts to bend. The failure occurs in the near-tip regions in the subsequent time steps. The near-tip region failure is caused by high bending during collapse. Generally, the strains in the near-tip region must be low at the static load level at blade collapse. However, the impact loads generated by the blade collapse could be affected by dynamic strains to the near-tip region and cause damage. To understand the root transition region failure, material stacking sequence must be examined. In the blade manufacturing process, for resin infusion, thick unidirectional composites are placed into the blade mold. However, that unbalanced construction has a negative effect on the buckling strength. Also, in this study, numerical analyzes are performed to examine the failure process of the blade during the loading. First of all, linear buckling analysis is performed on the root transient region of the blade. In the second analysis, progressive failure analysis technique is used to predict major failure modes of the blade. Additionally, a detailed three-dimensional strain analysis is performed to examine failure characteristics. The analyzes results show that major failure characteristics are well captured to the test results by the finite element analysis.

CHAPTER 3

FINITE ELEMENT MODEL OF WIND TURBINE BLADE

In this chapter, finite element modeling of the existing 5-meter composite wind turbine blade is defined in detailed. In Section 3.1, the three-dimensional geometric modelling of the blade is described. In Section 3.2, mesh and contact definitions in the finite element model are given. In Section 3.3, the materials that are used in blade structure are explained. The material model of the blade is given. In Section 3.4, the loads and boundary conditions are given.

3.1. Geometric Modeling of The Blade

The existing blade consists of four main parts: suction side, pressure side, internal flange, “hat shaped” chassis (spar), and flange; as given in Figure 3.1. Total length of the blade is 5 meters. Two shear webs part of a “hat shaped” chassis and the internal flange are placed in the blade, starting at 0.5 meters away from the root and extending up to 4 meters. The root diameter of the blade is equal to 273 mm.

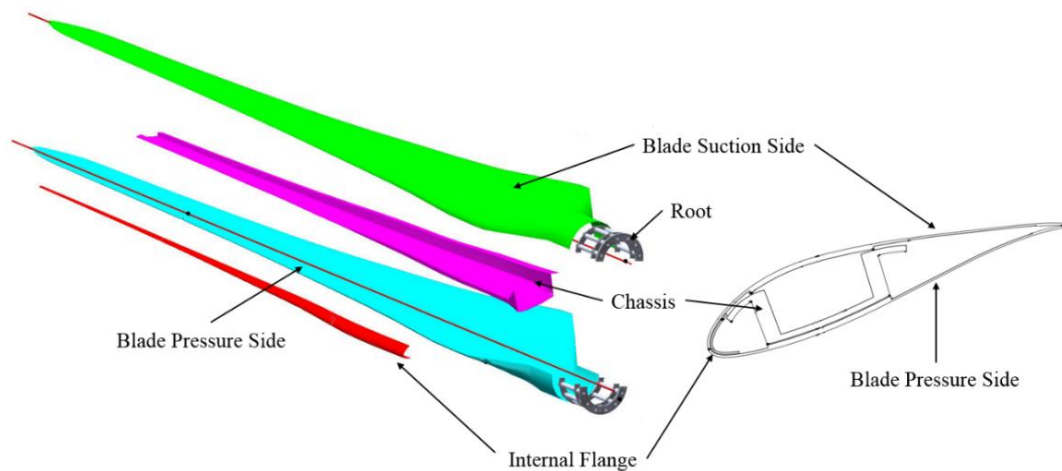


Figure 3.1. Blade assembly.

In Figure 3.2, cross-section at 0.7-meter of the blade is given. The thick lines show the chassis (spar). Two shear webs of chassis (spar) divide the blade section into three parts. From the left to the right, these sections can be called as the leading edge, the spar cap and the trailing edge. The spar cap and the shear webs are designed as a hat-shape form to improve the flapwise stiffness of the blade. Two shear webs of chassis (spar) are perpendicular to the chord of the cross-section and are located at 50% and 85% respectively of the airfoil chord from the trailing edge. The widths of each spar cap flanges on the suction side of the blade are designated as 7% of the airfoil cord respectively.

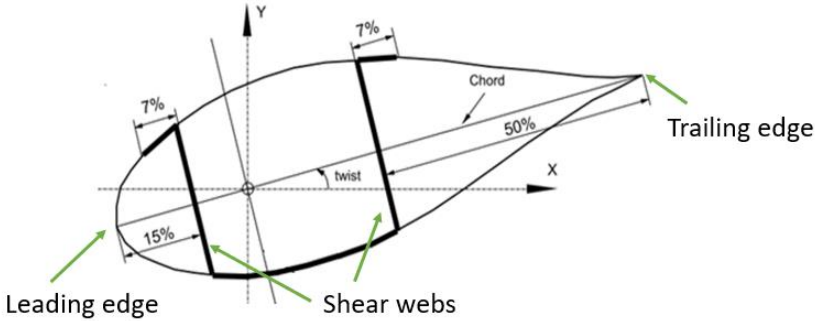


Figure 3.2. The blade cross-section at 0.5-meter [16].

The two-dimensional blade drawings which include the blade aerodynamic design details such as cord length and twist angle along the blade were provided by the blade designer. The given cross-section details at the different sections are given in Figure 3.3 and Figure 3.4. The blue lines define internal flange. Green lines and hatched define foam. The magenta lines define adhesive area.

After sketching, the cross-sections are combined along blade chord direction by using “Explode” command in NX 10.0 environment. The three-dimensional model of the blade is given in Figure 3.6.

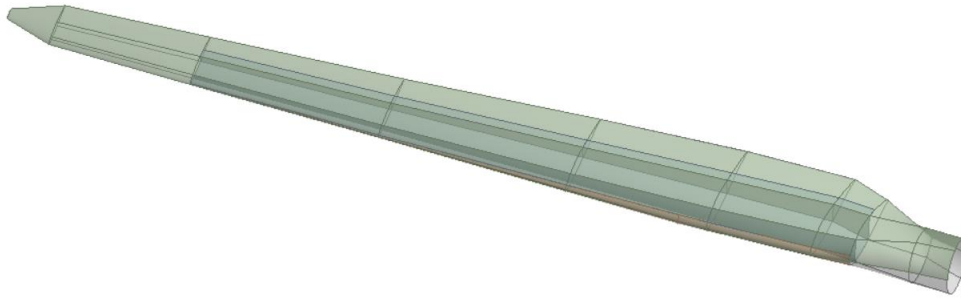


Figure 3.6. Three-dimensional model of the blade.

3.2. Contact Definitions

Each component of the blade (suction side, pressure side, internal flange and chassis) is built in a different mold and then they assembled by using adhesive. In the finite element model of the blade, the regions where adhesive is located are modelled as bonded contact. The bonded contacts are between;

- Internal flange and pressure side,
- Internal flange and suction side,
- Spar and pressure side,
- Spar and suction side,
- Pressure side and suction side.

Bonded areas between pressure side and suction side, and between spar and suction side are given in Figure 3.7.

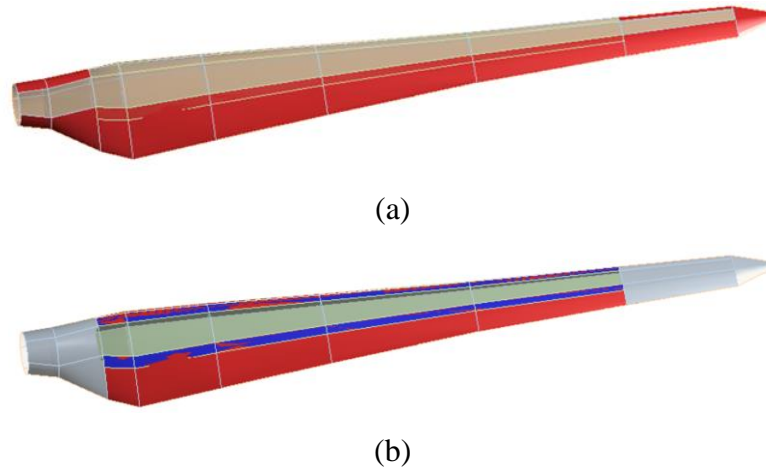


Figure 3.7. Bonded regions between (a) Pressure side and suction side (b) Spar and suction side.

The adhesive is modelled as 15 kg point mass to keep blade total mass constant. The point mass is located at the center of gravity of the blade and distributed the areas where the adhesive is.

3.3. Mesh Convergence

The S4R linear quadrilateral elements (SHELL181) are used for finite element modeling of the blade in ANSYS Workbench environment [17]. Furthermore, mesh convergence is performed on the blade. The tip deflection is used as the convergence criterion. Figure 3.9 shows the results of mesh converge. It is found that the suitable mesh is created with 225,224 layered shell elements and 229,753 nodes.

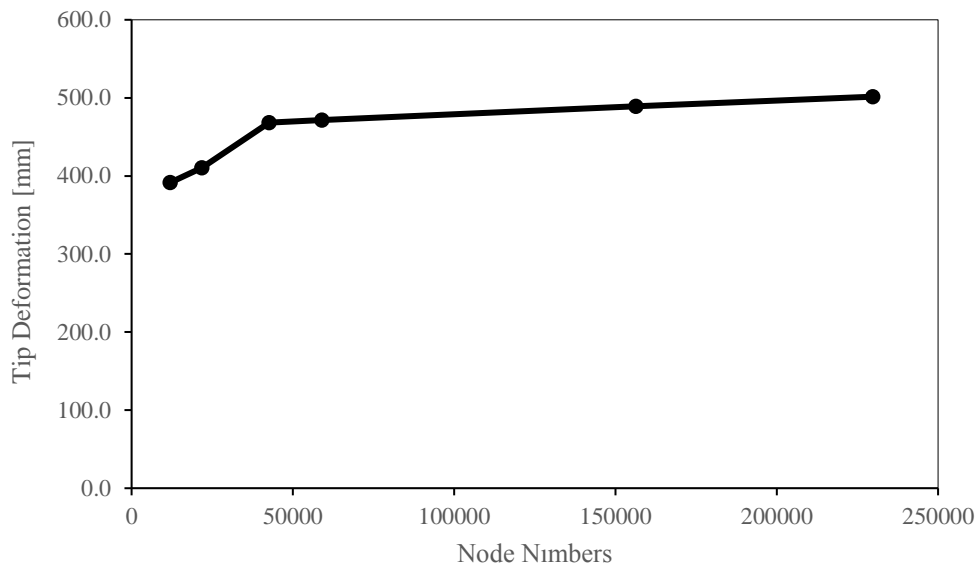


Figure 3.8. Results of the mesh study in the blade model.

The meshed blade is given in Figure 3.9.

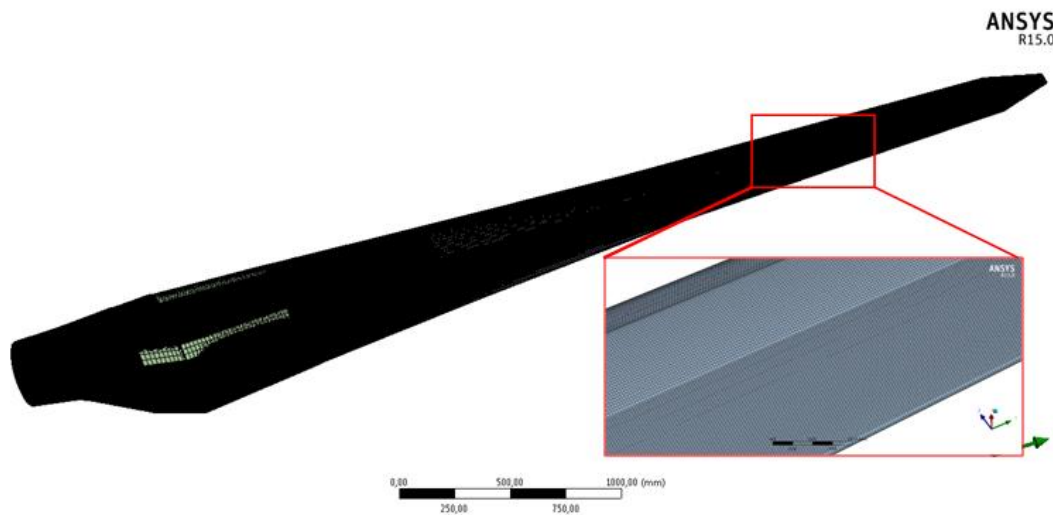


Figure 3.9. Meshed model of the blade.

3.4. Material Layout of The Blade

In the existing blade, gel coat, chopped strand mat (CSM 300), steel, polymeric foam (Divinycell H45) and two fiberglass composite materials are used. These glass/epoxy composites are: unidirectional laminate and tri-axial laminate. The unidirectional laminate is called METYX L600E10C-0 of 623 g/m² with parallel continuous fibers. The second glass fabric, METYX XL800E10F-[0/45/-45] of 835 g/m², is a tri-axial architecture with fibers in the 0, +45° and -45° directions in a ratio of 2:1:1.

Table 1 lists the experimental material properties of the blade materials.

Table 1. Material properties.

Material Property		Unidirectional Laminate	Steel	Gel Coat	CSM 300	Divinycell H45
Density, ρ	[kg/mm ³]	1896	7850	1200	1896	200
Thickness	[mm]	0.716	5.3	0.9	0.358	5–10
E ₁	[GPa]	24.84	210	1.95	4.47	0.269E-03
E ₂	[GPa]	9.14				
ν_{12}		0.29	0.3	0.17	0.14	0.2
G ₁₂	[GPa]	2.83				7.35E-03
X _T	[MPa]	191.73	581.8	35.29	16.86	1.4
X _C	[MPa]	101.16				0.6
Y _T	[MPa]	16.86				1.4
Y _C	[MPa]	50.41				0.6
S	[MPa]	11.29				0.56

The lamination plan of the pressure and suction sides of the blade is presented in Figure 3.10. The lamination plan is:

- The outer surface of the blade is covered with transparent Gel Coat and a layer of chopped strand mat, 300 g/m² CSM 300.
- The root part of the blade is composed of unidirectional laminates, tri-axial laminates and steel.

- The lay-up sequence for the pressure and suction side differs only in the area from 1.25m to 2m where an additional unidirectional glass fabric was placed in the suction side of the blade.
- The Divinycell H45 foam used in the trailing edge is of 10mm thickness in the area from 0.7 meters to 2 meters and 5mm thickness from 2 meters to 3 meters.



Figure 3.10. Lamination plan of the pressure and suction sides of blade.

The stacking sequence of the chassis is presented in Figure 3.11. The stacking sequence is:

- Only triaxial fiber is used in the chassis.
- The 10 mm thickness Divinycell H45 foam is used in the spar cap in the 10th layer.

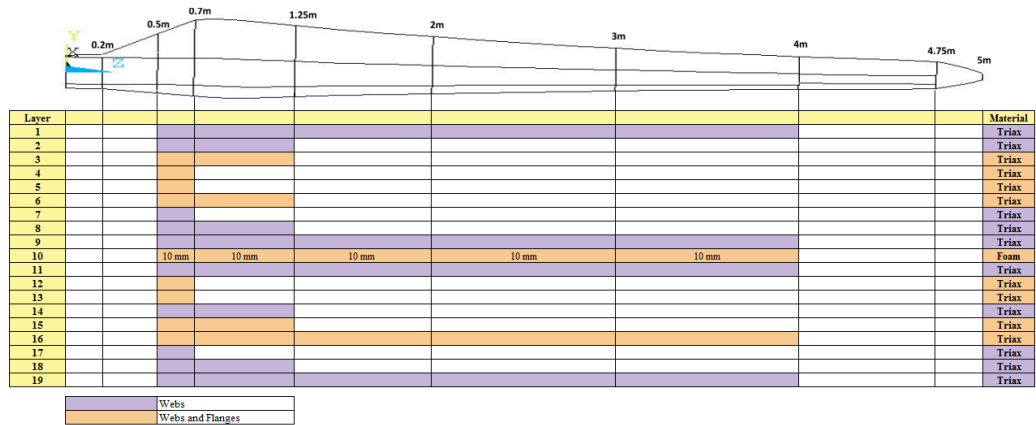


Figure 3.11. Lamination plan of chassis.

The layers have different thicknesses along blade. The thickness of materials of the blade are as follows:

- Unidirectional laminate with a thickness of 0.716 mm
- Tri-axial laminate [0/45/-45] with a thickness of $h_{0TRI} = 0.483\text{mm}$, $h_{+45TRI} = 0.238\text{mm}$, $h_{-45TRI} = 0.238\text{mm}$.
- Steel with a thickness of 5.3 mm
- Gel Coat with a thickness of 0.9 mm
- CSM 300 with a thickness of 0.358 mm
- The polymeric foam, Divinycell H45 of DiAB group, with thickness varies from 5mm to 10mm

The composite material lay-up of the blade is defined in ANSYS ACP/Pre module [18]. The layers are aligned along inside the blade surface as shown in Figure 3.12.

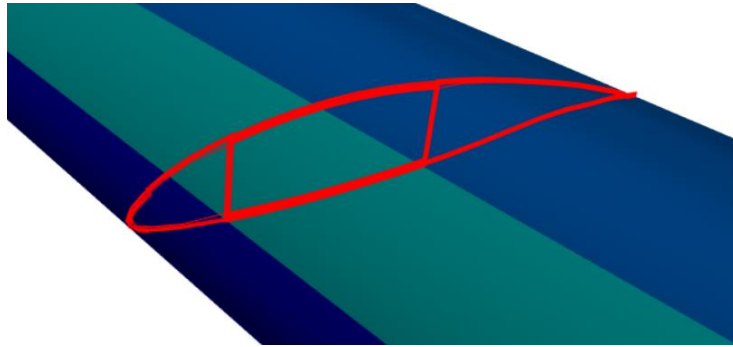
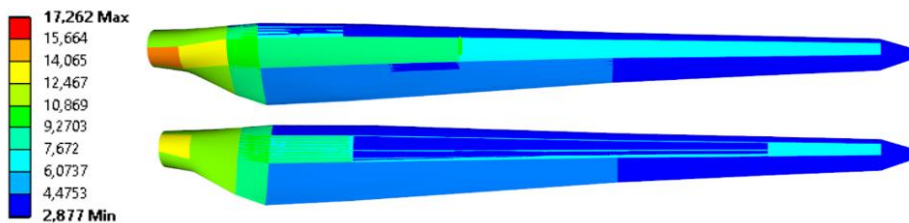
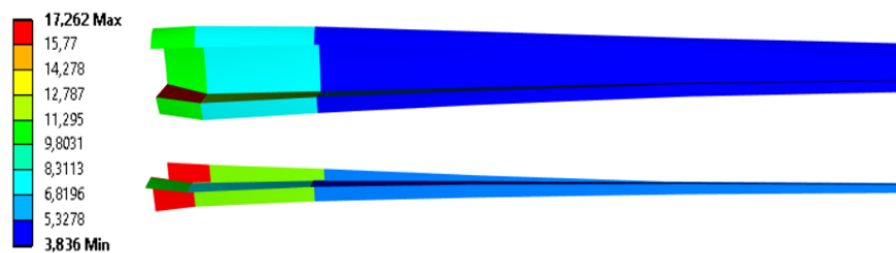


Figure 3.12. Material lay-up in the cross-section of the blade.

With respect to different lamination plan for different blade section, the composite layer thickness change is given in Figure 3.13 . The dark blue areas are the thinnest regions while light blue areas are thicker regions. The thickest region is root transient area between 0 to 0.2-metre, as shown in orange.



(a)



(b)

Figure 3.13. Contour plot of layer thickness along (a) the blade skin (b) chasis.

The composite layer thickness in the aeroshell of the blade changes as seen in Figure 3.14 from the root to the tip of the blade. The maximum thickness is at the near root area.

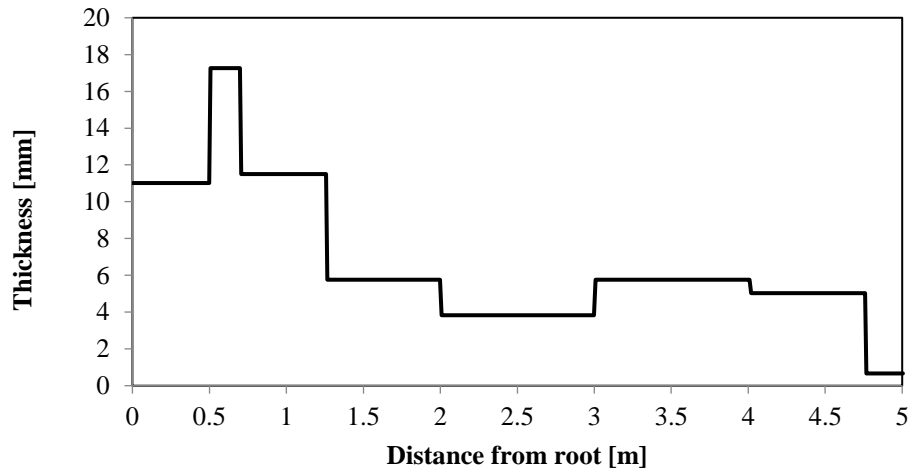


Figure 3.14. Layer thickness of the blade skin.

The composite layer thickness in the chassis of the blade is given in Figure 3.15 from the root to the tip of the blade. As aeroshell thickness distribution, the maximum thickness in the chassis is at the near root area.

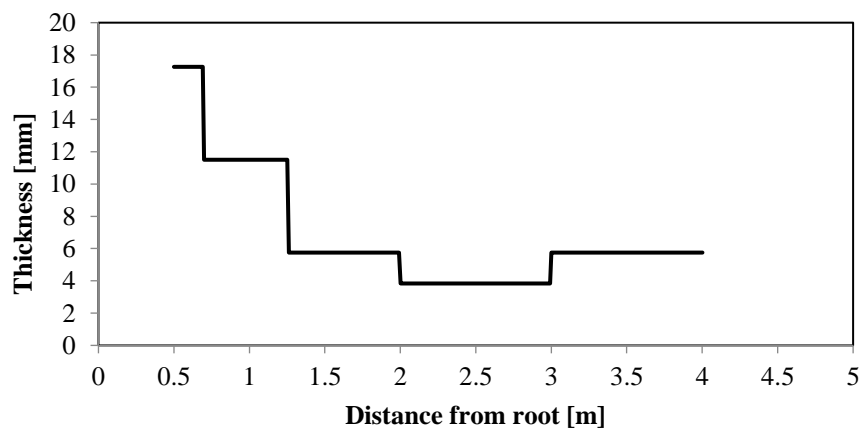


Figure 3.15. Layer thickness for the aeroshell of the blade.

The total mass of the blade including the adhesive paste, the Gel Coat and the CSM 300 finishing ply is 83.41 kg.

3.4. Loading Conditions

There are two important aerodynamic forces acting on a wind turbine blade: drag and lift. Drag force applies on the blade in the direction of the relative wind flow, while lift force applies in a perpendicular direction to the relative wind flow. The drag and lift forces depend on wind speed and wind speed is calculated from meteorological data in Ankara. These are analyzed so that, average wind speed, occurrence of gusts and wind speeds are determined. Based on this information the turbine specifications are selected according to IEC 61400-2 standard [7]. Worst case load scenario is chosen among the complete set of IEC extreme loads provided from aero-elastic simulations. The extreme loads are computed using the wind turbine aero-hydro-servo-elastic software tool FAST version v7.01.00a-bjj. During the simulations the turbine is simulated as a stall regulated constant speed turbine at 83 rpm with a gearbox and simple induction generator. Using this data, the blade is analyzed under extreme loads in the flapwise and edgewise direction including a safety factor of 1.35. These loads are given in Table 2.

Table 2. Flapwise and edgewise loads over blade radial position.

R [m]	Flapwise Loads [kN]	Edgewise Loads [kN]	R [m]	Flapwise Loads [kN]	Edgewise Loads [kN]
0,00	8,14	2,44	2,75	2,95	0,51
0,70	7,03	1,78	3,00	2,6	0,44
0,80	6,82	1,68	3,25	2,26	0,36
0,90	6,62	1,57	3,50	1,93	0,3
1,00	6,4	1,51	3,75	1,6	0,23
1,25	5,85	1,34	4,00	1,29	0,17
1,50	5,3	1,17	4,25	0,97	0,12
1,75	4,75	1,01	4,50	0,66	0,08
2,00	4,2	0,84	4,75	0,34	0,04
2,25	3,76	0,72	4,90	0,15	0,01
2,50	3,35	0,61			

Loads are placed at 21 stations along the blade in finite element modelling, which is presented in Figure 3.10

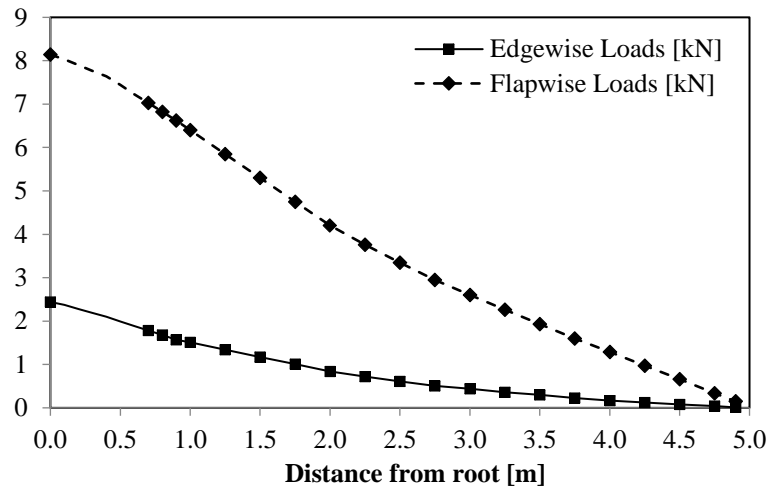


Figure 3.16. Load distribution over blade radial position.

This set of forces is subsequently implemented in the finite element model. Specifically, the forces are applied to nodes lying in both the pressure and suction side as presented in Figure 3.17.

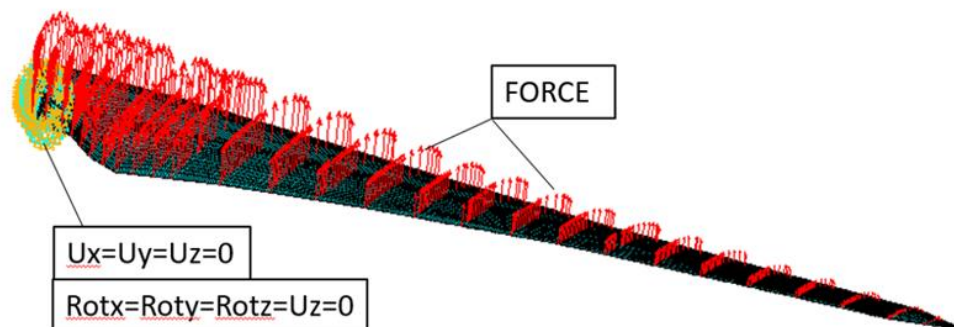


Figure 3.17. Location of forces in the finite element model.

The moment distribution along blade is given in Figure 3.18.

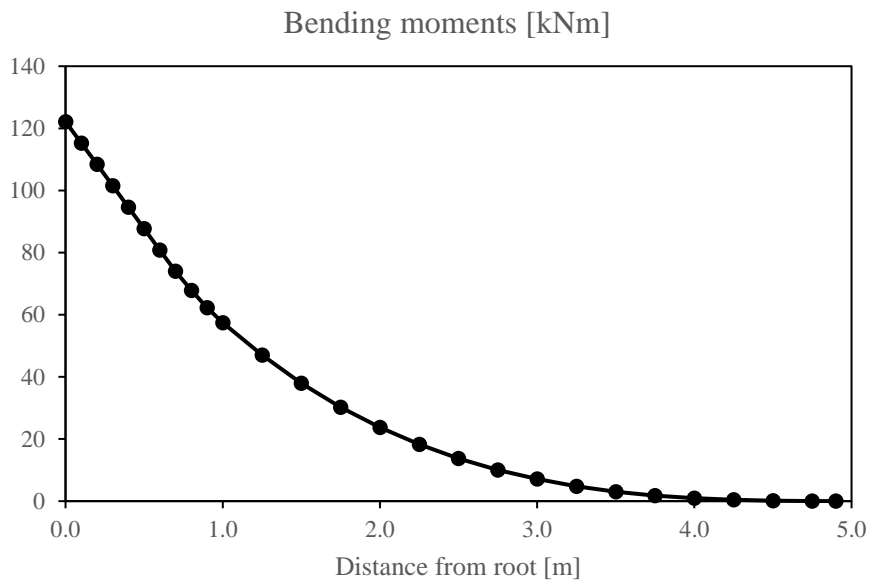


Figure 3.18. Bending moment distribution along blade.

CHAPTER 4

STATIC AND FAILURE ANALYSIS OF THE FULLY-BONDED BLADE

In this chapter, modal and static analysis of the existing blade are performed in order to obtain static and dynamic behavior of the blade. In Section 4.1, the natural frequencies and the mode shapes of the blade are estimated. The results of the static analysis are presented under two loading conditions: only flapwise, both flapwise and edgewise loading conditions in Section 4.2 and Section 4.3, respectively.

4.4. Modal Analysis

It is necessary the natural frequencies of a wind turbine blade in order to be resistance in terms of instability in wind turbines. In general, natural frequencies are interpreted by comparing with wind turbine speed. However, in this study, natural frequencies are compared between fully-bonded and unbonded blade model. To estimate the mode shapes and natural frequencies of the existing blade, a modal analysis is performed in ANSYS Workbench. In the modal analysis, the blade is fixed at the root by fixing all degree of freedom. Table 3 presents the results of the modal analysis that calculated the natural frequencies for bending modes in the edgewise and flapwise directions. The mode shapes of the blade are given in Figure 4.1. The maximum natural frequency occurs in the torsional movement of the blade. So, this mode shape must be taken into account when the wind turbine will be designed.

Table 3. Results of modal analysis.

Mode Shapes		Natural Frequencies [Hz]
1 st Mode Shape	1 st Flapwise Bending	5.3
2 nd Mode Shape	2 nd Flapwise Bending	9.3
3 rd Mode Shape	3 rd Flapwise Bending	20.4
4 th Mode Shape	4 th Flapwise Bending & 1 st Edgewise Bending Coupling	35.2
5 th Mode Shape	5 th Flapwise Bending & 2 nd Edgewise Bending Coupling	42.2
6 th Mode Shape	3 rd Flapwise Bending & 1 st Torsion Coupling	53.4

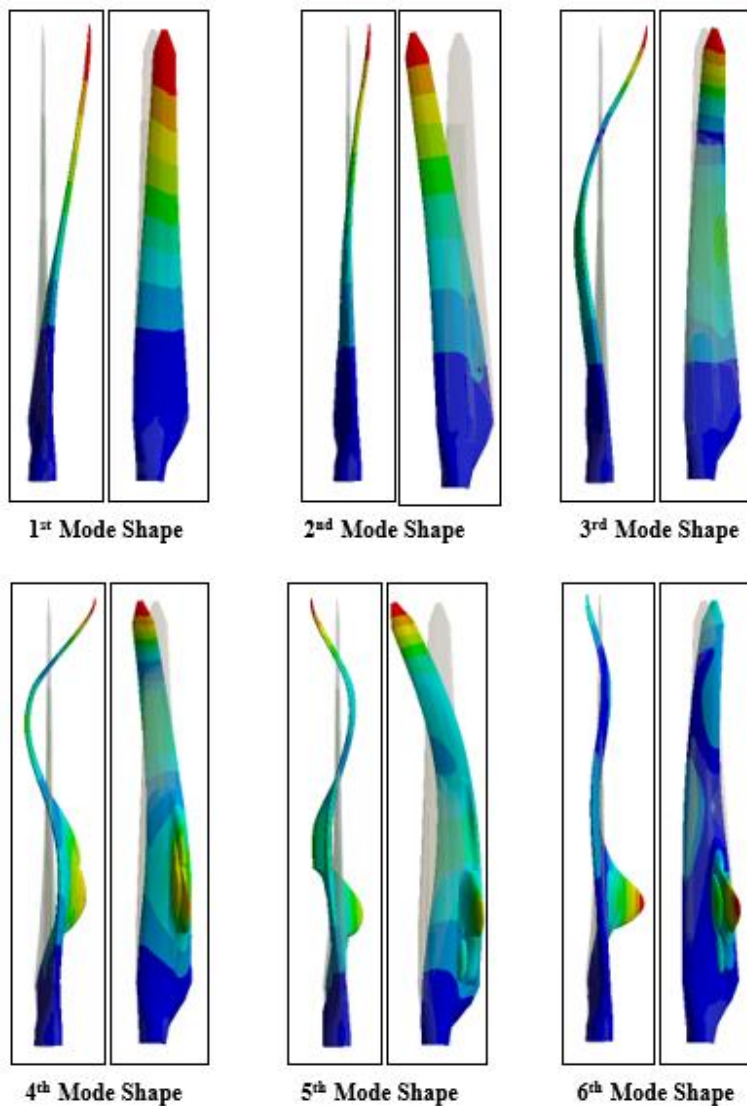


Figure 4.1. Mode shapes of the existing blade.

4.5. Static Analysis

The results for the static analysis under two loading conditions are presented following sections. The detailed investigation about static analysis is given in Chapter 6.

4.5.1. Flapwise Analysis

In the flapwise analysis, the blade root is fixed all six degree of freedom and flapwise loads are given in Figure 3.16 are applied along the blade. The total deformation is almost 0.4-meter in the flapwise direction at the tip of the blade as given in Figure 4.2. In the edgewise direction, there is a small deflection because of the twist angle of the blade.

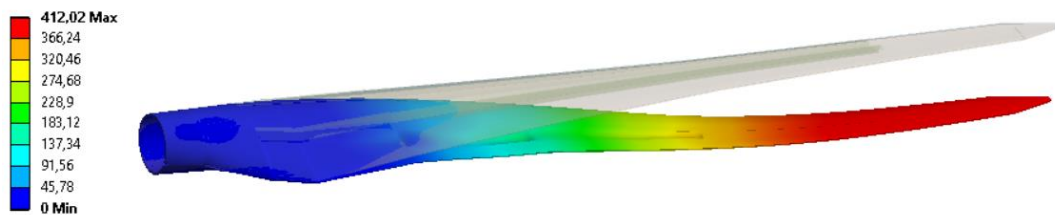


Figure 4.2. Total deformation under loading in flapwise direction.

The stress distribution along blade is given in Figure 4.3.

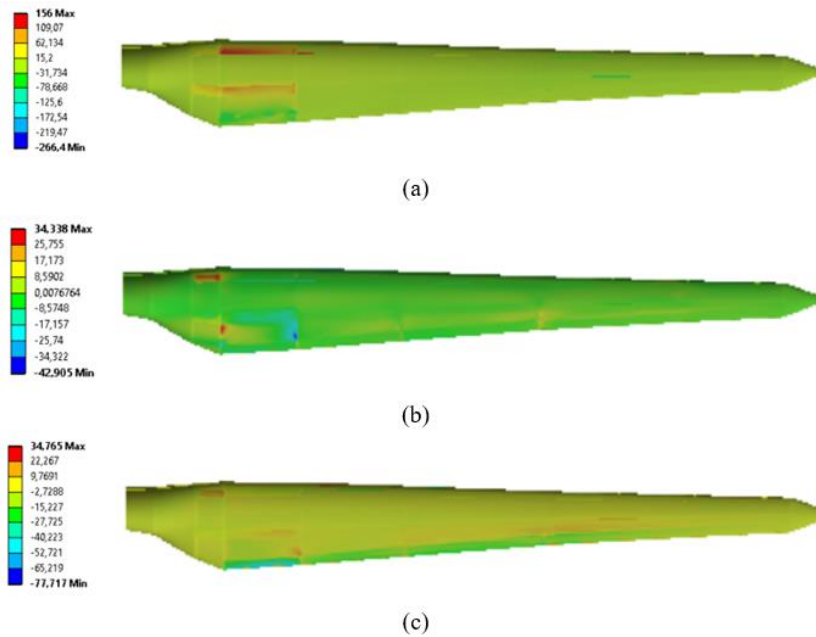


Figure 4.3. Stress distribution at the suction side of the blade (a) fiber directions (b) transverse fiber directions (c) shear stresses under flapwise loading.

4.5.2. Flapwise and Edgewise Analysis

In the flapwise and edgewise analysis, the blade root is fixed all six degree of freedom and flapwise and edgewise loads are given in Figure 3.16 are applied along the blade. Also, the gravity force is applied to the blade. The total deformation is almost 0.4 meters at the tip of the blade as given in Figure 4.4. In the flapwise analysis, the deflection in the edgewise direction is in the way of leading edge. In the flapwise and edgewise analysis, edgewise loads are applied to the blade in the trailing edge way. Therefore, there is nearly no deflection in the edgewise direction.

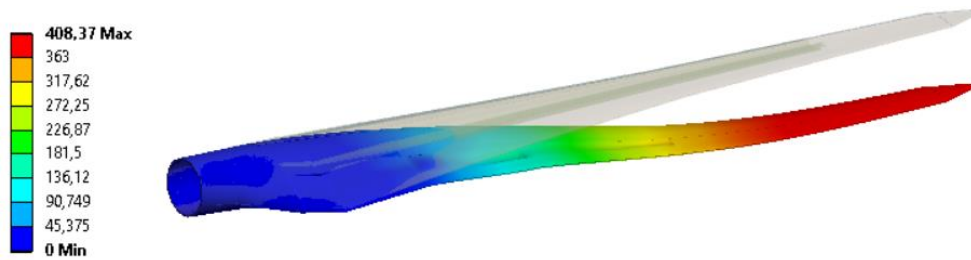


Figure 4.4. Total deformation under loading in flapwise and edgewise direction.

The stress distribution along blade is given in Figure 4.5.

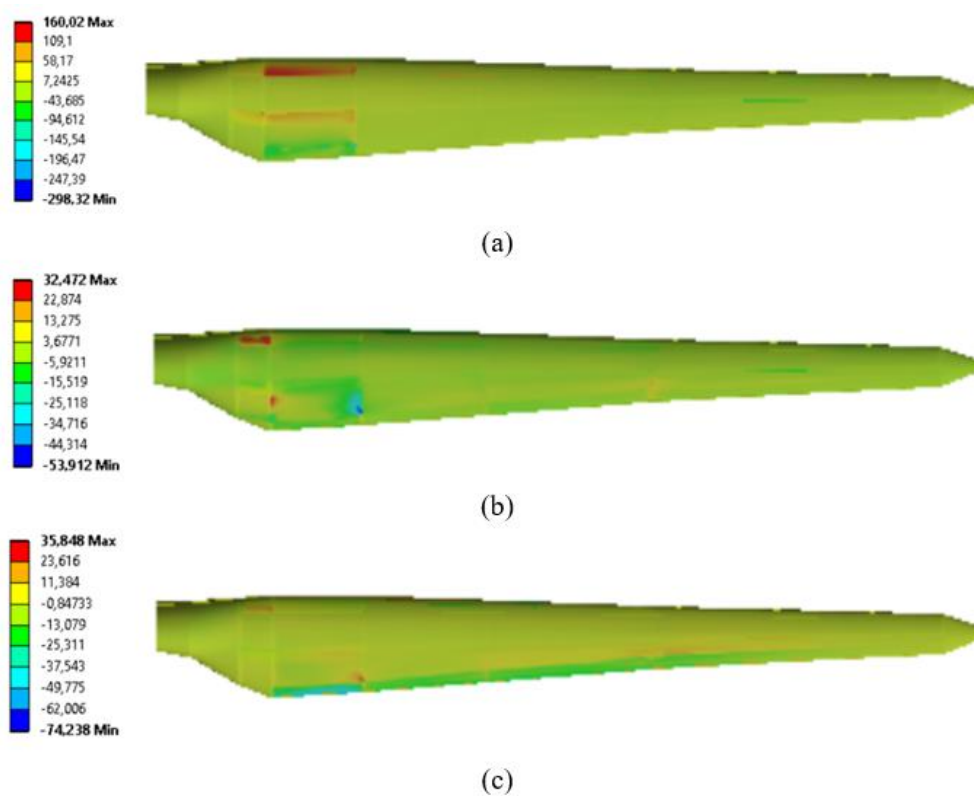


Figure 4.5. Stress distribution at the suction side of the blade (a) fiber directions (b) transverse fiber directions (c) shear stresses under flapwise and edgewise loading.

4.6. Failure Analysis

In this section, blade failure is analyzed using Tsai-Wu criteria and Puck criteria. In Section 4.3.1, Puck and Tsai-Wu Failure Criteria are explained briefly. In Section 4.3.2, blade failure is modelled using two different composite failure models: linear elastic analysis using Tsai-Wu criteria and Puck criteria under extreme flapwise loading conditions. In Section 4.3.3, each analysis is performed again under extreme loads in the flapwise and edgewise direction.

4.6.1. Methodology

4.6.1.1. Tsai-Wu Failure Criterion

Tsai-Wu failure criterion [19] is classified among fully interactive failure criteria expressed by the equation below:

$$\frac{\sigma_1^2}{X_t X_c} - \frac{\sigma_1 \sigma_2}{\sqrt{X_t X_c Y_t Y_c}} + \frac{\sigma_2^2}{Y_t Y_c} + \left(\frac{\sigma_6}{S}\right)^2 + \left(\frac{1}{X_t} - \frac{1}{X_c}\right)\sigma_1 + \left(\frac{1}{Y_t} - \frac{1}{Y_c}\right)\sigma_2 = 1 \quad (7)$$

In equation (7), if the value of equation exceeds one, failure of the ply occurs. It is not possible to determine failure modes with this criterion.

4.6.1.2. Puck Failure Criteria

Puck failure criteria is one of the most commonly used criteria for the assessment of composite laminate strength. In this study, Puck failure criteria are applied to unidirectional and tri-axial laminate composite materials. Puck's failure criteria are implemented for the evaluation of stress results. For fiber failure, Puck's criteria are as follows:

$$f_{E(F)}^T = \frac{\sigma_1}{X_T} = 1 \quad (8)$$

$$f_{E(F)}^C = \frac{\sigma_1}{X_C} = 1 \quad (9)$$

where $f_{E(FF)}^T$ and $f_{E(FF)}^c$ are stress exposures for fiber failure under tension and compression loading situations. σ_1 is the stress value in fiber direction, X_T and X_c are tensile and compressive strengths in fiber direction.

Puck's inter fiber failure criteria use the following equations:

$$f_{E(IFF)}^A = \sqrt{\left(\frac{\sigma_6}{S}\right)^2 + \left(1 - p_{\perp H}^{(+)} \frac{Y_T}{S}\right)^2 \left(\frac{\sigma_2}{Y_T}\right)^2} + p_{\perp H}^{(+)} \frac{\sigma_2}{S} = 1 \quad (10)$$

$$f_{E(IFF)}^B = \frac{1}{S} \left(\sqrt{(\sigma_6)^2 + (p_{\perp H}^{(-)} \sigma_2)^2} + p_{\perp H}^{(-)} \sigma_2 \right) = 1 \quad (11)$$

$$f_{E(IFF)}^C = \left[\left(\frac{\sigma_6}{2(1 + p_{\perp\perp}^{(-)})S} \right)^2 + \left(\frac{\sigma_2}{Y_C} \right)^2 \right] \frac{Y_C}{(-\sigma_2)} = 1 \quad (12)$$

In the equations above $p_{\perp H}^{(+)}$, $p_{\perp H}^{(-)}$ and $p_{\perp\perp}^{(-)}$ represent inclination parameters that control the shape of the failure envelope. σ_2 is the stress value in transverse fiber direction, Y_T and Y_c are the tensile and the compressive strengths in transverse fiber direction. Shear stress and shear strength are represented by σ_6 and S, respectively. If the value of failure exposure (f_E) exceeds 1, failure initiation occurs. As seen in Figure 4.6, Mode A is caused by tensile and shear stresses. Modes B occurs under compressive and shear stresses. Mode C is a dangerous failure in compressive shearing which may lead to ultimate failure.

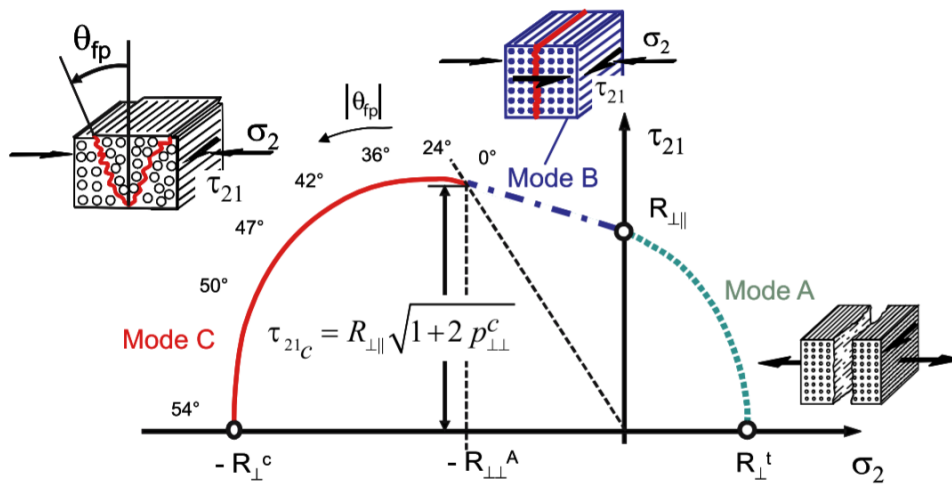


Figure 4.6. Puck fracture curve [20].

4.6.2. Failure Analysis Under Flapwise Loading

Since suction of part of the blade is heavily damaged under extreme flapwise loading, focus of investigation is the suction part. Figure 4.7 shows contour plots of Tsai-Wu failure inverse reserve factors in the suction side of the blade is presented for loads from 10% to 100% of the extreme flapwise loading with increments of 20%. Failure occurs if inverse reserve factor is greater than 1 and these failure areas are indicated in red. At 20% of loading, failure initiation begins at two main regions: interface between chassis-skin and part of the skin close to trailing edge. When 30% load level is reached, the failed region propagates along the interface between the chassis-skin, root and part of the skin close to trailing edge and leading edge. The blade failure areas occur nearly all suction side from root to the tip of the blade after %80 loading condition.

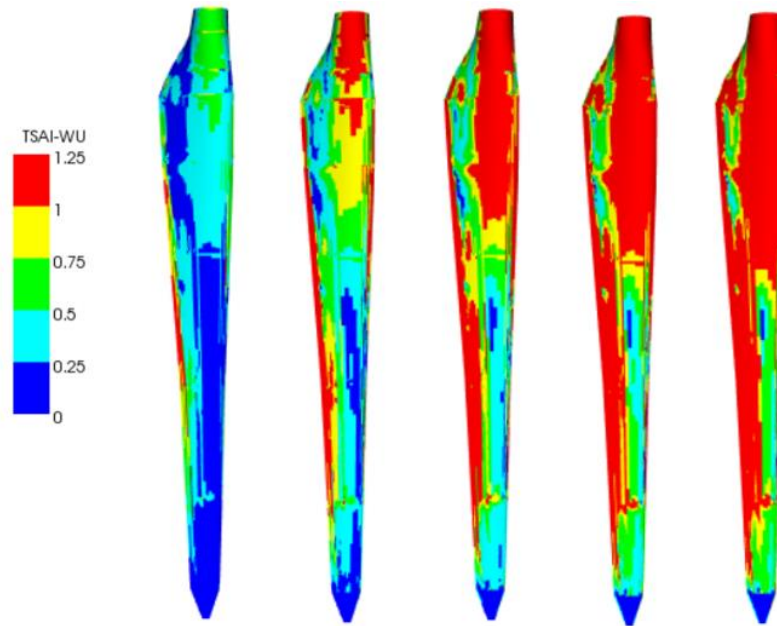


Figure 4.7. Contour plots of Tsai-Wu failure reserve factors under flapwise loads from 20% to 100% of the extreme flapwise loading.

Figure 4.8 shows contour plots of failure inverse reserve factors of IFF(A) mode in the suction side of the blade is presented for loads from 10% to 100% of the extreme flapwise loading with increments of 10%. In the suction side of the blade, failure exposures of IFF(A) mode initiate in the root and trailing edges of the blade at 20% and 30% of loading. As the loading is further increased to 40% and 50% at the root and trailing edge become larger. After 50% of extreme loading, the failure regions occur nearly all suction area of the blade.

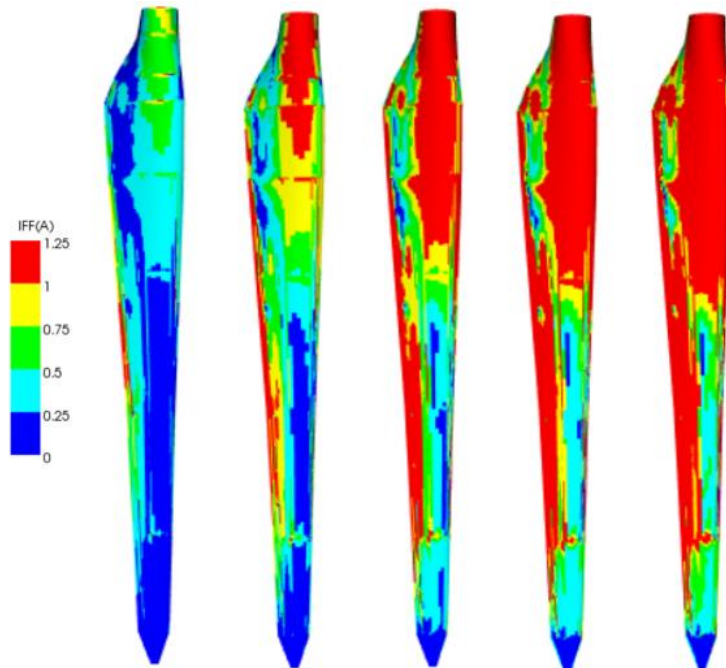


Figure 4.8. Contour plots of IFF (A) mode for the suction side of the blade under flapwise loads from 20% to 100% of the extreme flapwise loading.

Figure 4.9 shows contour plots of failure inverse reserve factors of IFF(B) mode in the suction side of the blade is presented for loads from 20% to 100% of the extreme flapwise loading with increments of 20%. In the suction side of the blade, failure exposures of IFF(B) mode is as similar as failure exposures of IFF(A). The difference is that failure exposures of IFF(B) mode initiate in the root and trailing edges of the blade at 40% of loading.

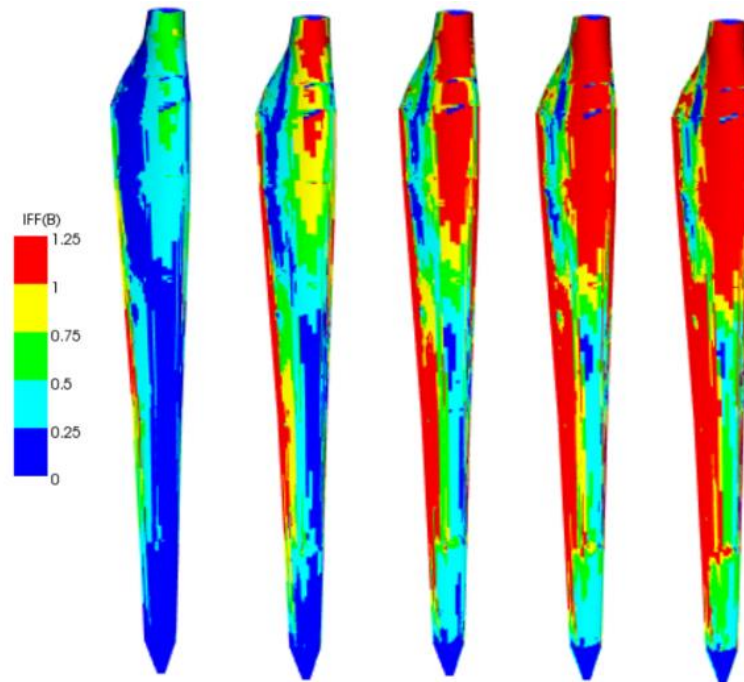


Figure 4.9. Contour plots of IFF (B) mode for the suction side of the blade under flapwise loads from 20% to 100% of the extreme flapwise loading.

When Puck failure criteria are considered, ultimate failure of the blade is considered to take place if fiber failure (FF) in any ply occurs or when inter fiber failure IFF (C) is observed. FF reduces the structural strength of the composite part drastically due to high energy release. In addition, risk of delamination is high when IFF (C) is seen in all plies [21]. Figure 4.10 and Figure 4.11 show contour plots of Puck failure exposures for IFF(C) and FF in suction side of the blade under static loading in flapwise direction, respectively. In the suction side of the blade, failure exposures of IFF(C) and FF modes initiate in the root and trailing edges of the blade at 50% of loading. As the loading is further increased to 40% and 50% at the root and trailing edge become larger. After 50% of extreme loading, the failure regions occur trailing edge at the suction side of the blade between 0.5-metre and 0.7-metre as seen in red areas.

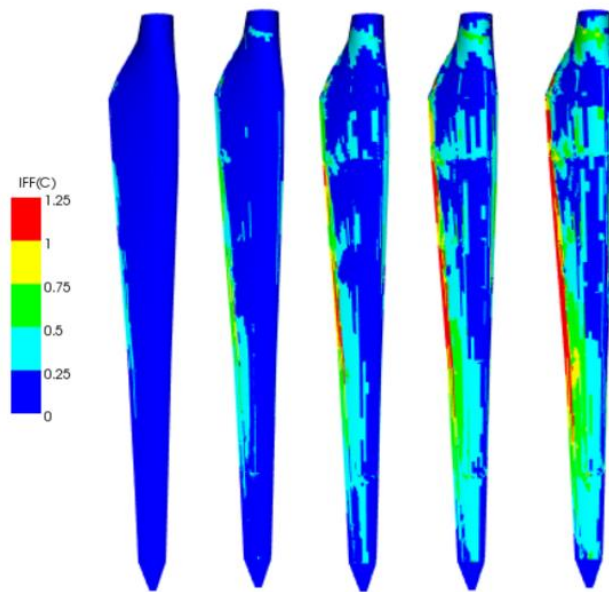


Figure 4.10. Contour plots of IFF (C) mode for the suction side of the blade under flapwise loads from 20% to 100% of the extreme flapwise loading.

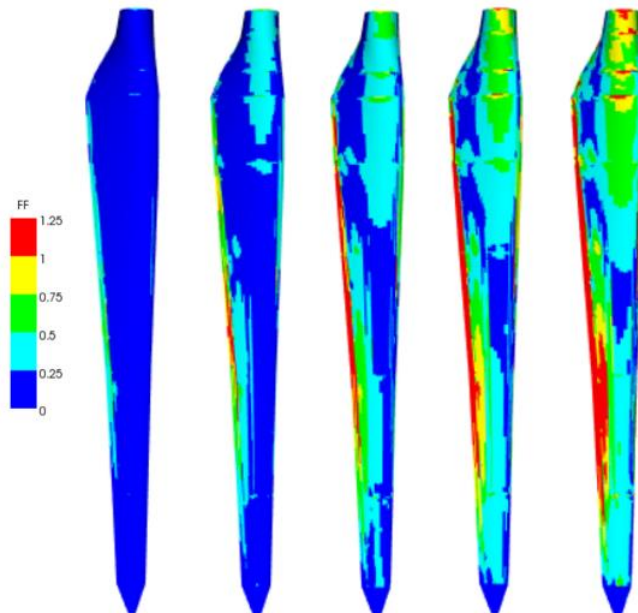


Figure 4.11. Contour plots of FF mode for the suction side of the blade under flapwise loads from 20% to 100% of the extreme flapwise loading.

Failure modes IFF(A) and IFF(B) are dominant over a larger area compared to FF and IFF(C). However, since IFF(A) and IFF(B) do not cause ultimate failure, these modes are not treated as critical as FF and IFF(C). The failure areas in FF and IFF(C) modes occur in trailing edge at the suction side of the blade from 0.5-metre to 0.7-metre from the root as seen in red areas at Ply 1 and Ply 9 which are 0° layers.

In pressure side of the blade, contour plots of Puck failure exposures for IFF(A), IFF(B), IFF(C) and FF under 100% static loading in flapwise direction are given in Figure 4.12, respectively. Failure modes IFF(A) is dominant in aeroshell, trailing edge and leading edge of the blade. However, the critical modes such as IFF(C) and FF are dominant in the root and leading edge of the blade.

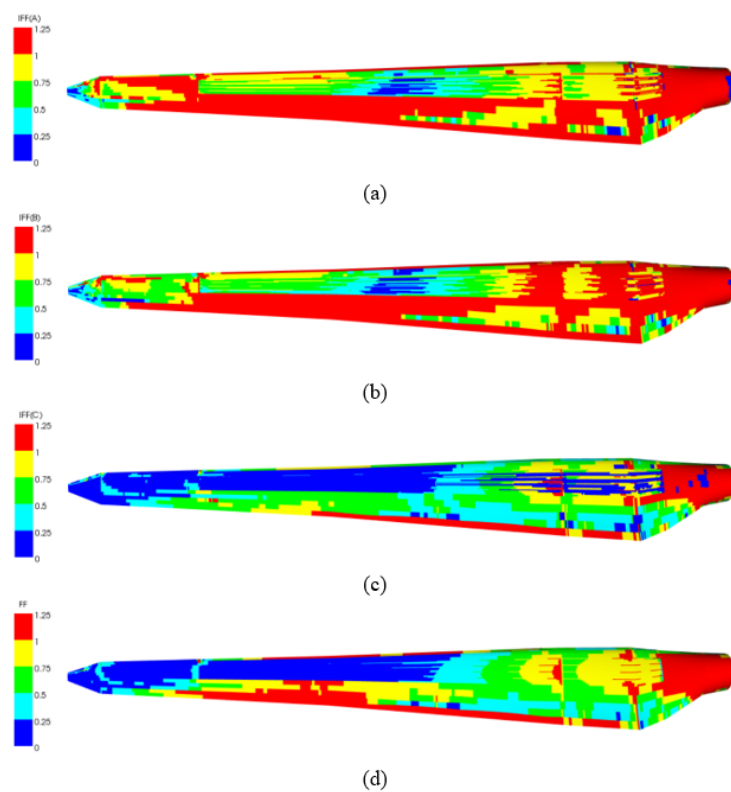


Figure 4.12. Contour plots of failure exposes of (a) IFF(A) (b) IFF(B) (c) IFF(C) (d) FF for the pressure side of the blade under flapwise loading.

Figure 4.13 shows contour plots of Tsai-Wu failure inverse reserve factor in the pressure side of the blade under extreme flapwise loading. Failed regions cover a larger area of the blade. The root, leading and trailing edges of the blades are failure regions. Since results which are obtained from linear elastic analysis using Tsai-Wu and Puck criteria are compared, Tsai-Wu failure criterion is used failed regions are seen to be larger compared to the case when Puck criteria are used.

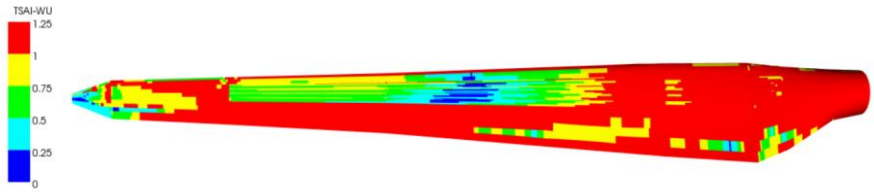


Figure 4.13. Contour plots of Tsai-Wu failure reserve factors in the pressure side at flapwise loading.

Figure 4.14 shows contour plots of Puck failure exposures for IFF(A), IFF(B), IFF(C) and FF in chassis of the blade under static loading in flapwise direction, respectively. Failure modes IFF(A) occurs the largest region of chassis. However, the critical modes such as IFF(C) and FF are not dominant in spar cap region. It can be concluded that the chassis is indestructible under extreme flapwise loading condition.

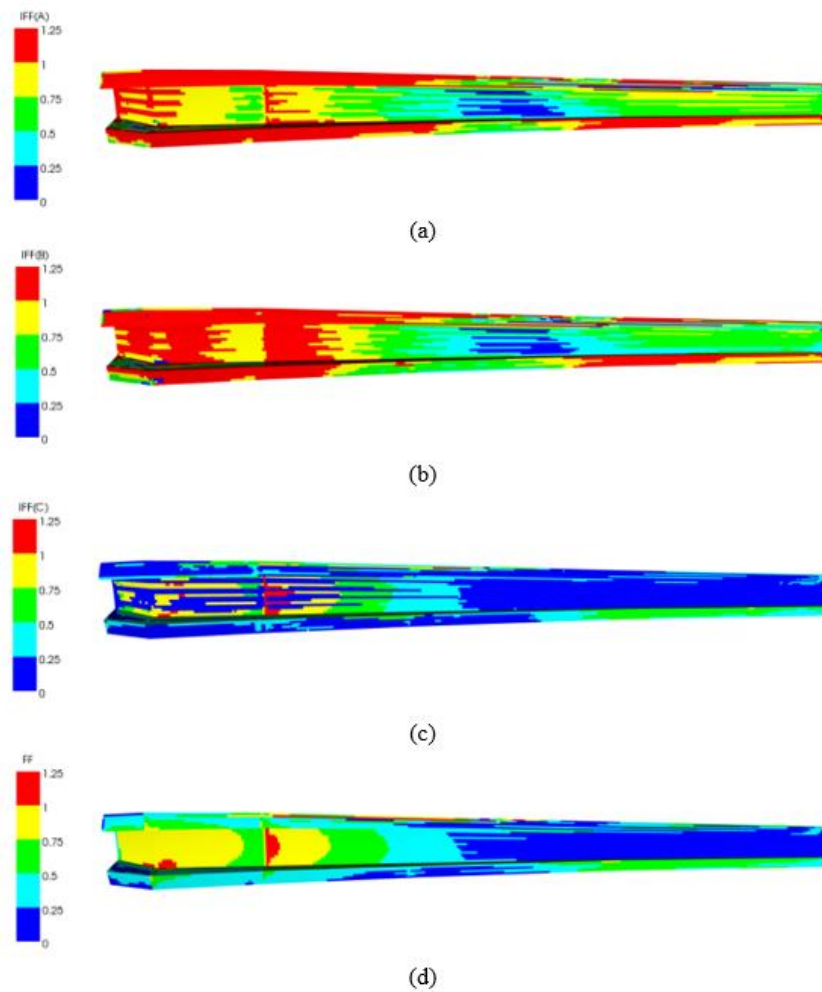


Figure 4.14. Contour plots of failure exposes of (a) IFF(A) (b) IFF(B) (c) IFF(C) (d) FF for the chassis of the blade under flapwise loading.

Figure 4.15 shows contour plots of Tsai-Wu failure inverse reserve factor in the chassis of the blade under extreme flapwise loading. Failed regions cover a larger area of the chassis although Puck failure criterion is used failed regions occur at spar caps particularly.

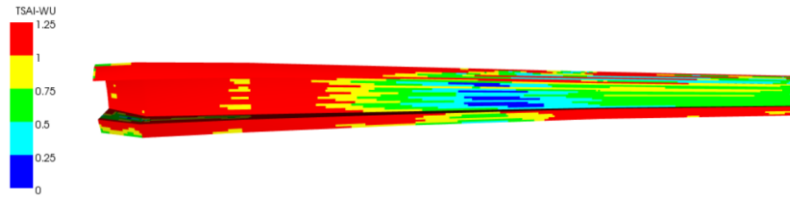


Figure 4.15. Contour plots of Tsai-Wu failure reserve factors in the chassis at flapwise loading.

Figure 4.16 shows contour plots of Puck failure exposures for IFF(A), IFF(B), IFF(C) and FF in internal flange of the blade under static loading in flapwise direction, respectively. Inverse reserve factor of all Puck failure exposures is above 1 in internal flange. Therefore, failure is occurred along internal flange for all Puck failure modes.

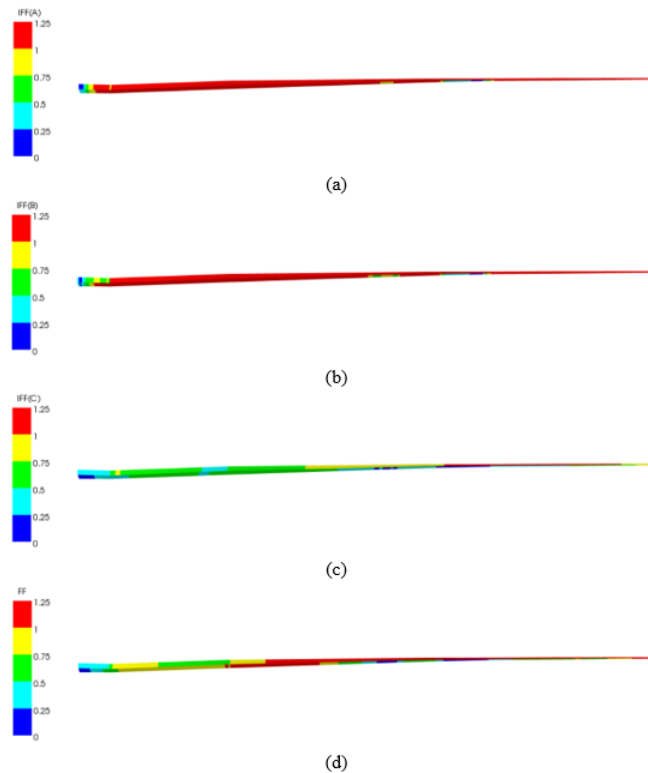


Figure 4.16. Contour plots of failure exposures of (a) IFF(A) (b) IFF(B) (c) IFF(C) (d) FF for the internal flange of the blade under flapwise loading.

Figure 4.17 shows contour plots of Tsai-Wu failure inverse reserve factor in the suction side of the blade under extreme flapwise loading. For both Puck and Tsai-Wu failure criteria, the inverse reserve factors are above 1. Hence, ultimate failure is expected to occur in the internal flange under the extreme flapwise loading case.



Figure 4.17. Contour plots of Tsai-Wu failure reserve factors in the internal flange at flapwise loading.

4.6.3. Failure Analysis Under Flapwise And Edgewise Loading

Since suction of part of the blade is heavily damaged under extreme flapwise and edgewise loading as given in Section 4.3, focus of investigation is the suction part. Figure 4.18 shows contour plots of Tsai-Wu failure inverse reserve factors in the suction side of the blade is presented for loads from 10% to 100% of the extreme flapwise and edgewise loading with increments of 10%. Failure occurs if inverse reserve factor is greater than 1 and these failure areas are indicated in red. At 20% load, failure initiation begins at two main regions: interface between chassis-skin and part of the skin close to trailing edge. When 30% load level is reached, the failed region propagates along the interface between the chassis-skin, root and part of the skin close to trailing edge and leading edge. The blade failure areas occur from root to the tip of the blade after %80 loading condition.

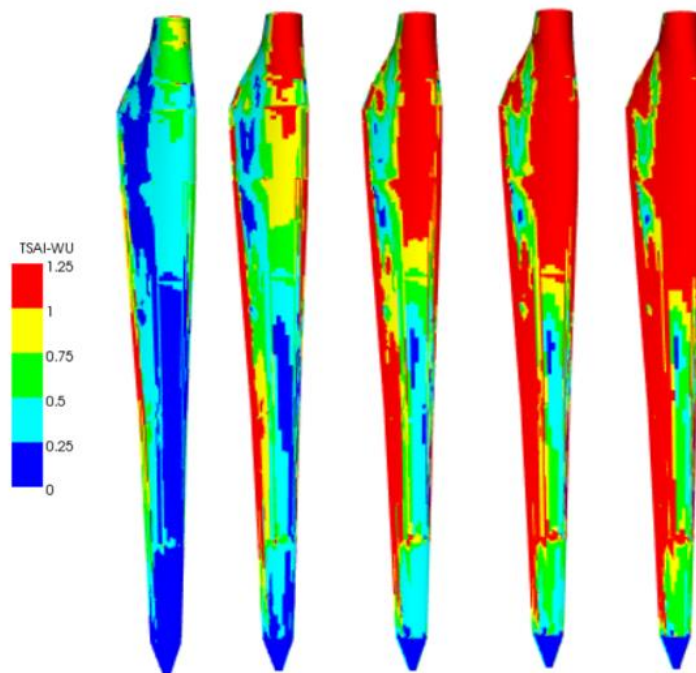


Figure 4.18. Contour plots of Tsai-Wu failure reserve factors of the blade under flapwise and edgewise loads from 20% to 100% of the extreme loading.

Figure 4.19 shows contour plots of failure inverse reserve factors of IFF(A) mode in the suction side of the blade is presented for loads from 10% to 100% of the extreme flapwise and edgewise loading with increments of 10%. In the suction side of the blade, failure exposures of IFF(A) mode initiate in the root and trailing edges of the blade at 20% and 30% of loading. As the loading is further increased to 40% and 50% at the root and trailing edge become larger. After 50% of extreme loading, the failure regions occur nearly all suction area of the blade.

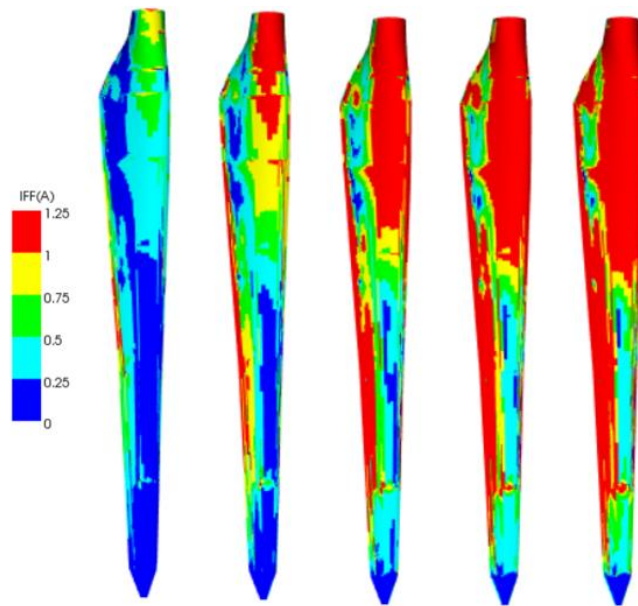


Figure 4.19. Contour plots of IFF (A) mode for the suction side of the blade under flapwise and edgewise loads from 10% to 100% of the extreme loading.

Figure 4.20 shows contour plots of failure inverse reserve factors of IFF(B) mode in the suction side of the blade is presented for loads from 10% to 100% of the extreme flapwise and edgewise loading with increments of 10%. In the suction side of the blade, failure exposures of IFF(B) mode is as similar as failure exposures of IFF(A). The only difference is that failure exposures of IFF(B) mode initiate in the root and trailing edges of the blade at 40% of loading.

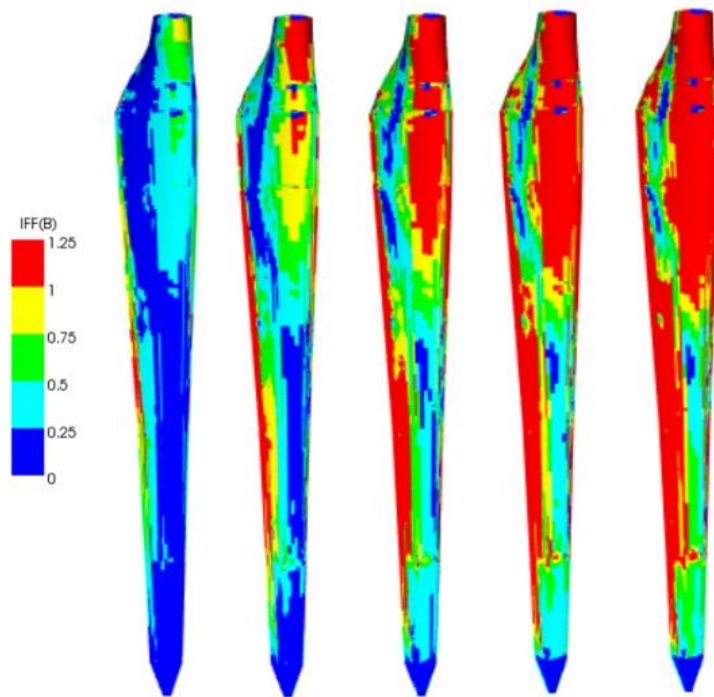


Figure 4.20. Contour plots of IFF (B) mode for the suction side of the blade under flapwise and edgewise loads from 20% to 100% of the extreme loading.

When Puck failure criteria are considered, ultimate failure of the blade is considered to take place if fiber failure (FF) in any ply occurs or when inter fiber failure IFF (C) is observed. FF reduces the structural strength of the composite part drastically due to high energy release. In addition, risk of delamination is high when IFF (C) is seen in all plies [21]. Figure 4.21 and Figure 4.22 show contour plots of Puck failure exposures for IFF(C) and FF in suction side of the blade under static loading in flapwise and edgewise direction, respectively. In the suction side of the blade, failure exposures of IFF(C) and FF modes initiate in the root and trailing edges of the blade at 50% of loading. As the loading is further increased to 40% and 50% at the root and trailing edge become larger. After 50% of extreme loading, the failure regions occur trailing edge at the suction side of the blade between 0.5-metre and 0.7-metre as seen in red areas.

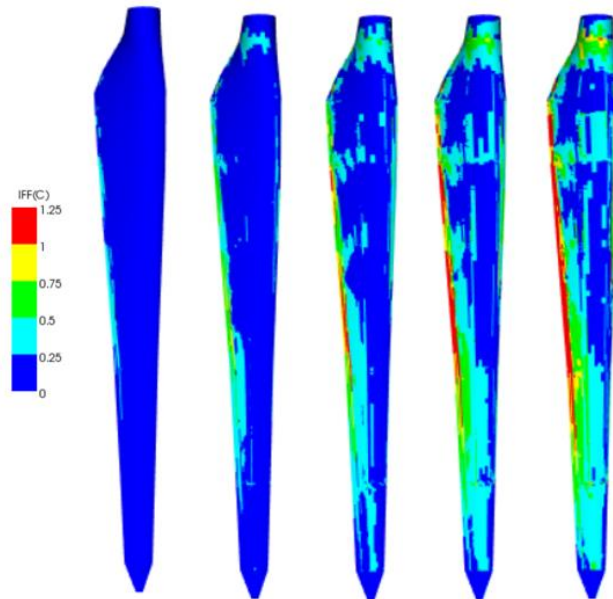


Figure 4.21. Contour plots of IFF (C) mode for the suction side of the blade under flapwise and edgewise loads from 20% to 100% of the extreme loading.

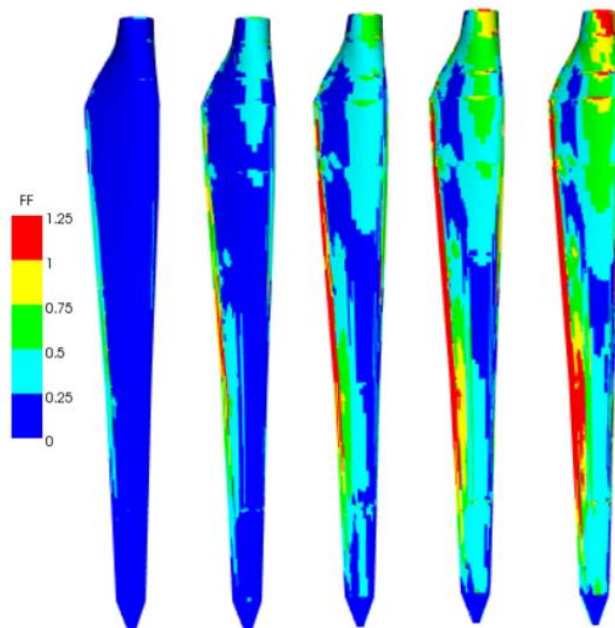


Figure 4.22. Contour plots of FF mode for the suction side of the blade under flapwise and edgewise loads from 20% to 100% of the extreme loading.

In pressure side of the blade, contour plots of Puck failure exposures for IFF(A), IFF(B), IFF(C) and FF under 100% static loading in flapwise and edgewise direction are given in Figure 4.23, respectively. Failure modes IFF(A) is dominant skin, trailing edge and leading edge of the blade. The critical modes such as IFF(C) and FF are dominant in the root and leading edge of the blade.

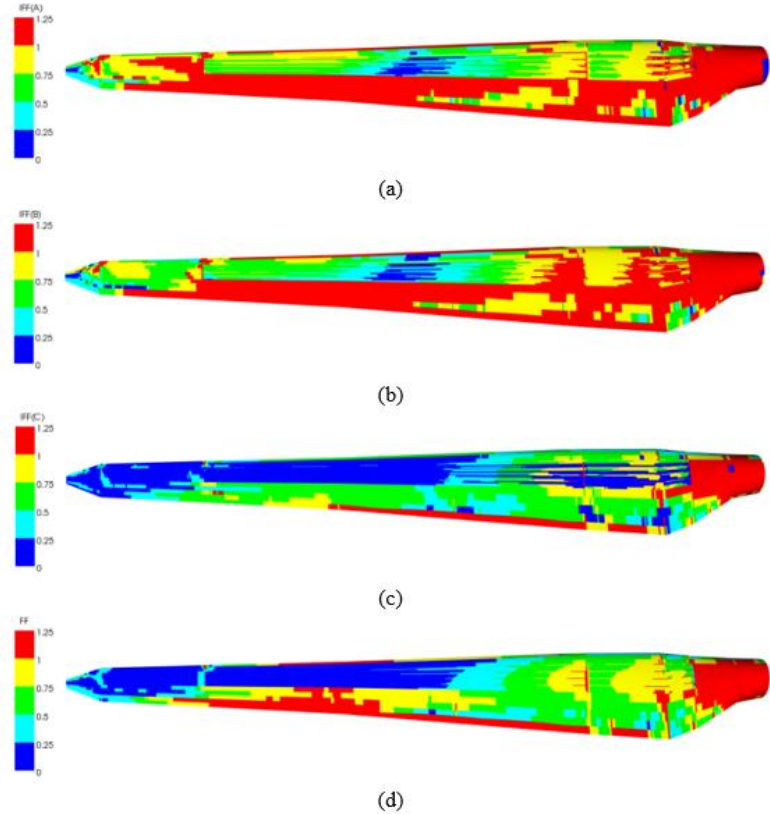


Figure 4.23. Contour plots of failure exposes of (a) IFF(A) (b) IFF(B) (c) IFF(C) (d) FF for the pressure side of the blade under flapwise and edgewise loading.

Figure 4.24 shows contour plots of Tsai-Wu failure inverse reserve factor in the pressure side of the blade under extreme flapwise and edgewise loading. The root, leading and training edges of the blades are failed area according to Tsai-Wu failure criteria. Nevertheless, failed regions are root and leading edges of the blade in the analysis using Puck failure criteria.

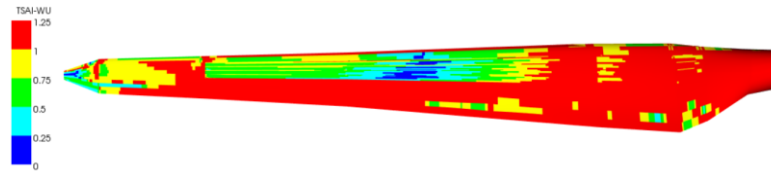


Figure 4.24. Contour plots of Tsai-Wu failure reserve factors in the pressure side at flapwise and edgewise loading.

Figure 4.25 shows contour plots of Puck failure exposures for IFF(A), IFF(B), IFF(C) and FF in chassis of the blade under static loading in flapwise and edgewise direction, respectively. Failure modes IFF(A) is occurred the largest region of chassis. Yet, the critical modes such as IFF(C) and FF are not excessive in the spar caps. It can be concluded that the chassis is indestructible under extreme flapwise and edgewise loading conditions according to failure analysis using Puck failure criteria.

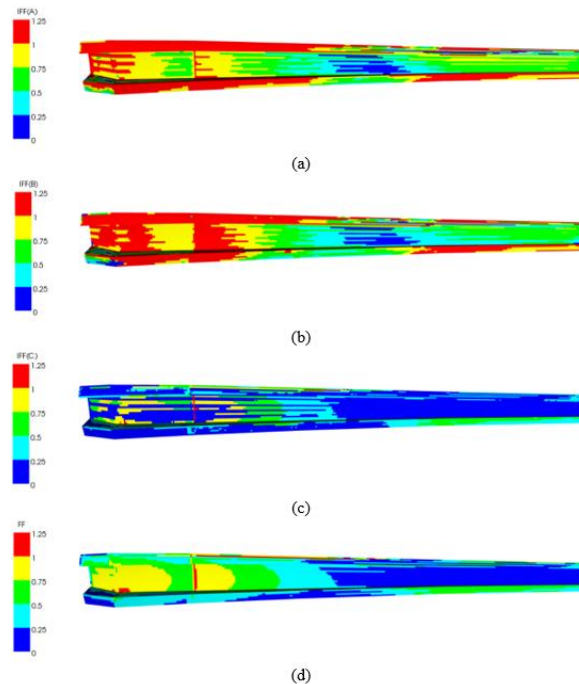


Figure 4.25. Contour plots of failure exposes of (a) IFF(A) (b) IFF(B) (c) IFF(C) (d) FF for the chassis of the blade under flapwise and edgewise loading.

Figure 4.26 shows contour plots of Tsai-Wu failure inverse reserve factor in the suction side of the blade under extreme flapwise and edgewise loading. Failed regions cover a larger area of the chassis although Puck failure criterion is used failed regions occur at spar caps particularly.

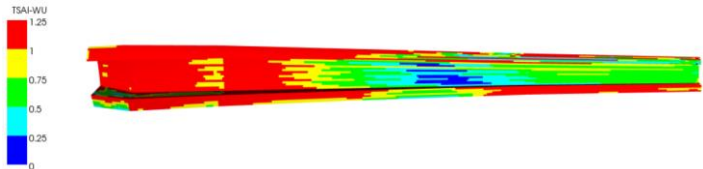


Figure 4.26. Contour plots of Tsai-Wu failure reserve factors in the chassis at flapwise and edgewise loading.

Figure 4.27 shows contour plots of Puck failure exposures for IFF(A), IFF(B), IFF(C) and FF in internal flange of the blade under static loading in flapwise and edgewise direction, respectively. The red areas are seen for all Puck failure exposures.

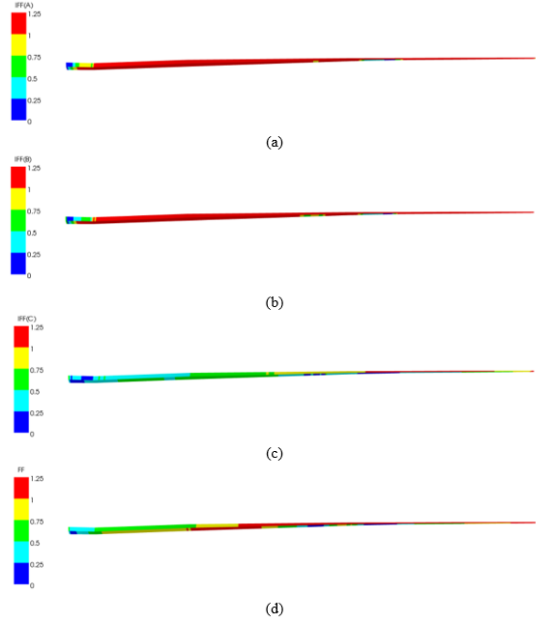


Figure 4.27. Contour plots of failure exposes of (a) IFF(A) (b) IFF(B) (c) IFF(C) (d) FF for the internal flange of the blade under flapwise and edgewise loading.

Figure 4.28 shows contour plots of Tsai-Wu failure inverse reserve factor in the suction side of the blade under extreme flapwise and edgewise loading. For Puck and Tsai-Wu failure criteria, it can be concluded that the internal flange is the weakest construction of the blade under extreme flapwise and edgewise loading.



Figure 4.28. Contour plots of Tsai-Wu failure reserve factors in the internal flange at flapwise and edgewise loading.

CHAPTER 6

STATIC AND FAILURE ANALYSIS OF THE UNBONDED BLADE

Typical failure modes observed as adhesive joint failure that is observed at the leading and trailing edges. In this chapter, this adhesive joint failure is investigated. In Section 6.1, the unbonded blade model is explained in detail. In Section 5.2., the natural frequencies and the mode shapes of the blade are estimated. In Section 5.3., the results for the static analysis are presented under two loading conditions: flapwise and edgewise loading. In Section 5.4., blade failure is modelled using two different composite failure models: linear elastic analysis using Tsai-Wu criteria and Puck criteria under extreme loading conditions.

5.1. Unbonded Blade Model

During its operation a wind turbine blade is exposed to large forces in both edgewise and flapwise directions. These forces cause stresses in skin, spar and adhesive joints of the blade [7]. Typical failure modes observed in a typical composite wind turbine blade are given in Figure 5.1. As seen from the figure, at the leading and trailing edges of the blade, adhesive joint failure is detected. These typical failure modes are examined by Sorensen et al. [22]. In Sorensen's paper, debonding between skin and adhesive, and delamination between laminates are observed between the layers of the aeroshell.

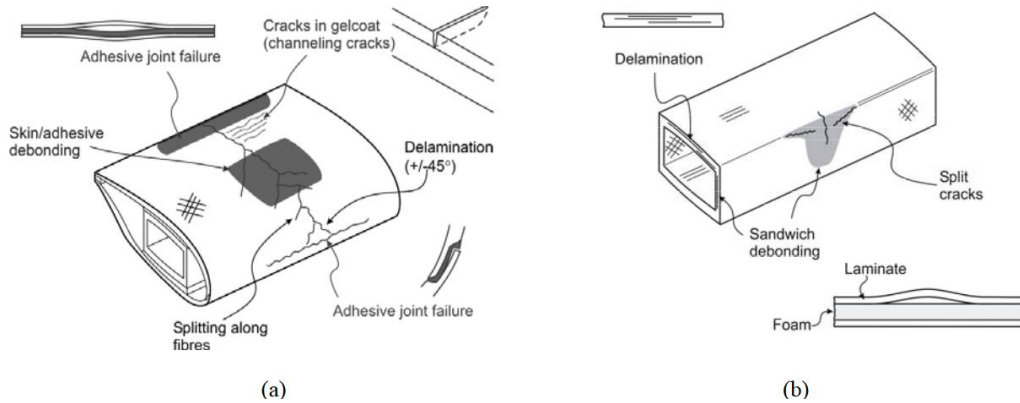


Figure 5.1. Failure modes occurred in (a) skin of the blade (b) spar of the blade [7].

In the same manner, In Chapter 4, strength analysis of the 5-meter RUGEM wind turbine blade shows that inverse reserve factors are particularly high at the leading, trailing edges and at the interface chassis-skin, where the expected failure initiation will begin. IFF(A, B and C) are expected to facilitate delamination at these locations. Thus, all analyzes are repeated subjected to unbonded blade model. The unbonded blade model is given in Figure 5.2. By taking the failure mode exposure areas into account, the unbonded region selected. From 0.7 to 1.25 meters between trailing edges of suction and pressure sides, it is assumed that no adhesive is applied to the finite element model of the blade.

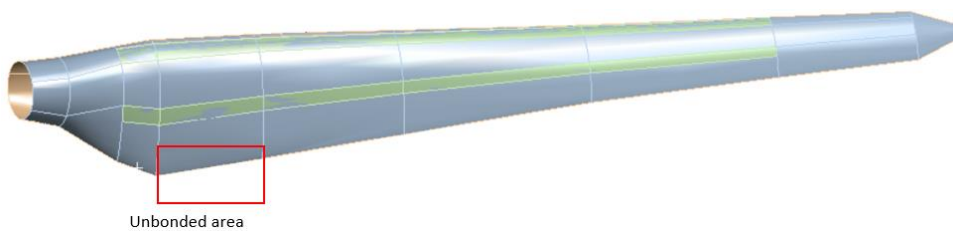


Figure 5.2. Unbonded blade model.

Except no adhesive edges, finite element analysis is performed under same boundary conditions as mentioned in Chapter 3. Mesh size and loading conditions are same as the fully-bonded blade model.

5.2. Modal Analysis

To estimate the mode shapes and natural frequencies of the unbonded blade, a modal analysis is performed in ANSYS Workbench. In the modal analysis, the blade is fixed at the root by fixing all degree of freedom. Table 4 presents the results of the modal analysis that calculated the natural frequencies of the unbonded blade for bending modes in the edgewise and flapwise directions. The mode shapes of the blade are given in Figure 5.3. The maximum natural frequency occurs in the torsional movement of the blade. So, this mode shape must be taken into account when the wind turbine will be designed.

Table 4. Results of modal analysis of the unbonded blade.

Mode Shapes		Natural Frequencies [Hz]
1 st Mode Shape	1 st Flapwise Bending	5.4
2 nd Mode Shape	2 nd Flapwise Bending	9.3
3 rd Mode Shape	3 rd Flapwise Bending	20.4
4 th Mode Shape	4 th Flapwise Bending & 1 st Edgewise Bending Coupling	33.8
5 th Mode Shape	5 th Flapwise Bending & 2 nd Edgewise Bending Coupling	35.3
6 th Mode Shape	3 rd Flapwise Bending & 1 st Torsion Coupling	41.7

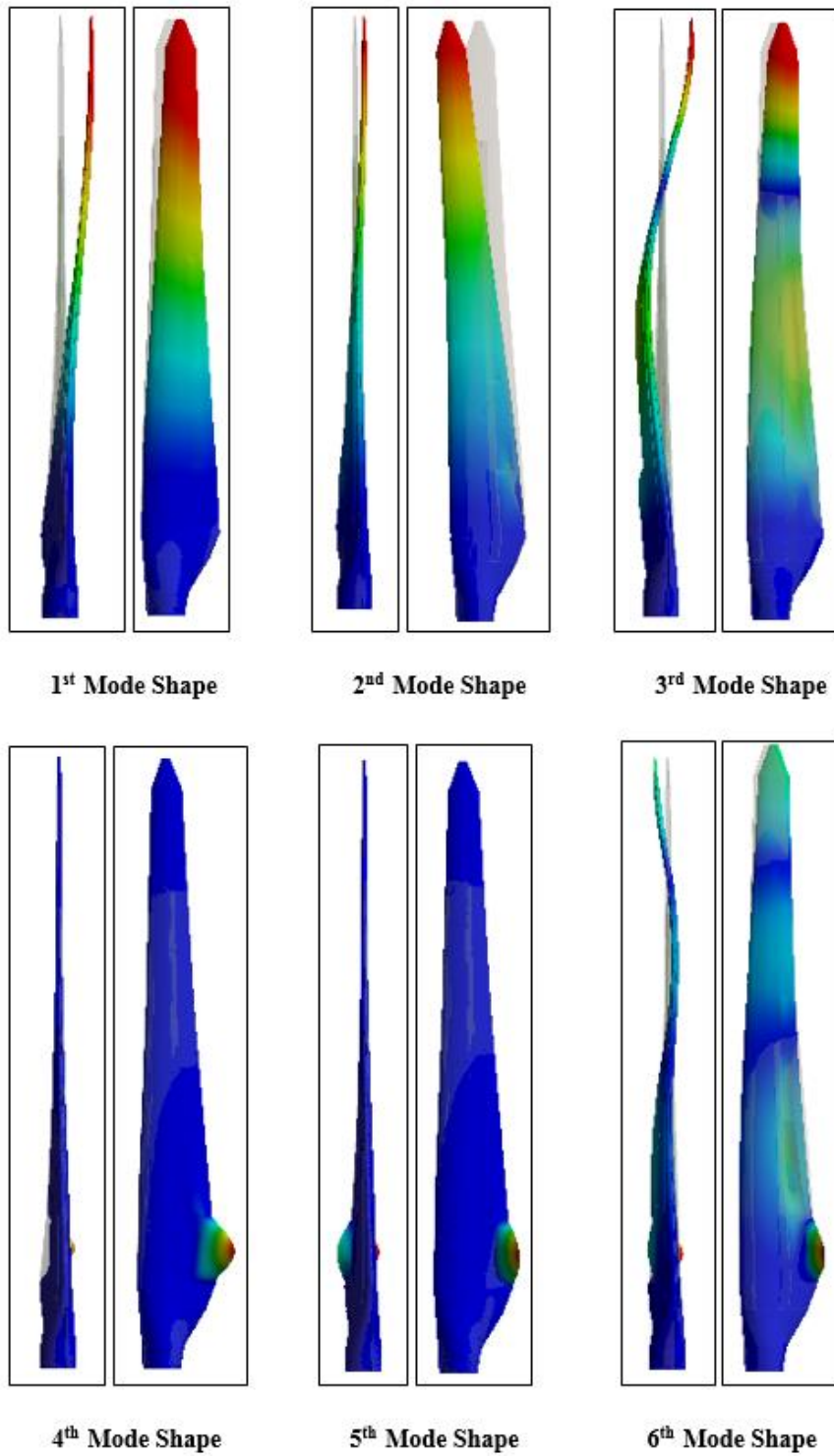


Figure 5.3. Mode shapes of the unbonded blade.

5.3. Static Analysis

The results for the static analysis under flapwise and flapwise and edgewise loading conditions are presented in Section 5.3.1 and Section 5.3.2. The detailed investigation about static analysis is given in Chapter 6.

5.3.1. Flapwise Analysis

In the flapwise analysis, the blade root is fixed all six degree of freedom and flapwise loads are given in Figure 3.16 are applied along the blade. The total deformation is almost 0.4-meter in the flapwise direction at the tip of the blade as given in Figure 5.4. In the edgewise direction, there is a small deflection because of the twist angle of the blade.

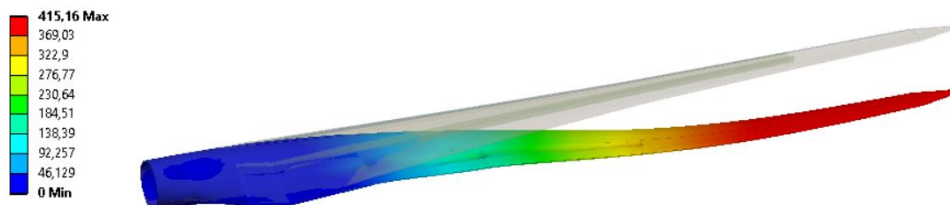


Figure 5.4. Total deformation of unbonded blade under loading in flapwise direction.

The deformation of unbonded region is given in Figure 5.5. The trailing edge between suction and pressure sides is deformed separately due to lack of adhesive.

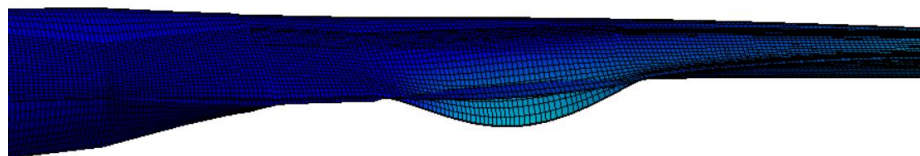


Figure 5.5. Deformation of the unbonded region of the blade.

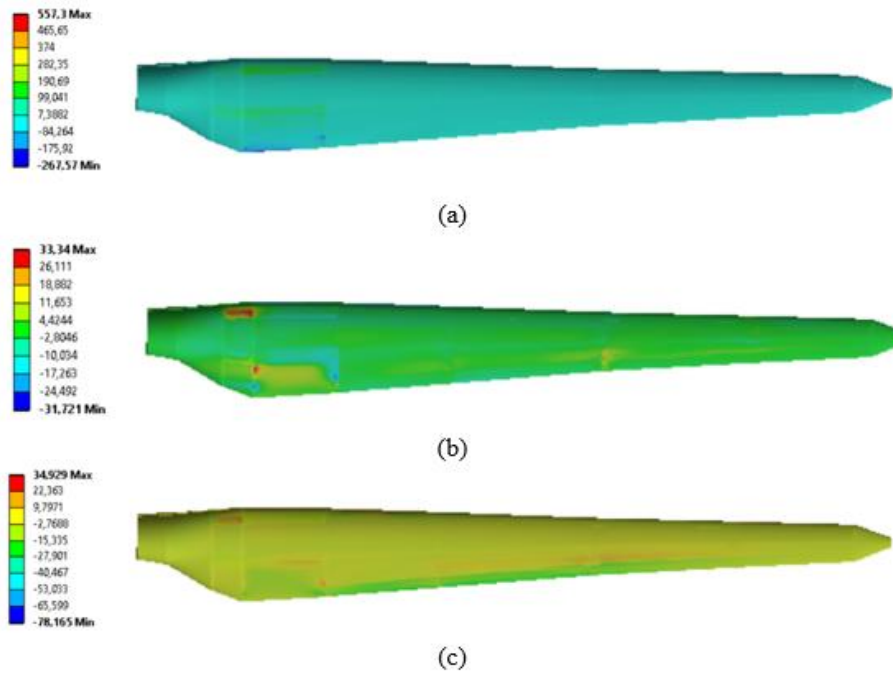


Figure 5.6. Stress distribution at the suction side of the blade (a) fiber directions (b) transverse fiber directions (c) shear stresses under flapwise loading.

5.3.2. Flapwise and Edgewise Analysis

In the flapwise and edgewise analysis, the blade root is fixed all six degree of freedom and flapwise and edgewise loads are given in Figure 3.16 are applied along the blade. Also, the gravity force is applied to the blade. The total deformation is almost 0.4 meters at the tip of the blade as given in Figure 5.7. In the flapwise analysis, the deflection in the edgewise direction is in the way of leading edge. In the flapwise and edgewise analysis, edgewise loads are applied to the blade in the trailing edge way. Therefore, there is nearly no deflection in the edgewise direction.

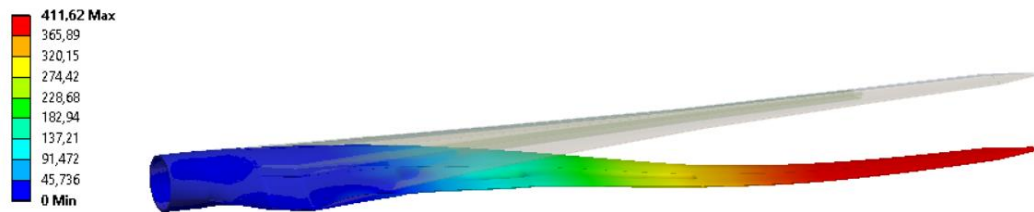


Figure 5.7. Total deformation of unbonded blade under loading in flapwise and edgewise direction.

The stress distribution along blade is given in Figure 5.8.

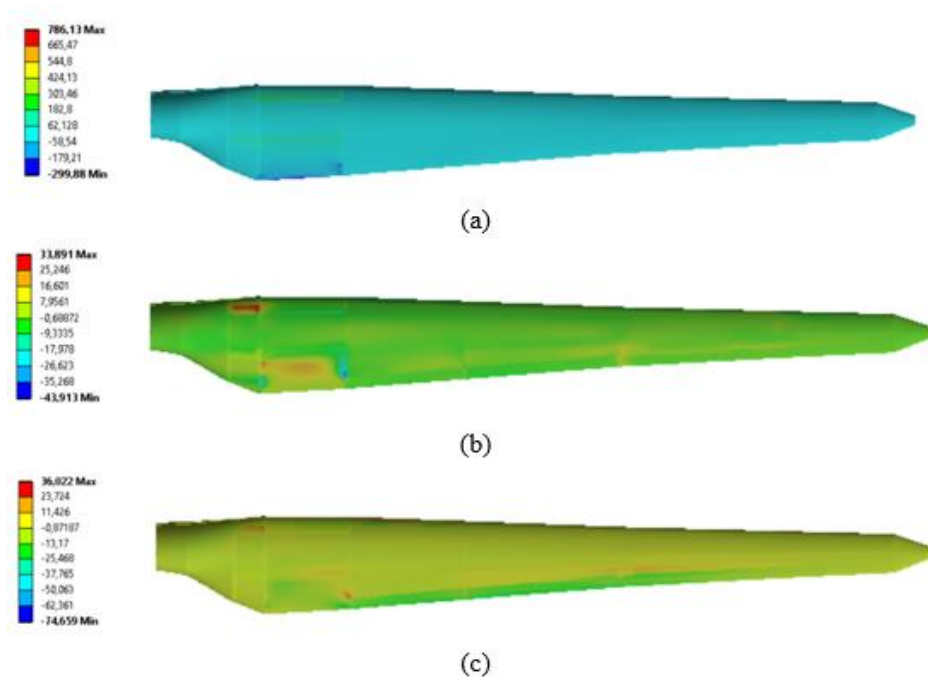


Figure 5.8. Stress distribution at the suction side of the blade (a) fiber directions (b) transverse fiber directions (c) shear stresses under flapwise and edgewise loading.

5.4. Failure Analysis

In this section, the unbonded blade failure is analyzed using Tsai-Wu criteria and Puck criteria. The unbonded blade failure is modelled using two different composite failure

models: linear elastic analysis using Tsai-Wu criteria and Puck criteria. In Section 6.4.1, the results of the failure analysis under flapwise loading condition are given. In Section 6.4.2, the results of the failure analysis under flapwise and edgewise loading condition are given.

5.4.1. Failure Analysis Under Flapwise Loading

Since suction of part of the blade is heavily damaged under extreme flapwise loading, focus of investigation is the suction side of the blade. Figure 5.9 shows contour plots of Tsai-Wu failure inverse reserve factors in the suction side of the blade is presented for loads from 10% to 100% of the extreme flapwise loading with increments of 10%. Failure occurs if inverse reserve factor is greater than 1 and these failure areas are indicated in red. At 20% load, failure initiation begins at two main regions: interface between chassis-skin and part of the skin close to trailing edge. When 30% load level is reached, the failed region propagates along the interface between the chassis-skin, root and part of the skin close to trailing edge and leading edge. The blade failure areas under the higher loading (higher than %80 loading) occur from root to the tip of the blade.

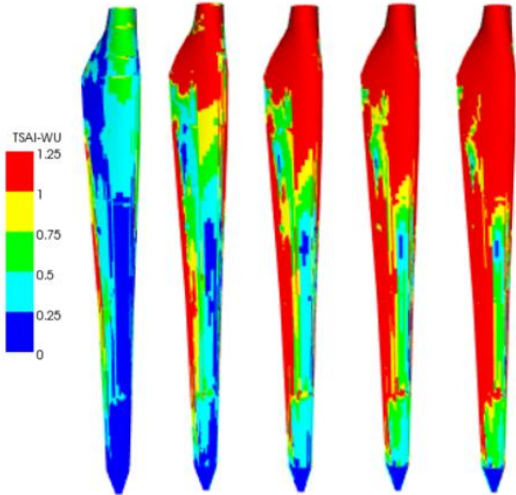


Figure 5.9. Contour plots of Tsai-Wu failure reserve factors under flapwise loads from 10% to 100% of the extreme loading.

Figure 5.10 shows contour plots of failure inverse reserve factors of IFF(A) mode in the suction side of the blade is presented for loads from 10% to 100% of the extreme flapwise loading with increments of 10%. In the suction side of the blade, failure exposures of IFF(A) mode initiate in the root and trailing edges of the blade at 20% and 30% of loading. As the loading is further increased to 40% and 50% at the root and trailing edge become larger. After 50% of extreme loading, the failure regions occur nearly all suction area of the blade.

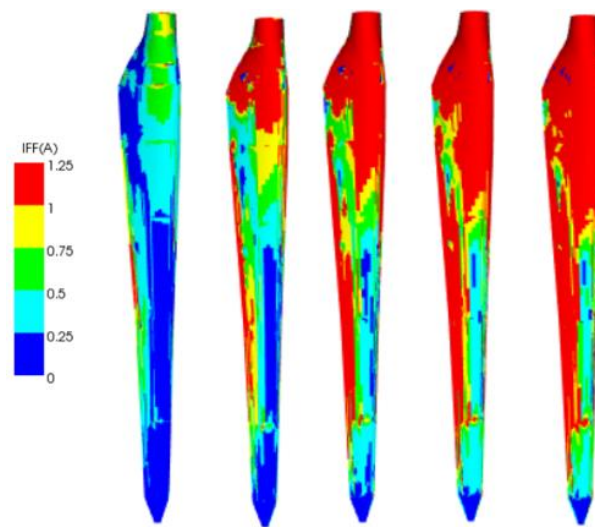


Figure 5.10. Contour plots of IFF (A) mode for the suction side of the blade under flapwise loads from 10% to 100% of the extreme loading.

Figure 5.11 shows contour plots of failure inverse reserve factors of IFF(B) mode in the suction side of the blade is presented for loads from 10% to 100% of the extreme flapwise loading with increments of 10%. In the suction side of the blade, failure exposures of IFF(B) mode is as similar as failure exposures of IFF(A). The only difference is that failure exposures of IFF(B) mode initiate in the root and trailing edges of the blade at 40% of loading.

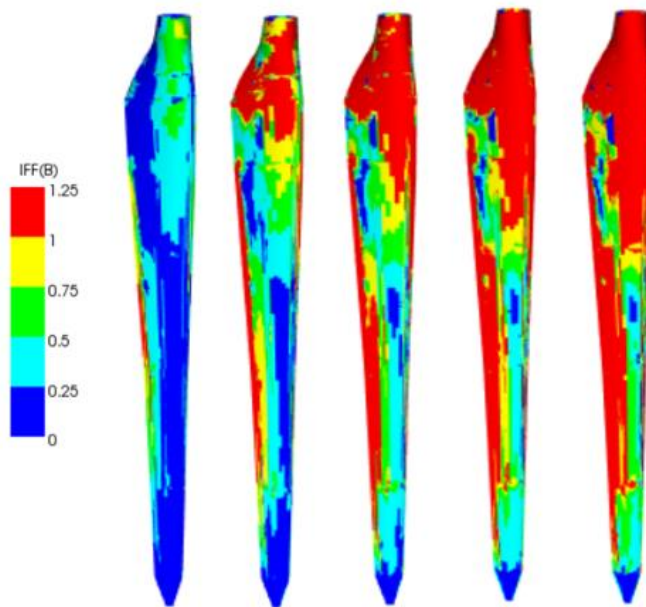


Figure 5.11. Contour plots of IFF (B) mode for the suction side of the blade under flapwise loads from 20% to 100% of the extreme loading.

When Puck failure criteria are considered, ultimate failure of the blade is considered to take place if fiber failure (FF) in any ply occurs or when inter fiber failure IFF (C) is observed. FF reduces the structural strength of the composite part drastically due to high energy release. In addition, risk of delamination is high when IFF (C) is seen in all plies. Figure 5.12 and Figure 5.13 show contour plots of Puck failure exposures for IFF(C) and FF in suction side of the blade under static loading in flapwise direction, respectively. In the suction side of the blade, failure exposures of IFF(C) and FF modes initiate in the root and trailing edges of the blade at 50% of loading. As the loading is further increased to 40% and 50% at the root and trailing edge become larger. After 50% of extreme loading, the failure regions occur trailing edge at the suction side of the blade between 0.5-metre and 0.7-metre as seen in red areas.

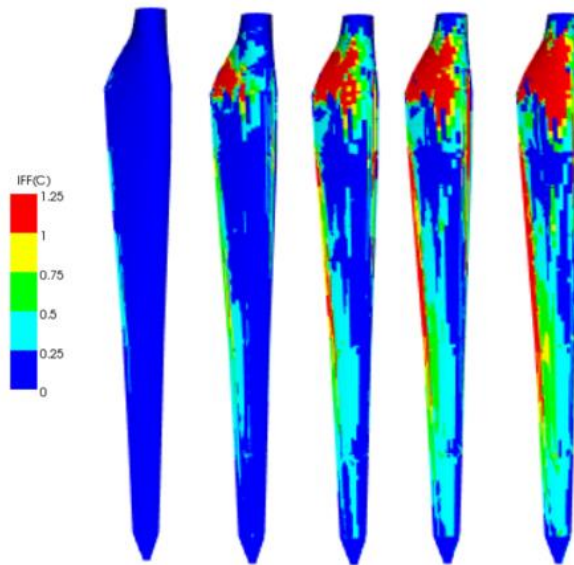


Figure 5.12. Contour plots of IFF (C) mode for the suction side of the blade under flapwise loads from 10% to 100% of the extreme loading.

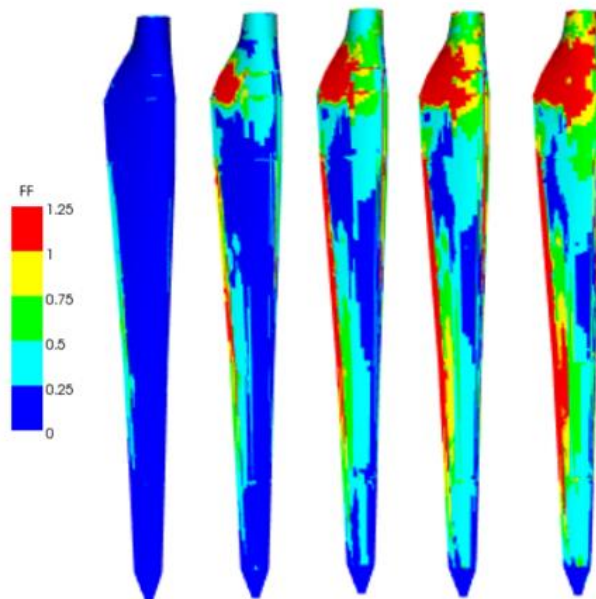


Figure 5.13. Contour plots of FF mode for the suction side of the blade under flapwise loads from 10% to 100% of the extreme loading.

Failure modes IFF(A) and IFF(B) are dominant over a larger area compared to FF and IFF(C). However, since IFF(A) and IFF(B) do not cause ultimate failure, these modes are not treated as critical as FF and IFF(C). The failure areas in FF and IFF(C) modes occur in trailing edge at the suction side of the blade between 0.5-metre and 0.7-metre as seen in red areas at Ply 1 and Ply 9 which are 0° layers.

In pressure side of the blade, contour plots of Puck failure exposures for IFF(A), IFF(B), IFF(C) and FF under 100% static loading in flapwise direction are given in Figure 5.14, respectively. Failure modes IFF(A) is dominant skin, trailing edge and leading edge of the blade. The critical modes such as IFF(C) and FF are dominant in the root and leading edge of the blade.

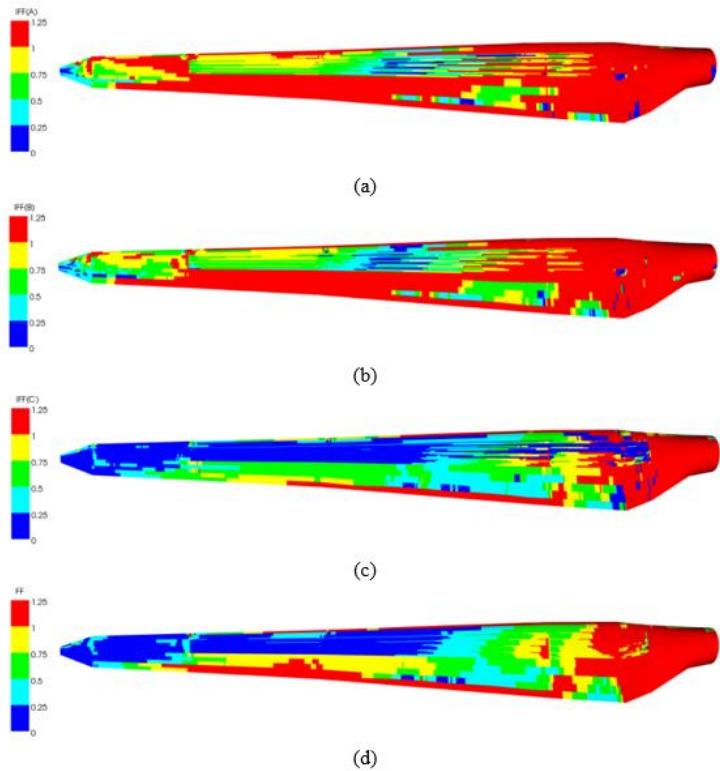


Figure 5.14. Contour plots of failure exposes of (a) IFF(A) (b) IFF(B) (c) IFF(C) (d) FF for the pressure side of the unbonded blade under flapwise loads.

Figure 5.15 shows contour plots of Tsai-Wu failure inverse reserve factor in the pressure side of the blade under extreme flapwise loading. Failed regions cover a larger area of the blade. The root, leading and trailing edges of the blades are failure regions. Since results which are obtained from linear elastic analysis using Tsai-Wu and Puck criteria are compared, Tsai-Wu failure criterion is used failed regions are seen to be larger compared to the case when Puck criteria are used.

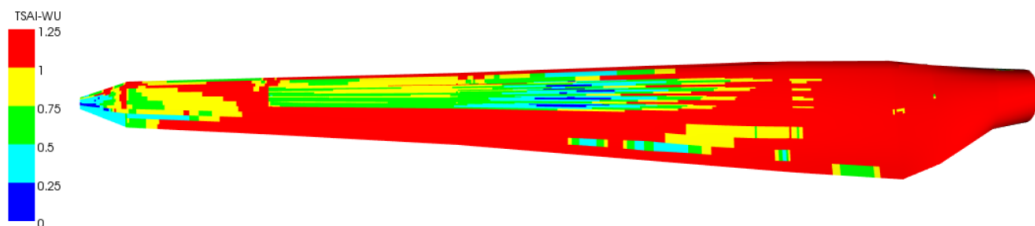


Figure 5.15. Contour plots of Tsai-Wu failure reserve factors in the pressure side at flapwise loading.

Figure 5.16 shows contour plots of Puck failure exposures for IFF(A), IFF(B), IFF(C) and FF in chassis of the blade under static loading in flapwise direction, respectively. Failure modes IFF(A) is occurred the largest region of chassis. However, the critical modes such as IFF(C) and FF are dominant in spar cap region.

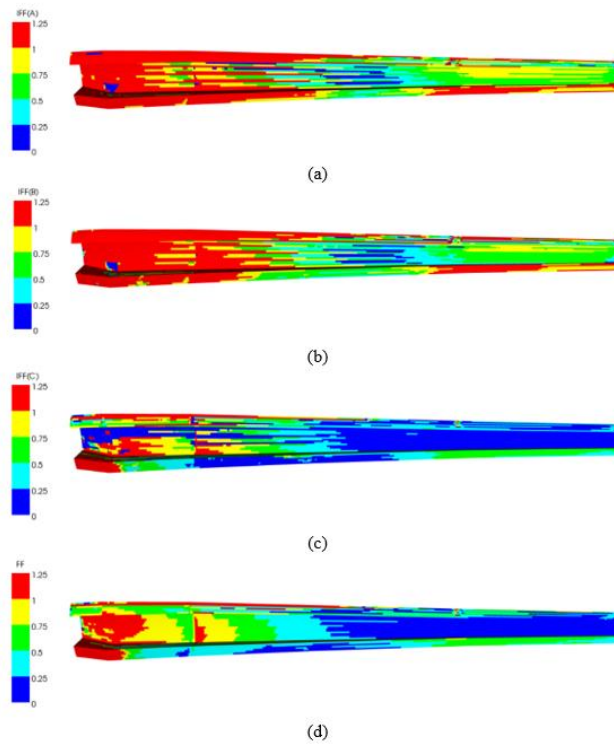


Figure 5.16. Contour plots of failure exposes of (a) IFF(A) (b) IFF(B) (c) IFF(C) (d) FF for the chassis of the unbonded blade under flapwise loads.

Figure 5.17 shows contour plots of Tsai-Wu failure inverse reserve factor in the chassis of the blade under extreme flapwise loading. Failed regions cover a larger area of the chassis although Puck failure criterion is used failed regions occur at spar caps particularly.

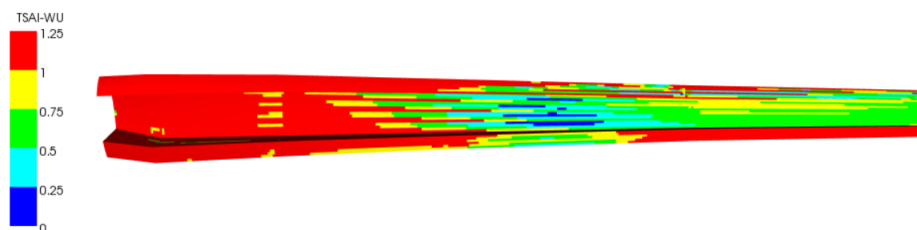


Figure 5.17. Contour plots of Tsai-Wu failure reserve factors in the pressure side at flapwise loading.

Figure 5.18 shows contour plots of Puck failure exposures for IFF(A), IFF(B), IFF(C) and FF in internal flange of the blade under static loading in flapwise direction, respectively. Inverse reserve factor of all Puck failure exposures is above 1 in internal flange. Therefore, failure is occurred along internal flange for all Puck failure modes.

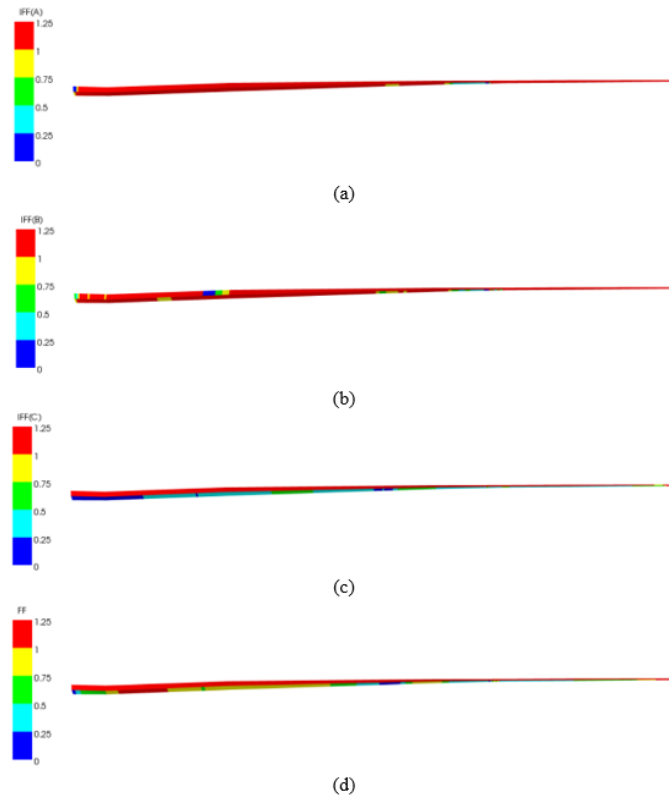


Figure 5.18. Contour plots of failure exposes of (a) IFF(A) (b) IFF(B) (c) IFF(C) (d) FF for the internal flange of the unbonded blade under flapwise loads.

Figure 5.19 shows contour plots of Tsai-Wu failure inverse reserve factor in the suction side of the blade under extreme flapwise loading. For both Puck and Tsai-Wu failure criteria, the inverse reserve factors are above 1. Hence, ultimate failure is expected to occur in the internal flange under the extreme flapwise loading case.



Figure 5.19. Contour plots of Tsai-Wu failure reserve factors in the internal flange at flapwise loading.

5.4.2. Failure Analysis Under Flapwise And Edgewise Loading

Since suction of part of the blade is heavily damaged under extreme flapwise and edgewise loading, focus of investigation is the suction part. Figure 5.20 shows contour plots of Tsai-Wu failure inverse reserve factors in the suction side of the blade is presented for loads from 10% to 100% of the extreme flapwise loading with increments of 10%. Failure occurs if inverse reserve factor is greater than 1 and these failure areas are indicated in red. At 20% load, failure initiation begins at two main regions: interface between chassis-skin and part of the skin close to trailing edge. When 30% load level is reached, the failed region propagates along the interface between the chassis-skin, root and part of the skin close to trailing edge and leading edge. The blade failure areas occur from root to the tip of the blade after %80 loading condition.

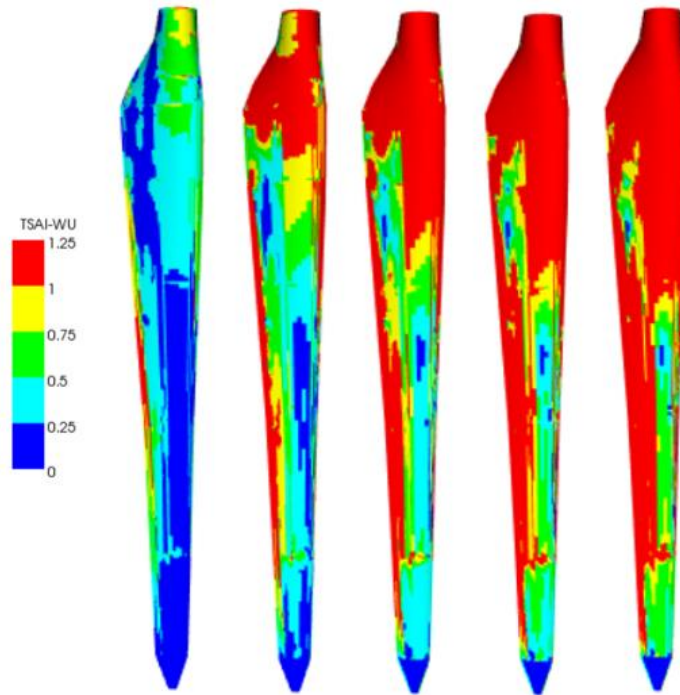


Figure 5.20. Contour plots of Tsai-Wu failure reserve factors under flapwise and edgewise loads from 20% to 100% of the extreme loading.

Figure 5.21 shows contour plots of failure inverse reserve factors of IFF(A) mode in the suction side of the blade is presented for loads from 10% to 100% of the extreme flapwise loading with increments of 10%. In the suction side of the blade, failure exposures of IFF(A) mode initiate in the root and trailing edges of the blade at 20% and 30% of loading. As the loading is further increased to 40% and 50% at the root and trailing edge become larger. After 50% of extreme loading, the failure regions occur nearly all suction area of the blade.

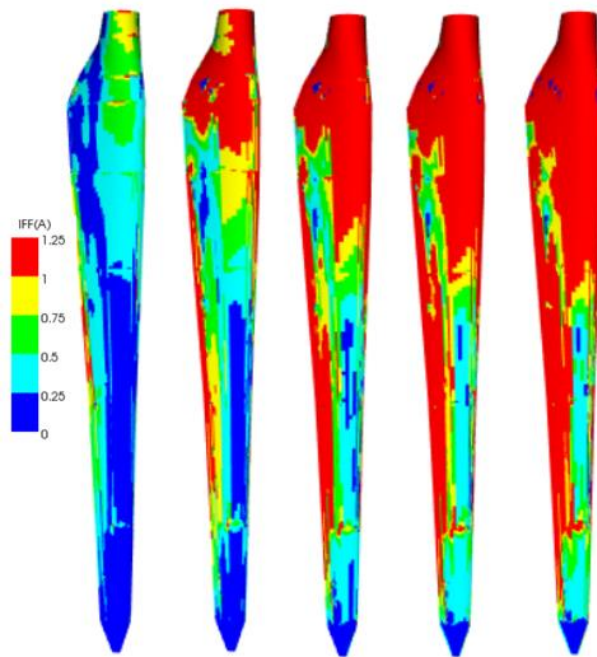


Figure 5.21. Contour plots of IFF (A) mode for the suction side of the blade under flapwise loads from 20% to 100% of the extreme flapwise and edgewise loading.

Figure 5.22 shows contour plots of failure inverse reserve factors of IFF(B) mode in the suction side of the blade is presented for loads from 10% to 100% of the extreme flapwise loading with increments of 10%. In the suction side of the blade, failure exposures of IFF(B) mode is as similar as failure exposures of IFF(A). The only difference is that failure exposures of IFF(B) mode initiate in the root and trailing edges of the blade at 40% of loading.

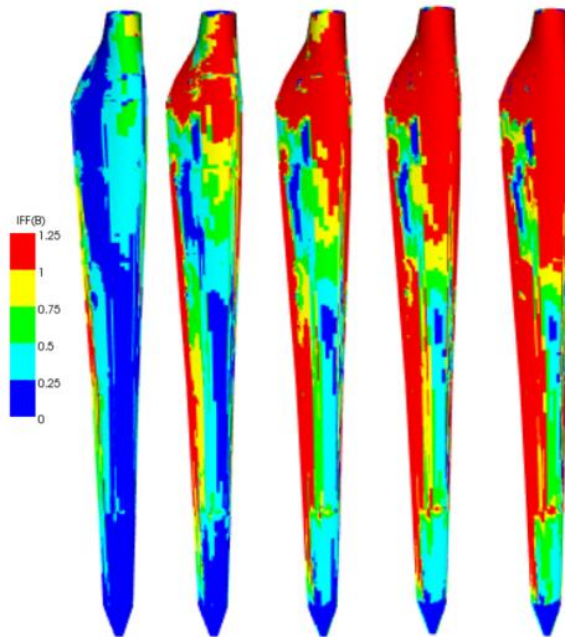


Figure 5.22. Contour plots of IFF (B) mode for the suction side of the blade under flapwise loads from 10% to 100% of the extreme flapwise and edgewise loading.

When Puck failure criteria are considered, ultimate failure of the blade is considered to take place if fiber failure (FF) in any ply occurs or when inter fiber failure IFF (C) in more than three plies of a laminate is observed. FF reduces the structural strength of the composite part drastically due to high energy release. In addition, risk of delamination is high when IFF (C) is seen in all plies. Figure 5.23 and Figure 5.24 show contour plots of Puck failure exposures for IFF(C) and FF in suction side of the blade under static loading in flapwise direction, respectively. In the suction side of the blade, failure exposures of IFF(C) and FF modes initiate in the root and trailing edges of the blade at 50% of loading. As the loading is further increased to 40% and 50% at the root and trailing edge become larger. After 50% of extreme loading, the failure regions occur trailing edge at the suction side of the blade between 0.5-metre and 0.7-metre as seen in red areas.

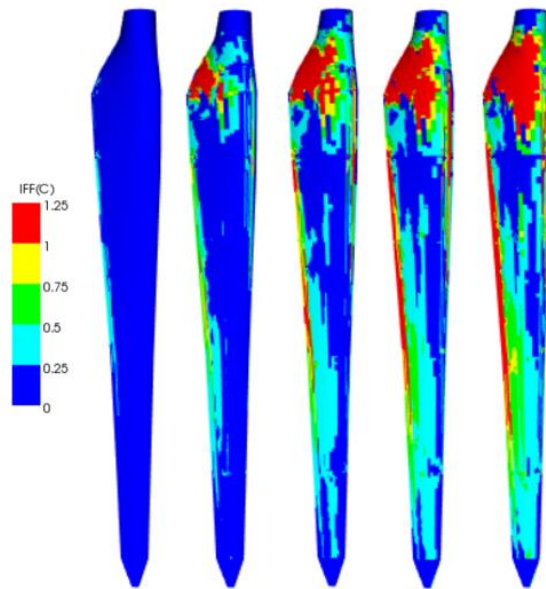


Figure 5.23. Contour plots of IFF (C) mode for the suction side of the blade under flapwise loads from 20% to 100% of the extreme flapwise and edgewise loading.

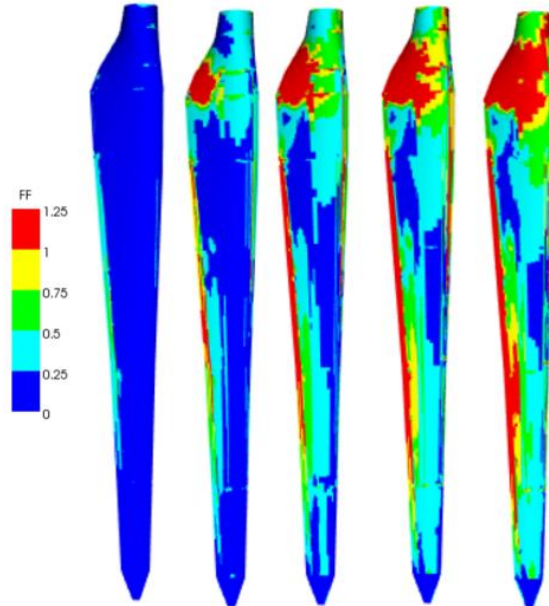


Figure 5.24. Contour plots of FF mode for the suction side of the blade under flapwise loads from 10% to 100% of the extreme flapwise and edgewise loading.

In pressure side of the blade, contour plots of Puck failure exposures for IFF(A), IFF(B), IFF(C) and FF under 100% static loading in flapwise direction are given in Figure 5.25, respectively. Failure modes IFF(A) is dominant skin, trailing edge and leading edge of the blade. The critical modes such as IFF(C) and FF are dominant in the root and leading edge of the blade.

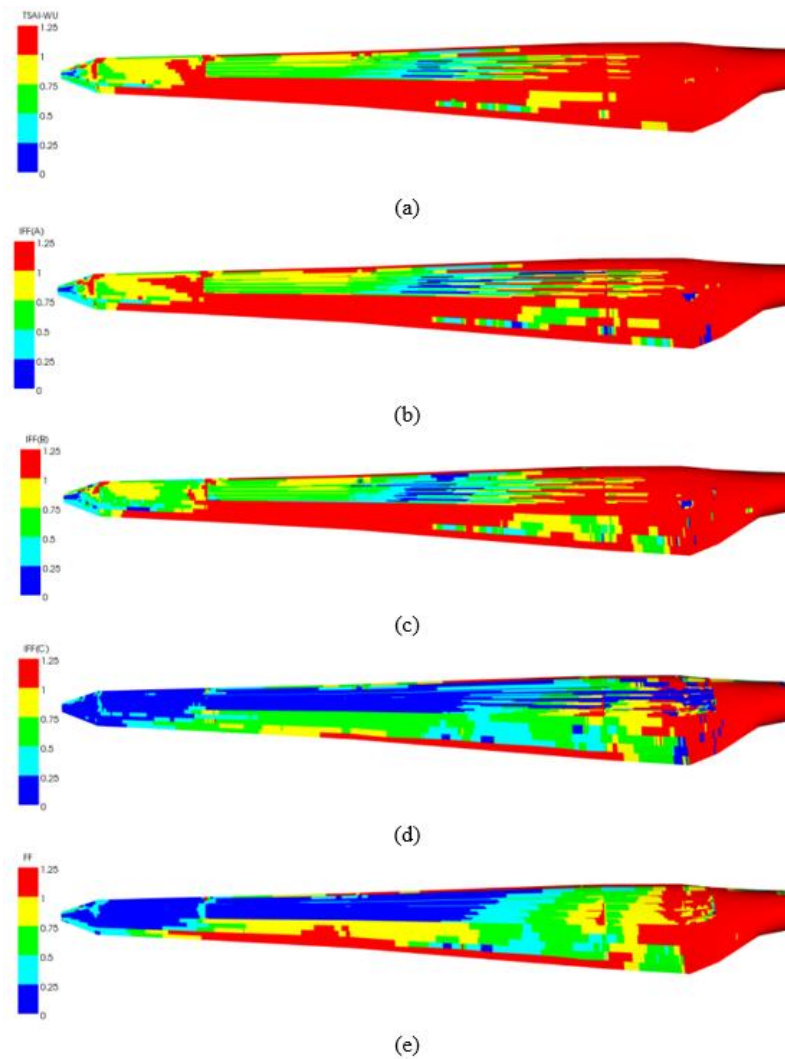


Figure 5.25. Contour plots of failure exposures of (a) Tsai-Wu (b) IFF(A) (c) IFF(B) (d) IFF(C) (e) FF for the pressure side of the unbonded blade under flapwise and edgewise loads.

Figure 5.26 shows contour plots of Puck failure exposures for IFF(A), IFF(B), IFF(C) and FF in chassis of the blade under static loading in flapwise direction, respectively. Failure modes IFF(A) is occurred the largest region of chassis. However, the critical modes such as IFF(C) and FF are dominant in spar cap region.

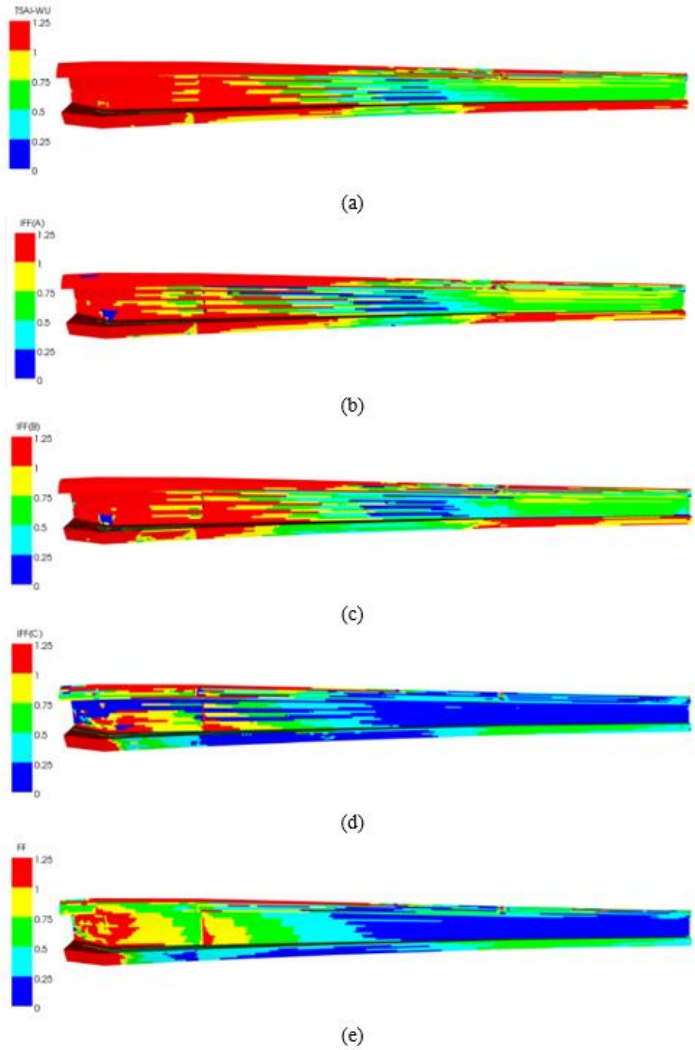


Figure 5.26. Contour plots of failure exposures of (a) Tsai-Wu (b) IFF(A) (c) IFF(B) (d) IFF(C) (e) FF for the chassis of the unbonded blade under flapwise and edgewise loads.

Figure 5.27 shows contour plots of Puck failure exposures for IFF(A), IFF(B), IFF(C) and FF in internal flange of the blade under static loading in flapwise and edgewise direction, respectively. For both Puck and Tsai-Wu failure criteria, Inverse reserve factor of all Puck failure exposures is above 1 in internal flange. Hence, ultimate failure is expected to occur in the internal flange under the extreme flapwise and edgewise loading case for both failure criteria.

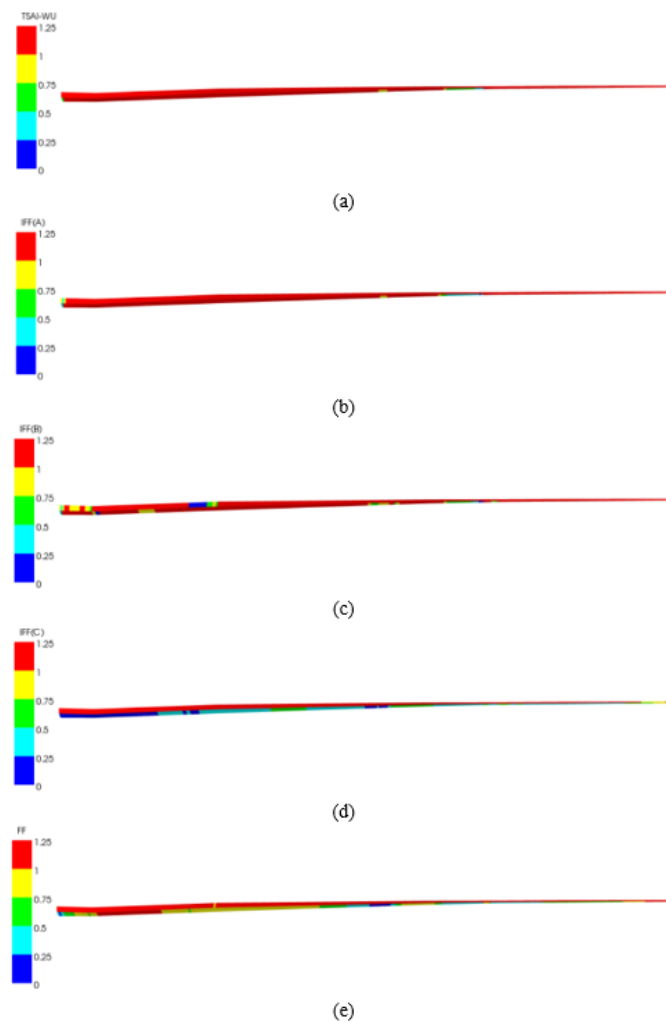


Figure 5.27. Contour plots of failure exposures of (a) Tsai-Wu (b) IFF(A) (c) IFF(B) (d) IFF(C) (e) FF for the internal flange of the unbonded blade under flapwise and edgewise loads.

CHAPTER 7

DISCUSSION

In this chapter, the results of the blade finite element analysis are compared. In the Section 6.1, results based on different loading conditions are compared. In the Section 6.2, Tsai-Wu and Puck failure criteria difference in the analysis is discussed. On the other hand, results of finite element analyze of the fully-bonded and unbonded blade are investigated subjected to natural frequencies, strength and failure mechanisms in Section 6.3.

6.1. Comparison of Stress Under Different Loading Conditions

To obtain stress differences along blade section between static loading under flapwise and edgewise directions, finite element analyzes of the blade under two different loading conditions is performed. First and foremost, the fully-bonded existing 5-meter composite wind turbine blade is analyzed under two different loading conditions: flapwise loading, flapwise and edgewise loading. The loads are given in Figure 3.16. In the first analysis, only loads in the flapwise direction are applied at the 21 stations on the blade. In the second analysis, loads in the both edgewise and flapwise directions are applied to the blade at the 21 stations. The stress differences along the section of each components of the blade are investigated in Figure 6.1, Figure 6.2 and Figure 6.3, respectively. The investigation focus on stresses in fiber direction, transverse fiber direction and shear stresses. These stresses are chosen because they are used in failure analyzes using Tsai-Wu and Puck criteria. Stresses in the fiber and transverse fiber directions are similar for both loading conditions. Shear stresses are varied slightly in spar and internal flange. It is observed that loads in the edgewise direction can be negligible.

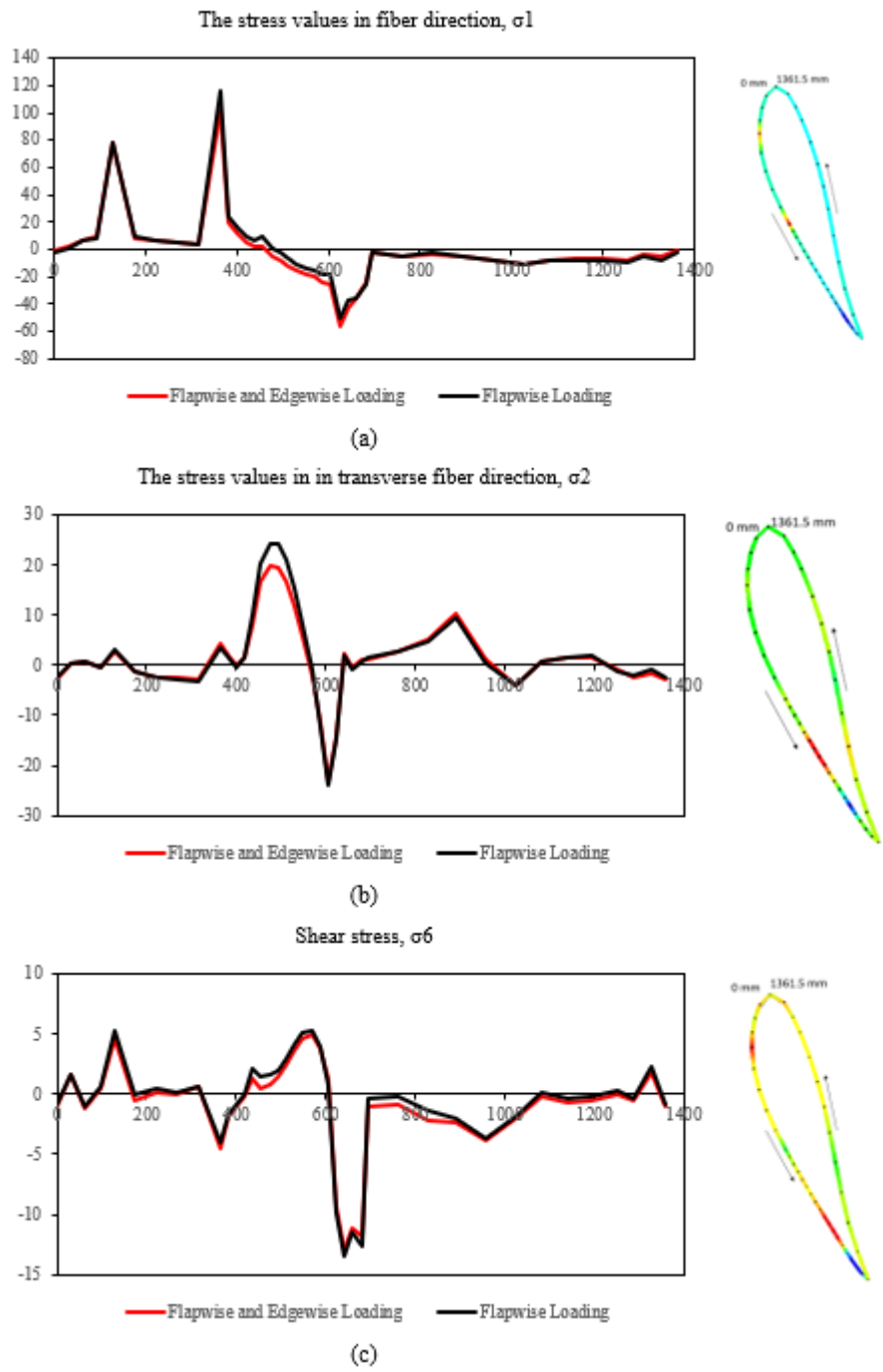


Figure 6.1. Stress distribution at the section of 0.7-metre from the root at the skin.

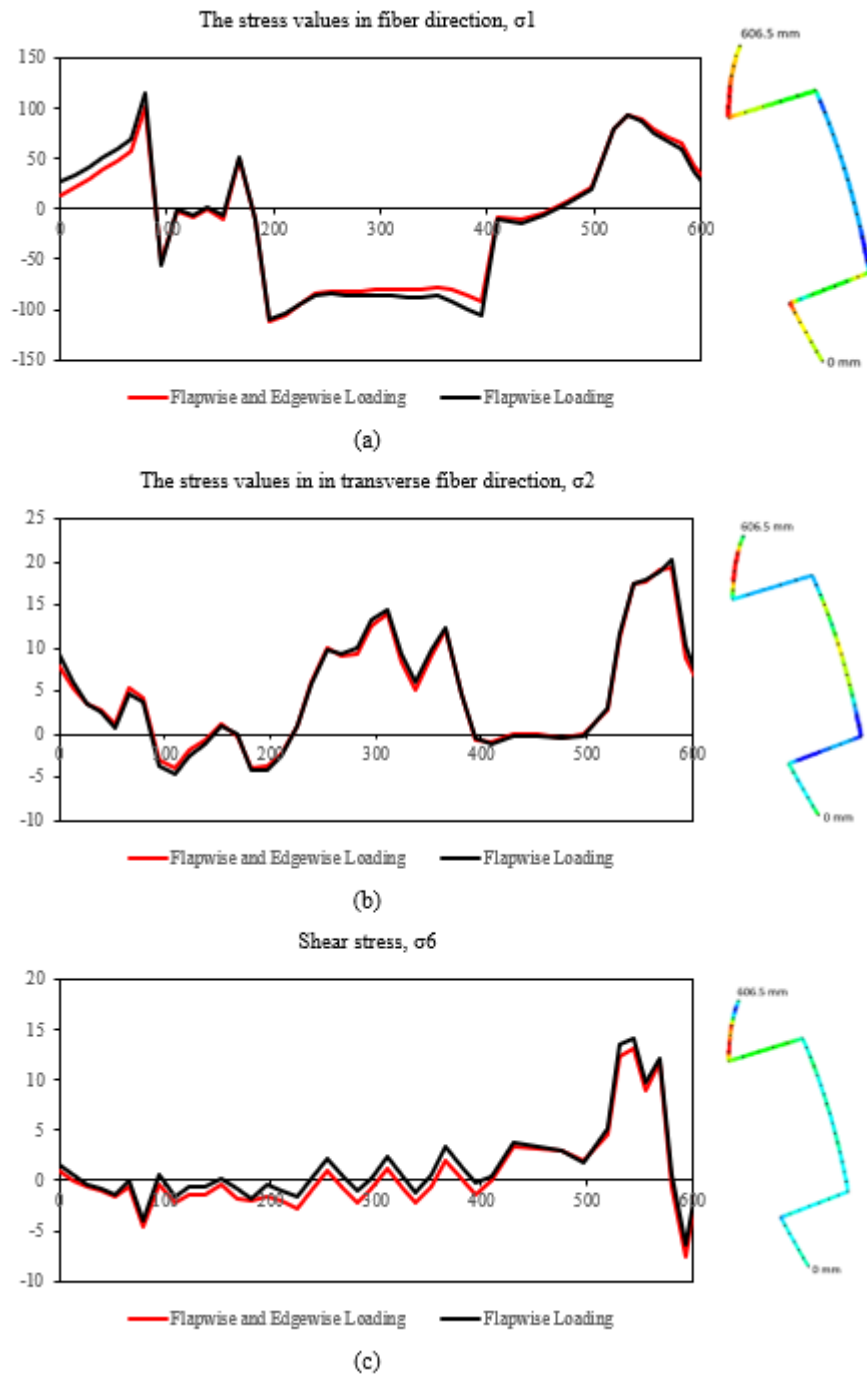


Figure 6.2. Stress distribution at the section of 0.7-metre from the root at the spar.

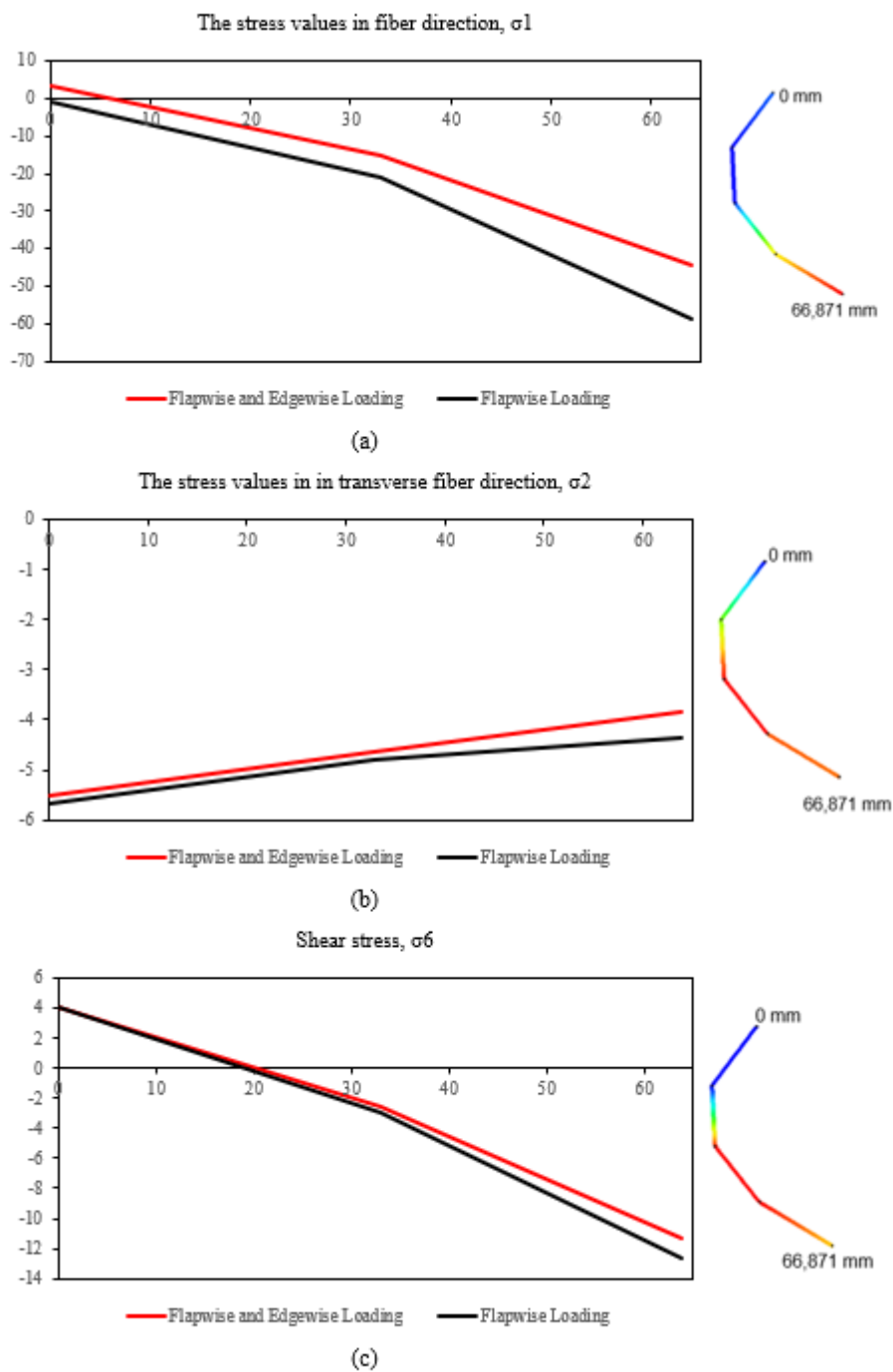


Figure 6.3. Stress distribution at the section of 0.7-metre from the root at the internal flange.

6.2. Comparison of Tsai-Wu and Puck Failure Criteria

Tsai-Wu failure criterion clarifies tensile and compressive stress through linear terms, so it is widely used theory for composite laminates. Tsai-Wu is a simple failure criterion which takes interaction of stresses in different directions into account by making use of strength tensors. On the other hand, Puck failure criteria explain the failure of the composite laminates within fiber and matrix failure due to transverse and shear loads separately. In the present study, linear failure analysis using Tsai-Wu criterion is compared with linear failure analysis using Puck criteria.

The failure analysis based on Puck and Tsai-Wu criteria performed both fully-bonded and unbonded blade model. The results of these analyzes are given in Chapter 4 and Chapter 5 in detail. In this section, to compare Tsai-Wu and Puck failure criteria, results of the fully-bonded blade finite element analysis of under flapwise and edgewise loading are discussed.

Figure 6.4 shows the contour plots of inverse reserve factors of the suction side of blade for IFF(A), IFF(B), IFF(C), FF and Tsai-Wu failure criteria. Failure occurs if inverse reserve factor is greater than 1 and these failure areas are indicated in red. It is observed that inverse reserve factors of Tsai-Wu criterion are identical with inverse reserve factors of IFF(A) mode of Puck criterion while it is different from IFF(B), IFF(C) and FF modes of Puck criterion. However, it is pointless to compare these failure criteria with the contour plots of inverse reserve factors inasmuch as IFF(A) and IFF(B) do not cause ultimate failure, these modes are not treated as critical as FF and IFF(C). Also, Tsai-Wu failure criterion cannot distinguish between different fracture modes like Puck.

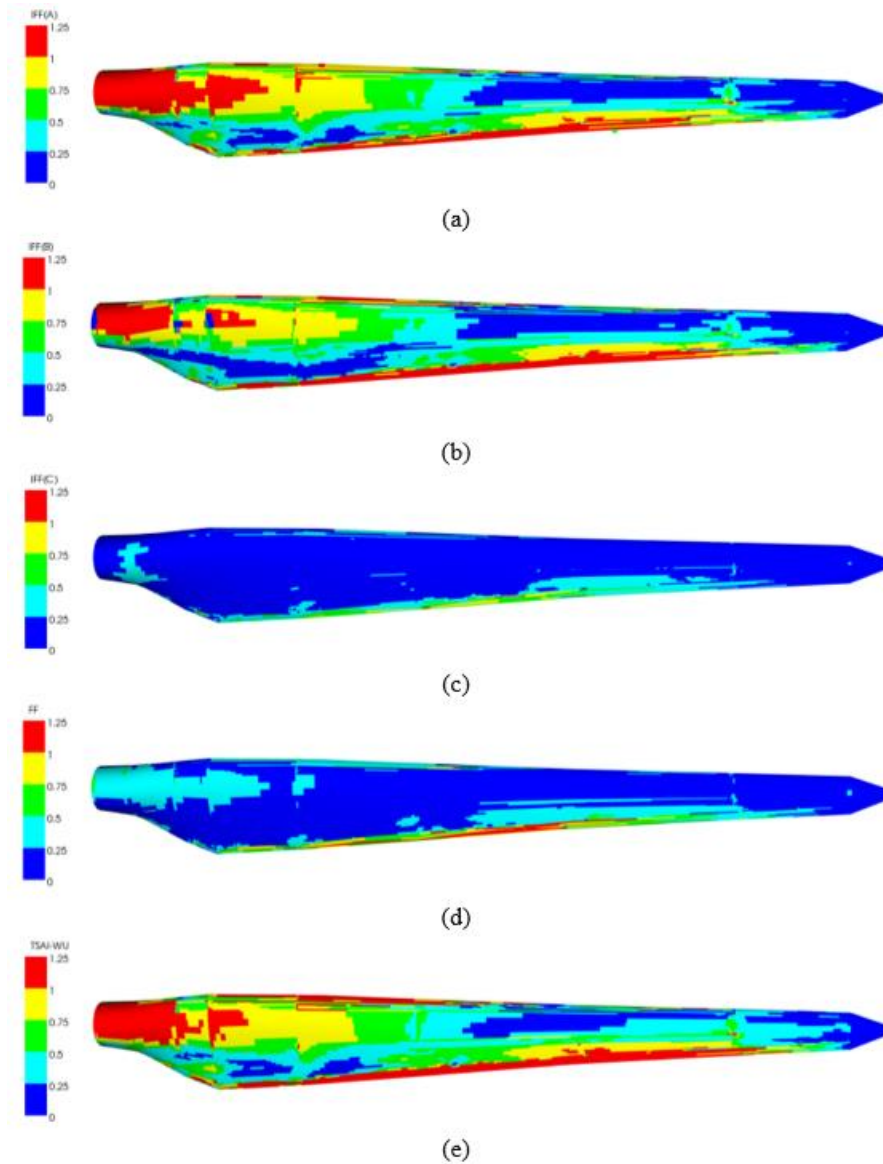


Figure 6.4. Contour plots of inverse reserve factors of (a) IFF(A) (b) IFF(B) (c) IFF(C) (d) FF (e) Tsai-Wu for the suction side of the fully-bonded blade under %40 of extreme flapwise and edgewise loading.

For more detailed investigation, an element is chosen at trailing edge of the suction side at 0.8-metre from root of the blade. Figure 6.5 shows the lay-ups, plies, stresses and inverse reserve factors of the element. The yellow areas show the lay-ups of the element through thickness. The sample element consists of three tri-axial architecture with fibers in the 0, +45° and -45° directions which are shown in red areas. The stresses in fiber direction, stresses in transverse fiber direction and shear stresses are plotted, also. It is observed that stresses change in ply-by-ply. Besides, inverse reserve factors of each failure criteria are plotted. To investigate failure modes based on inverse reserve factors in sample element, the graphs are plotted separately.

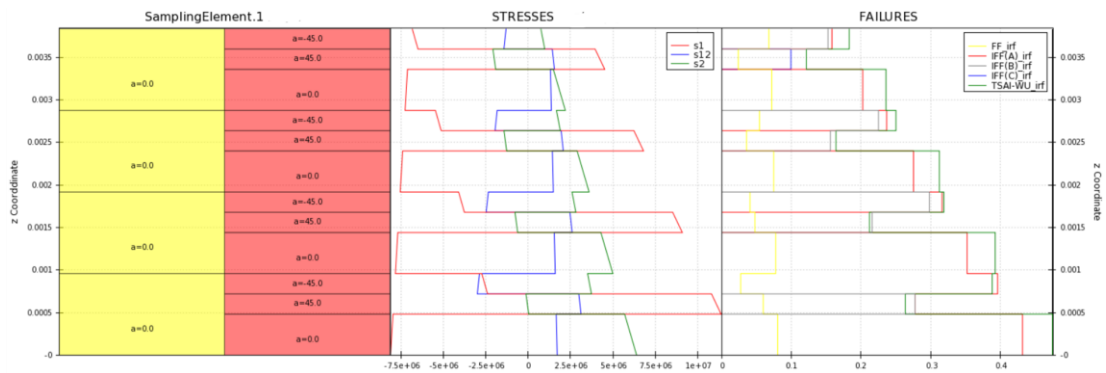


Figure 6.5. Comparison of Stress and Inverse Reserve Factor of Puck and Tsai-Wu Failure Criteria at the 0.8-metre of the fully-bonded blade under %40 of extreme flapwise and edgewise loading.

In Figure 6.6, inverse reserve factors of the suction side of blade for IFF(A), IFF(B), IFF(C) and Tsai-Wu failure criteria is plotted against thickness of the ply. As mentioned before, failure occurs if inverse reserve factor is greater than 1. Therefore, Tsai-Wu criteria do not show similarity with any Puck failure modes because Tsai-Wu criterion does not separate different fracture modes.

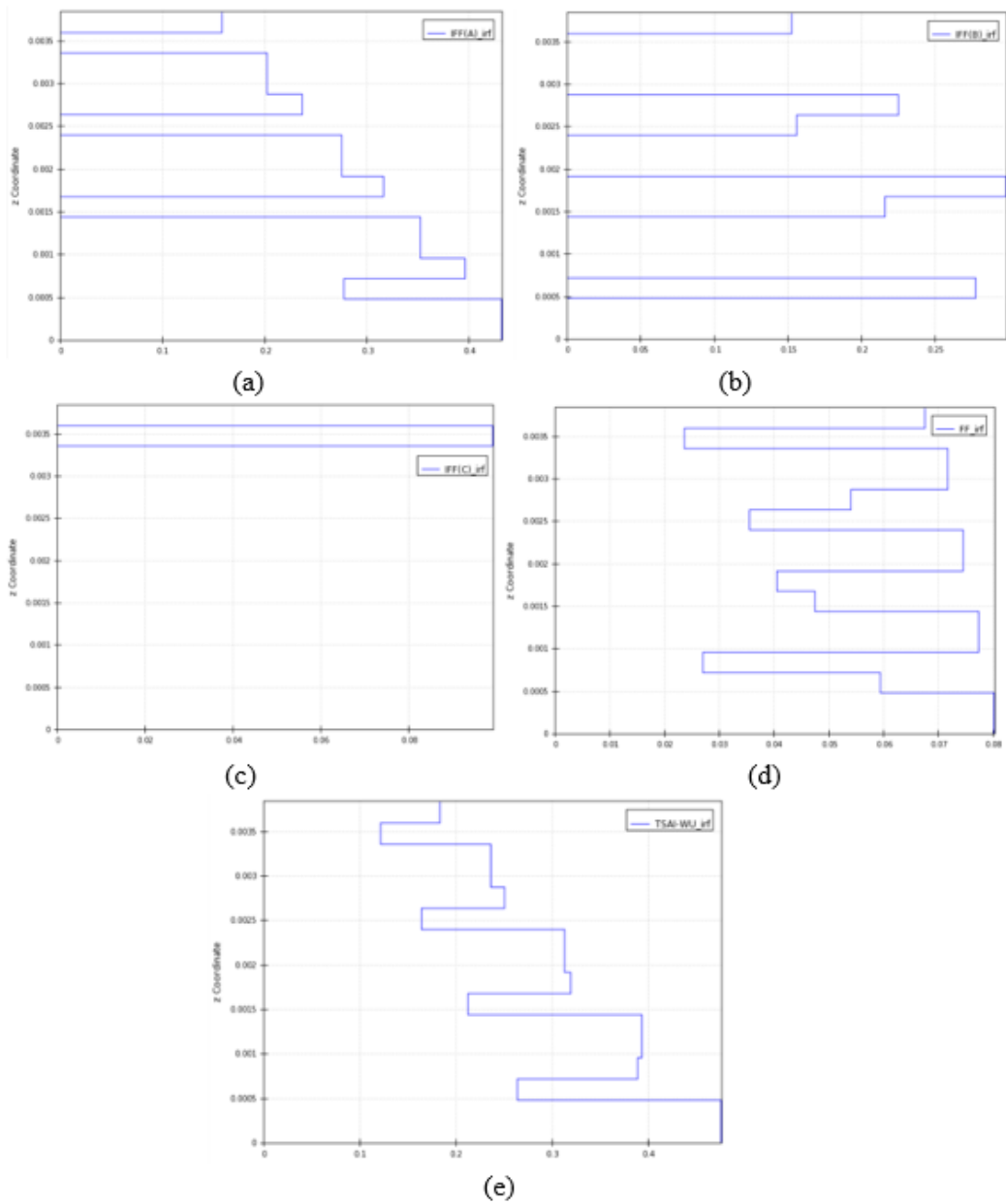


Figure 6.6. Inverse reserve factors of (a) IFF(A) (b) IFF(B) (c) IFF(C) (d) FF (e) Tsai-Wu at the 0.8-metre of the fully-bonded blade under %40 of extreme flapwise and edgewise loading.

To make more accurate comparison between Puck and Tsai-Wu failure criteria, the inverse reserve factor of Puck criterion is plotted by combining each failure modes with superposition management as given in Figure 6.7 (a). The plot of inverse reserve factor of Tsai-Wu criteria is given in Figure 6.7 (b). Note that if inverse reserve factor is greater than 1, failure occurs. It is observed that values of inverse reserve factors vary ply-by-ply although the plies which have inverse reserve factors above 1 are same for each failure criteria.

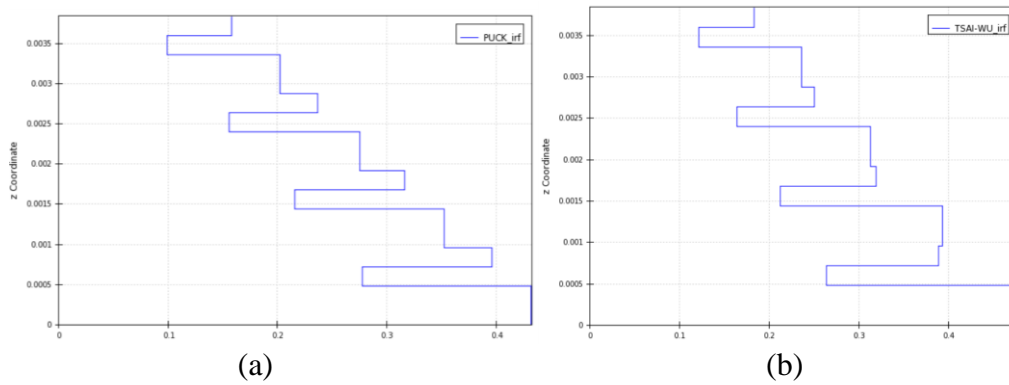


Figure 6.7. Inverse Reserve Factors of (a) Puck (b) Tsai-Wu at the 1-metre of the fully-bonded blade under %40 of extreme flapwise and edgewise loading.

In the same manner, an element is chosen at trailing edge of the suction side at 2.5-metre from root of the blade. The inverse reserve factors of Tsai-Wu and Puck criteria are given in Figure 6.8. There is no ply which have inverse reserve factor above 1, so there is no failure in the chosen element. Nevertheless, value of inverse reserve factors for Tsai-Wu and Puck failure criteria are different for ply-by-ply.

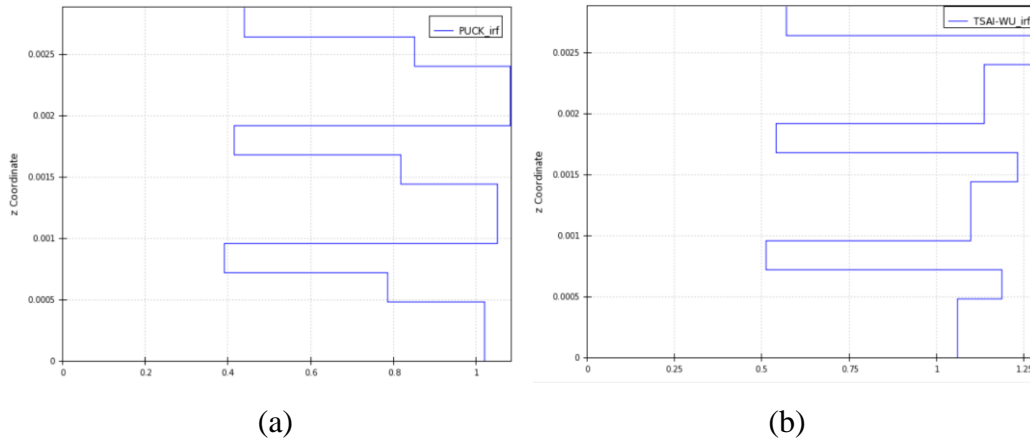


Figure 6.8. Inverse Reserve Factors of (a) Puck (b) Tsai-Wu at the 2.5-metre of the fully-bonded blade under %40 of extreme flapwise and edgewise loading.

6.3. Comparison of Fully-bonded and Unbonded Blade Model

In wind turbine blades, natural frequency is important to predict initial damage, so aeroelastic analysis must be done. In this study, the fully-bonded existing blade's natural frequencies are compared with natural frequencies of the unbonded blade. Figure 6.9 shows the natural frequencies vs mode shapes of the fully-bonded and unbonded blade models. First three modes shapes are defined as flapwise bending motion of the blade and the natural frequencies of the blade in these two modes are identical. Also, on 4th mode shape the natural frequencies are the same. The 5th modes shape is flapwise bending and edgewise bending coupling. In 5th mode shape, the natural frequency of the unbonded blade is started to decrease. The 6th modes shape is flapwise bending and torsion coupling. In 6th mode shape, the natural frequency of the unbonded blade is lower than fully-bonded blade's one. It is concluded that the lack of adhesive at the training edge is caused to decrease the natural frequency. In terms of instability of the blade, the natural frequency should be high enough to not cause flutter of the blade.

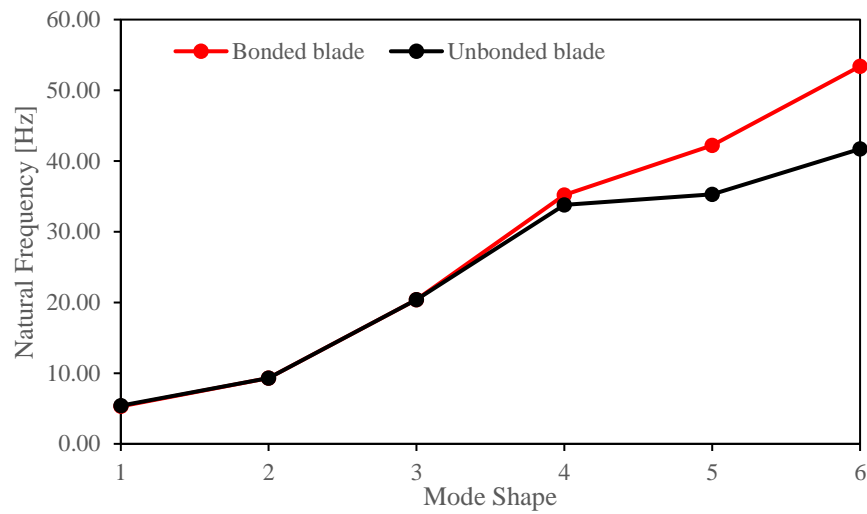


Figure 6.9. Mode shapes of unbonded and fully bonded blade models.

Total deformation under different loading cases in fully-bonded and unbonded blade model is investigated. In flapwise analysis, the deformation of the tip of the blade is approximately 1.5-meter for fully-bonded and unbonded blade model. In flapwise and edgewise analysis, the deformation of the tip of the blade is 1.4-meter for fully-bonded blade although it is the 1.5-meter in the unbonded blade model. The tip deformation of the blade stays the same even if the loading condition is changed. Thus, the stiffness for both cases is investigated.

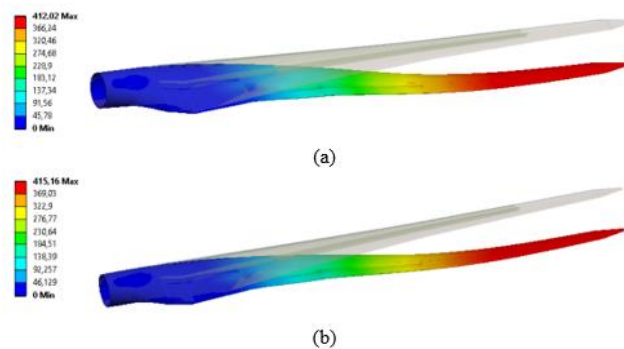


Figure 6.10. Total deformation of (a) fully-bonded (b) unbonded blade model under flapwise and edgewise loadings.

In Figure 6.11, the stiffness for each analyzes are given. Difference in stiffness of fully-bonded and unbonded blade can be negligible.

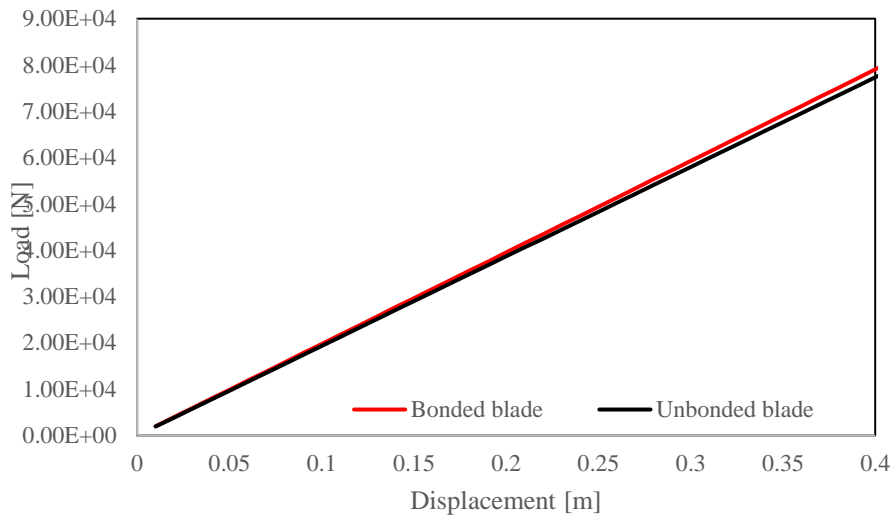


Figure 6.11. Load displacement curve of the blade corresponding to the fully-bonded and unbonded blade analysis.

Evaluation and visualization of Tsai-Wu inverse reserve factors and Puck failure exposures in the blade are viewed in Chapter 4 and Chapter 5 in detail. In this section, failure behavior of blade is investigated ply-by-ply. As can be seen from previous chapters, contours of the failure distribution in the blade are high at the unbonded region. Therefore, the contour plot of inverse reserve factors between 0.7 and 1.25 meters at the suction side of the fully-bonded blade is given in Figure 6.12. The red areas show the failed elements. The failures that occurred in that regions are as follows:

- The failure exposures are dominant in 1st and 8th plies for IFF(A).
- The failure exposures are dominant in 2nd and 4th plies for IFF(B).
- The failure exposures are dominant in 1st and 9th plies for IFF(C).
- The failure exposures are dominant in 2nd and 9th plies for FF.

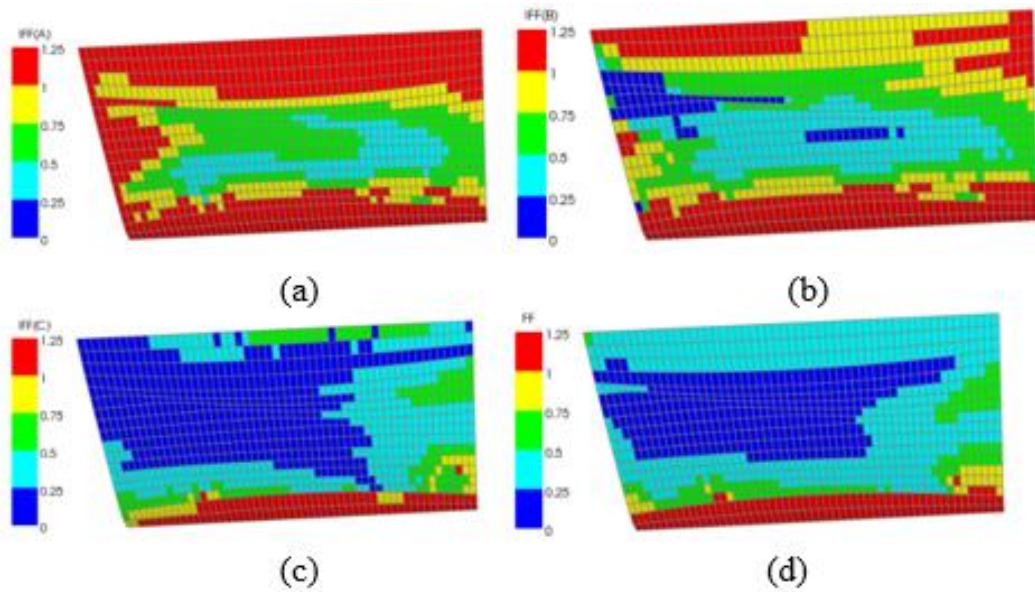


Figure 6.12. Contour plots of inverse reserve factors between 0.7-1.25 meters at the suction side of the fully-bonded blade for (a) IFF(A) (b) IFF(B) (c) IFF(C) (d)FF

In the same manner, the contour plot of inverse reserve factors between 0.7 and 1.25 meters at the suction side of the unbonded blade is given in Figure 6.12. Note that the red areas show the failed elements. It is observed that failure pattern at the unbonded blade changes as compared with failure pattern at the fully-bonded blade. On the other hand, failure exposures occur at the same ply as failure exposures at the fully-bonded blade.

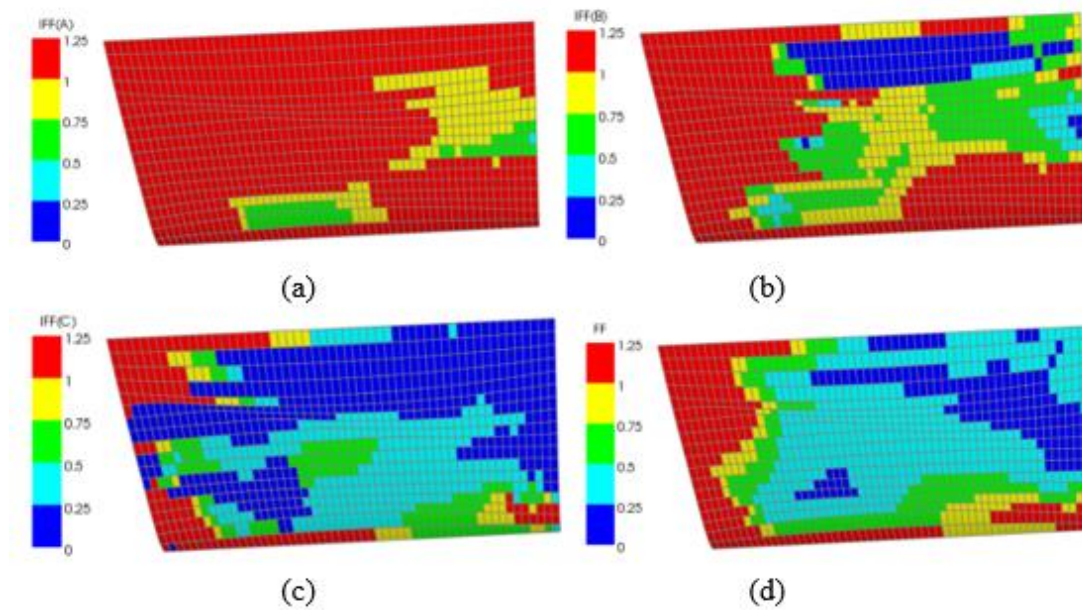


Figure 6.13. Contour plots of inverse reserve factors between 0.7-1.25 meters at the suction side of the unbonded blade for (a) IFF(A) (b) IFF(B) (c) IFF(C) (d)FF

A sample element is selected for more detailed information about failure exposures at the plies. The sample element is selected at the 0.8-meter from the root at the trailing edge of the suction side of the blade. The failure exposures are given in Figure 6.14 for fully-bonded blade and in Figure 6.15 for unbonded blade model. It is observed that the maximum inverse reserve factor at the unbonded blade occurs at the different ply from the fully-bonded blade model. For instance, at the 1st ply (0 degree), in the analysis of fully-bonded blade, there is no failure while analysis of unbonded blade shows that failure exposures occur for IFF(A) and IFF(B).

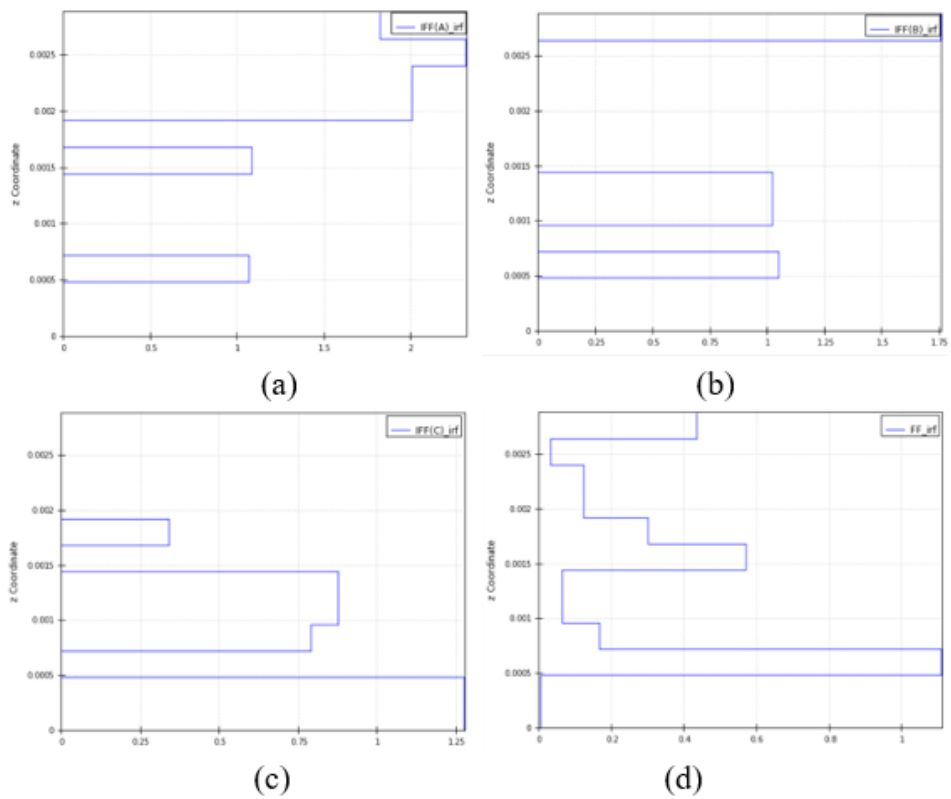


Figure 6.14. Inverse reserve factors ply-by-ply at the sample element of the fully-bonded blade for (a) IFF(A) (b) IFF(B) (c) IFF(C) (d)FF

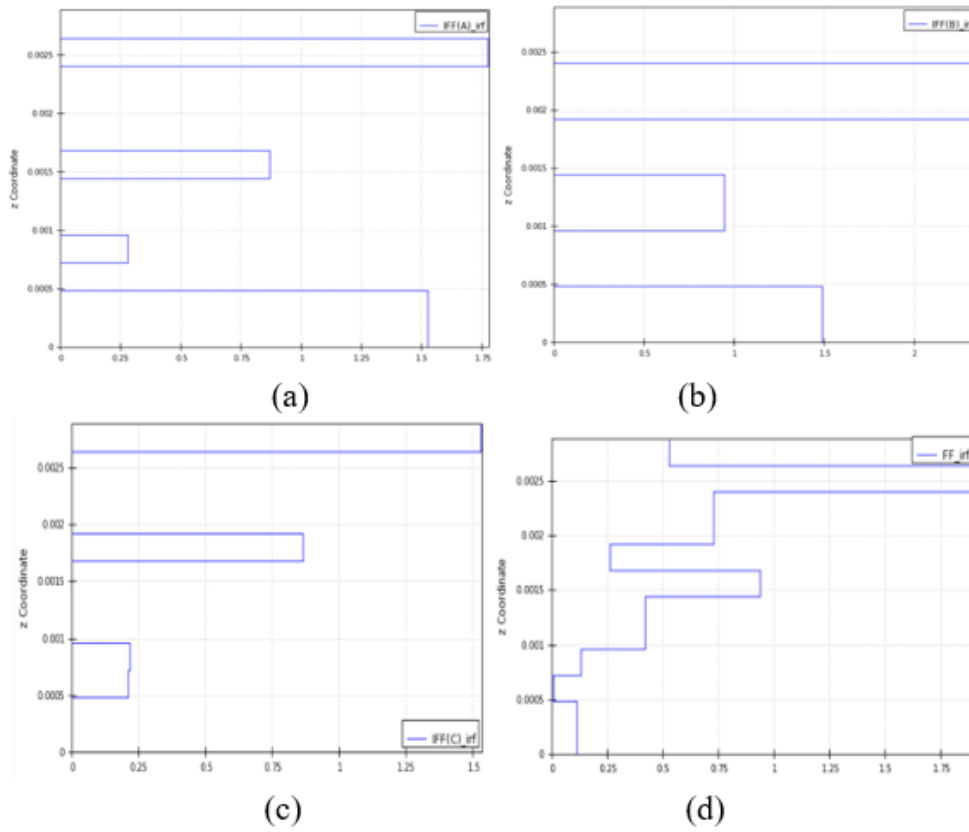


Figure 6.15. Inverse reserve factors ply-by-ply at the sample element of the unbonded blade for (a) IFF(A) (b) IFF(B) (c) IFF(C) (d)FF

The stress in the fiber and transverse fiber direction, shear stress distribution at the unbonded trailing edge region of the fully-bonded and unbonded blade are given in Figure 6.16 and Figure 6.17, respectively. As can be clearly seen figures, the maximum stress for all stresses occurs at the different location at the unbonded blade.

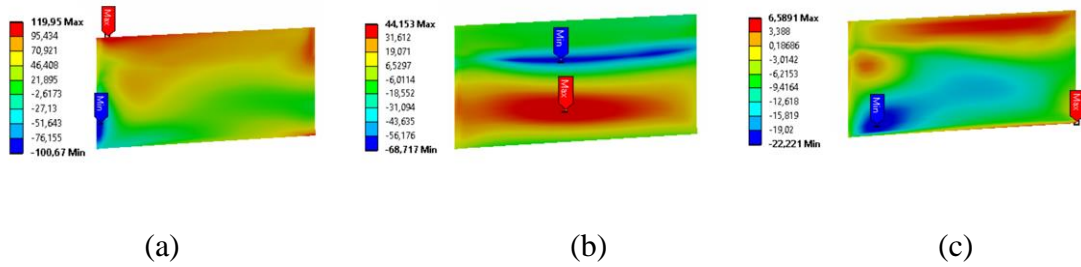


Figure 6.16. Stress distributions along suction side of the fully-bonded blade model between 0.7 and 1.25-metre (a) in fiber direction (b) in the transverse fiber direction (c) shear stress.

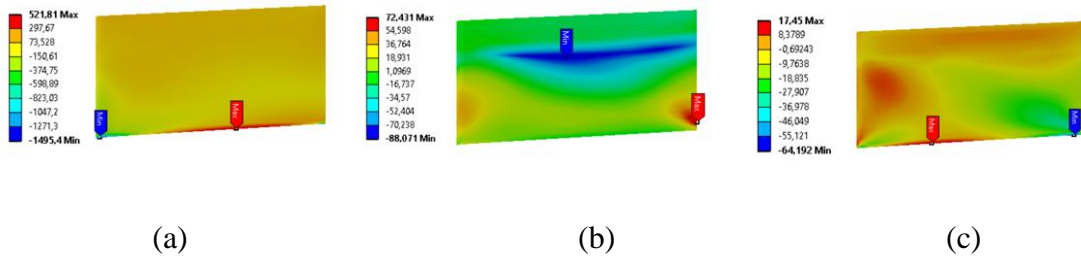


Figure 6.17. Stress distributions along suction side of the unbonded blade model between 0.7 and 1.25-metre (a) in fiber direction (b) transverse fiber direction (c) shear stress.

The stresses in the fiber direction and transverse fiber direction, shear stress in trailing edge between 0.7 and 1.25 meters of the fully-bonded and unbonded blade is given in Figure 6.19. It is observed that the maximum stresses occur at adhesive starting and ending points.

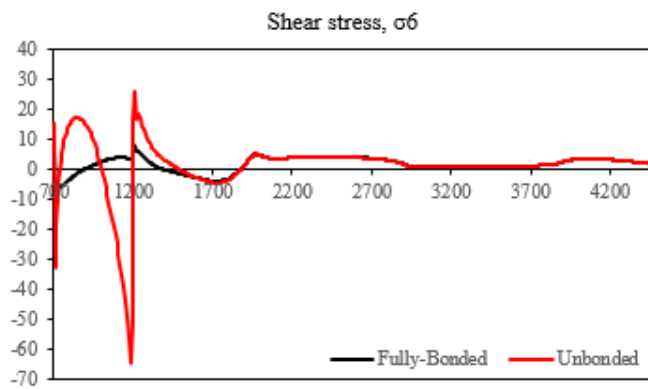
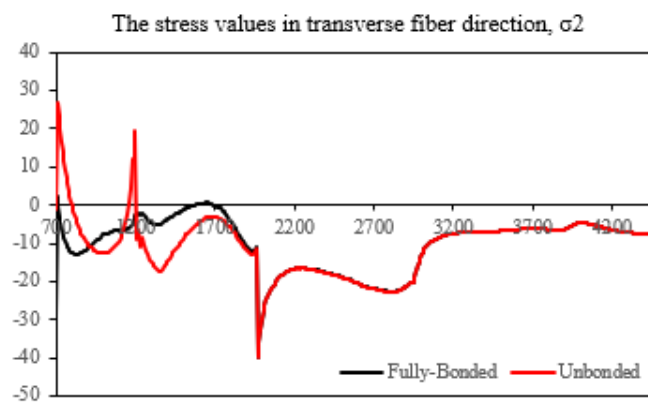
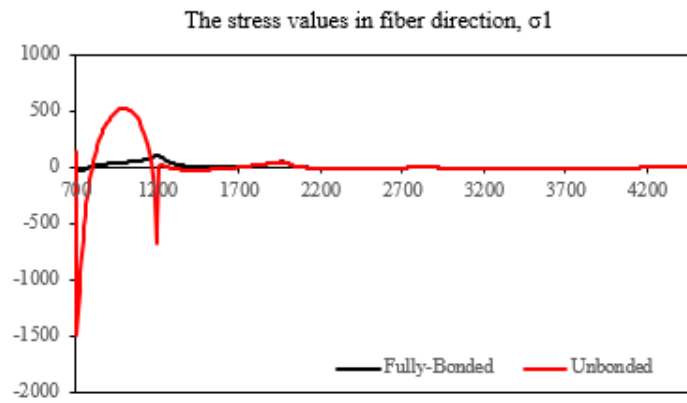
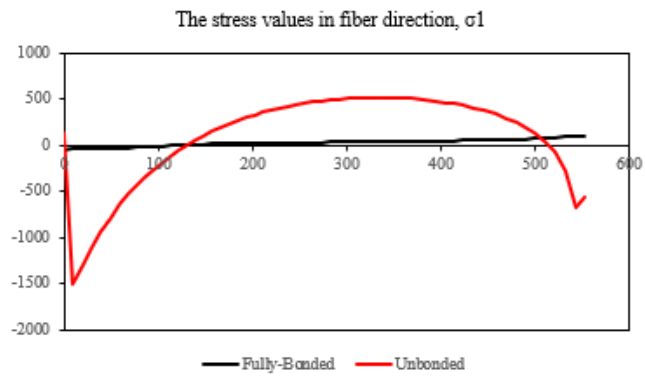
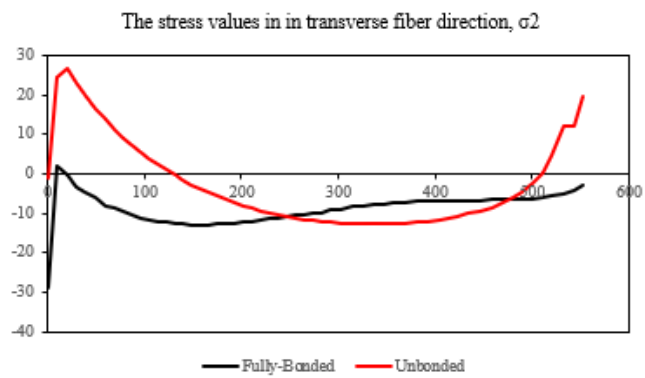


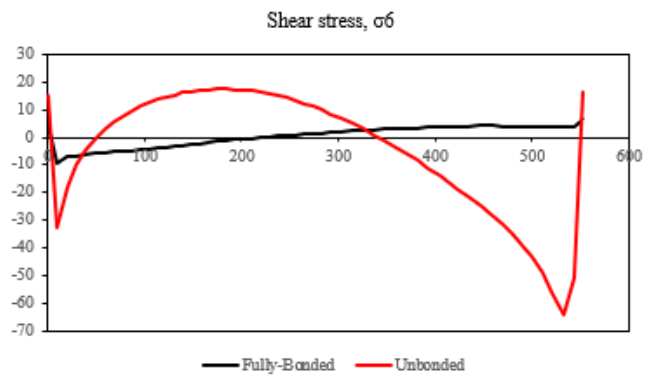
Figure 6.18. Stress distributions along trailing edge (a) in fiber direction (b) transverse fiber direction (c) shear stress.



(a)



(b)



(c)

Figure 6.19. Stress distributions along trailing edge between 0.7 and 1.25-metre (a) in fiber direction (b) transverse fiber direction (c) shear stress.

CHAPTER 8

SUMMARY AND CONCLUSIONS

7.1. Summary

In this thesis, strength analysis of an existing 5-meter glass-fiber epoxy composite wind turbine blade subjected to static loading condition is presented. Finite element analysis is performed to simulate the virtual testing of the blade and understand the failure modes/mechanisms which may lead to the ultimate failure of the blade. CAD model of the blade is prepared using NX 10.0 and ANSYS ACP/Pre module is utilized for building the material model of the blade. First and foremost, the finite element analyzes are performed under different static loading conditions. Total deformation and stress distribution along blade is investigated. Next, the evaluation of the failure along blade is done with two different approaches: linear elastic analysis using Tsai-Wu criteria and linear elastic analysis using Puck criteria. Linear analysis is carried out with ANSYS ACP/Post module. In literature, the most critical damage occurs as debonding between suction and pressure sides of the blade. Thus, analyzes of the blade are repeated with the blade that has debonding between suction and pressure sides. After the analysis of the blade, ANSYS ACP/Post module is used for the visualization of the results. From the interpretation of the results, critical components and regions with the highest risk of failure are identified. Additionally, the fully-bonded and unbonded blades are compared according to results of finite element analysis.

7.2. Conclusions

This thesis presents two objectives to obtain strength behavior of an existing 5-metre composite wind turbine blade. Finite element modelling of existing blade is performed to investigate blade behavior e.g. analysis of blade deflection under flapwise and edgewise loading, analysis of natural frequencies, analysis of strength of structural parts. In order to predict failure modes, a finite element simulation is performed using two different composite failure models: linear elastic analysis using Tsai-Wu criteria and linear elastic analysis using Puck criteria to check the strength of the blade subjected to static loading. Additionally, a fully-bonded composite wind turbine blade compares with a blade which has unbonded trailing edge. The conclusions are as follows:

- The stress difference along blade section between static loading under flapwise and edgewise directions is found to be negligible.
- In investigation of the failure modes the Puck criterion should be preferred over Tsai-Wu criteria since by using Puck criterion, more detailed information about the failure mechanism of the blade can be obtained.
- For Puck failure criterion, the failure at the blade occurs in the same ply in both the fully-bonded and unbonded trailing edge models. However, the number of the failed elements and the pattern of the failure are different for these two cases due to the stress differences in the unbonded trailing edge.
- Debonding on the trailing edge does not cause a significant change of failure pattern in spar and internal flange. Thus, debonding by itself is not sufficient to cause an ultimate failure of the blade.
- Root and trailing edge of the blade are the regions with the highest risk of failure initiation. In spar Puck reserve factors are significantly high at the adhesive joint of the spar to skin near the blade root. These locations are typical locations, where failure initiation is expected.

Novelties of present study are;

- Tsai-Wu and Puck failure criteria are compared ply-by-ply using linear elastic finite element analysis.
- Adhesive joint failure in a small wind turbine blade is investigated in detail.

7.3. Future Works

In the future, results of the analysis will be used to calibrate structural test set-up of the blade. Failure areas of the blade will be investigated after testing under static loading. Strength analysis of the blade using Puck failure criteria is useful for predicting failure initiation load, failure mode and failure location before testing of the blade. The finite element results show that since dangerous failure modes FF and IFF(C) are observed in the root and trailing edge of the blade, ultimate failure is expected to occur under extreme loading.

In this study, linear material model using Tsai-Wu and Puck criteria are used in the finite element analyzes. Hence, progressive failure analysis is necessary in order to capture more realistic simulation of the failure mechanisms prior to testing. The load paths and failure pattern of the blade will change as the elements fail when progressive Puck criteria are used.

REFERENCES

- [1] GmbH and G. L. Wind Energie, *Guideline for the Certification of Offshore Wind Turbines*, 2005.
- [2] D. White, "New Method for Dual-Axis Fatigue Testing of Large Wind Turbine Blades Using Resonance Excitation and Spectral Loading," National Renewable Energy Laboratory, 2004.
- [3] J. Manwell, *Wind Energy Explained, Theory Design and Application*, John Wiley & Son, 2010.
- [4] C. A. O. Algarin, *Root Blade Load Estimation by Measurement Database for the Implementation in a SCADA System*, Master Thesis.
- [5] J. Leon Mishnaevsky, K. Branner, H. N. Petersen, J. Beauson, M. McGugan and B. F. Sørensen, "Materials for Wind Turbine Blades: An Overview," *Materials — Open Access Journal of Materials Science*, vol. 10, 2017.
- [6] *IEC 61400-2: Wind turbines - Part 2: Small wind turbines*, 2013.
- [7] J. Holmes, B. Sørensen and P. Brøndsted, "Reliability of Wind Turbine Blades: An Overview of Materials Testing," in *Shanghai : Chinese Renewable Energy Industry Association*, 2007.

- [8] H. v. Leeuwen, D. v. Delft, J. Heijdra, H. Braam, E. R. Jørgensen, D. Lekou and P. Vionis, "Comparing Fatigue Strength From Full Scale Blade Tests With Coupon-Based Predictions," *J. Sol. Energy Eng*, vol. 124, pp. 404-411, 2002.
- [9] F. Jensen, B. Falzon, J. Ankersen and H. Stang, "Structural Testing and Numerical Simulation of a 34 m Composite Wind Turbine Blade.," *Composite Structures*, vol. 76, pp. 52-61, 2006,.
- [10] L. M. Jr, R. N. P. Brøndsted, D. Lekou and T. Philippidis, "Materials of Large Wind Turbine Blades: Recent Results in Testing and Modeling," *Wind Energy*, vol. 15, pp. 83-97, 2012.
- [11] Z. Shi, J. Dong and W. Ma, "Stress Characteristics Analysis on a Composite Wind Turbine Blade," *Advanced Materials Research*, Vols. 602-604, pp. 111-114, 2012.
- [12] J. Chen, W. Z. Shen, Q. Wang, X. Pang, S. Li and X. Guo, "Structural Optimization Study of Composite Wind Turbine Blade," *Materials & Design*, vol. 46, pp. 247-255, 2013.
- [13] M. Guțu, "Analysis of a Composite Blade Design for 10 kW Wind Turbine Using a Finite Element Model," *Applied Mechanics and Materials*, vol. 657, pp. 589-593, 2014.

- [14] H. G. Lee and J. Park, "Static Test Until Structural Collapse After Fatigue Testing of a Full-scale Wind Turbine Blade," *Composite Structures*, vol. 136, pp. 251-257, 2016.
- [15] X. Chen, X. Zhao and J. Xu, "Revisiting The Structural Collapse of a 52.3 m Composite Wind Turbine Blade in a Full-scale Bending Test," *Wind Energy*, vol. 20, pp. 1111-1127, 2017.
- [16] T. P. Philippidis and G. A. Roukis, "Structure Design Report of METUWIND Small Rotor Blade," Confidential Interim Report, unpublished, 2013.
- [17] Ansys Workbench, <http://www.ansys.com/products/platform/>.
- [18] Ansys ACP, <http://www.ansys.com/products/structures/ansys-composite-reppost>.
- [19] S. Tsai and M. Wu, "A General Theory of Strength for Anisotropic Materials," *J. Composite Materials*, vol. 5, pp. 58-80, 1971.
- [20] M. Knops, *Analysis of Failure in Fiber Polymer Laminates : The Theory of Alfred Puck*, ISBN 978-3-540-75765-8, 2008, p. 205.
- [21] V. Passipoularidisa, T. Philippidis and P. Brondsted, "Fatigue life prediction in composites using progressive damage modeling under block and spectrum loading," *International Journal of Fatigue*, vol. 33, p. 132–144, 2011.

- [22] B. F. Sørensen, K. Branner, H. Stang, H. Jensen, E. Lund, T. Jacobsen and K. Halling, "Improved Design of Large Wind Turbine Blades of Fibre Composites (Phase 2)," Risø National Laboratory, Denmark, 2005.
- [23] C. B. M. Knops, "Gradual Failure Process in Fiber/polymer Laminates," *Composites Science and Technology*, vol. 66, pp. 616-625, 2016.
- [24] J. A. P. Mark A. Rumsey, "Structural Health Monitoring of Wind Turbine Blades," in *SPIE*, 2008.
- [25] R. Ata, "The Current Situation of Wind Energy in Turkey," in *Hindawi Publishing Corporation*, 2013.
- [26] C. Amer and M. Sahin, "Structural Analysis of a Composite Wind Turbine Blade," in *World Academy of Science, Engineering and Technology International Journal of Aerospace and Mechanical Engineering*, 2014.
- [27] Council, "Global Wind Report," Global Wind Energy, 2014.
- [28] G. Bir and P. Migliore, "Preliminary Structural Design of Composite Blades for Two- and Three-Blade Rotors," National Renewable Energy Laboratory, 2004.
- [29] N. B. Chaudhari, "Dynamic Characteristics of Wind Turbine Blade," *International Journal of Engineering Research and Technology*, vol. 3, no. 8, pp. 168-173, 2014.

- [30] E. M. Fagan, S. B. Leen, C. R. Kennedy and J. Goggin, "Finite Element-Based Damage Assessment of Composite Tidal Turbine Blades," in *Journal of Physics: Conference Series*, 2015.
- [31] B. Standard, *Wind Turbines, Part 2: Design requirements for small wind turbine*, BS EN 61400-2:2006 , 2006.
- [32] P. Soden, A. Kaddour and M. Hinton, "Recommendations for designers and researchers resulting from the world-wide failure exercise," *Composites Science and Technology* , vol. 64, p. 589–604, 2003.
- [33] NX 10.0, <http://www.plm.automation.siemens.com/en/products/nx/>.